université de BORDEAUX

THÈSE PRÉSENTÉE
POUR OBTENIR LE GRADE DE

DOCTEUR DE

L'UNIVERSITÉ DE BORDEAUX

ÉCOLE DOCTORALE DES SCIENCES CHIMIQUES

SPÉCIALITÉ : Chimie Physique

Par Hsiang-Hsin Chen

TITRE

Imagerie IRTF tridimensionnelle pour l'étude de l'insuffisance rénale chronique

Sous la direction de : Cyril Petibois

Soutenue le 16/12/2015

Membres du jury :

M. Laroche, Gaétan	Professeur,	Université Laval, Quebec, Canada	Rapporteur
Mme Javerzat, Sophie	Professeur,	Université de Bordeaux	Examinateur, présidente
M. Moenner, Michel	Professeur,	Université de Bordeaux	Examinateur
M. Hwu, YeuKuang	Professeur,	Institute of Physics, Taipei, Taiwan	Invité

Titre : Imagerie IRTF tridimensionnelle pour l'étude de l'insuffisance rénale chronique

Résumé :

L'insuffisance rénale chronique (IRC) et l'une des pires maladies chroniques dans les pays développés. Les grades de l'IRC sont principalement basés sur la mesure ou l'estimation du taux de filtration rénale (GFR). Cependant, cette méthode est peu sensible sur les premiers stades de la pathologie et n'apporte donc pas de valeur diagnostique. La détection de la pathologie à des stades précoces et son traitement peuvent éviter ou limiter les effets délétères de la chronicité. Cette thèse se penche sur le développement de la microscopie IRTF en tant qu'outil diagnostic pour l'identification par histopathologie à l'échelle du glomérule dans un modèle d'IRC. Nous avons développé la technique de reconstruction 3D pour l'imagerie IRTF des modifications biochimiques à l'échelle du glomérule pour déterminer des marqueurs de l'IRC. La déconvolution spectrale et le clustering sont appliqués après analyses IRTF pour distinguer les modèles sains et pathologiques. Ensuite, la microvasculature glomérulaire est révélée par agent de contraste pour en déterminer les anomalies morphologiques. Grâce aux résultats obtenus en 3D et l'utilisation de méthodes statistiques avancées, la microscopie IRTF est utilisée comme une technique fonctionnelle pour déterminer les modifications morphologiques et moléculaires apparaissant au cours du développement de l'IRC.

Mots clés : IRFT, insuffisance rénale chronique, microscopie, histopathologie

Title : THREE-DIMENTIONSAL INFRARED IMAGING FOR CHRONIC KIDNEY DISEASE INVESTIGATION

Abstract :

CKD (Chronic Kidney Disease) is one of the worst public diseases in developing countries. The stages of CKD are mainly based on measured or estimated GFR (Glomerular Filtration Rate). However, this method is not sensitive enough on early stages of the pathology and thus do not offer accurate diagnostic value. Early detection and treatment can often limit or avoid the chronicity effects of the disease. This thesis focuses on the development of FTIR microscopy as a diagnostic tool for the identification by histopathology at glomerulus level of the kidney in CKD model. We developed a technique of 3D reconstruction for the FTIR imaging of biochemical components changes in glomeruli for identifying the pathological marker of CKD. The curve-fitting and spectral clustering are applied on the FTIR microscopy analysis to distinguish between healthy and pathological glomeruli of a kidney. Then, the glomerular microvasculature is highlighted to reveal the morphological abnormalities by perfusing contrast agents into blood vessels. With advanced 3D statistical methods and 3D image visualization by microscopy, FTIR spectro-imaging can be used as a functional technique to determine the morphological and molecular changes occurring along CKD development.

Keywords : FTIR, CKD, glomeruli, histopathology

Unité de recherche

LAMC , Inserm U1029, Allée Geoffroy Saint-Hillaire, 33600 Pessac

PhD Thesis

PRESENTED AT THE UNIVERSITY OF BORDEAUX

DEPARTMENT OF LIFE SCIENCE

THREE-DIMENTIONAL INFRARED IMAGING FOR CHRONIC KIDNEY DISEASE INVESTIGATION

by HSIANG-HSIN CHEN

To obtain the title of doctor

Acknowledgements

This work would not be possible without the support and encouragement of the professors and colleagues in Bordeaux and Taiwan, whose much inspiring presence has deeply enriched my years in the University of Bordeaux.

Firstly and foremost, I would like to thank my supervisor, Dr. Cyril Petibois, for his support, encouragement, and guidance during my study. His mastery of spectroscopic imaging and his strong enthusiasm for scientific enterprise have been inspirational role-model to me in the rest of my research path.

I would also like to thank Professor Sophie Lecomet and Andreas Bikfalvi for giving me the opportunity to study my PhD project in CBMN and U1029 research groups, respectively, throughout the period of this work. Their valuable support is the precious part of my PhD study to be deeply acknowledged.

In particular, I would like to thank Dr. Yeukuang Hwu, the senior researcher of Institute of Physics in Academia Sinica, Taiwan for his precious comments, support and helps during my PhD study. I would like to say special thanks to the colleagues of his group for their availability, encouragements and helps about my work. I also pay my deepest gratitude to Dr. Ann Chen, Doctor of Tr-iservice Hospital in Taiwan, and his group members for the collaboration of work and helps in our research by providing the tissue samples.

I would also like to say my deepest thanks to Prof. Gaétan Laroche, Universite Laval, Canada, and Prof. Michel Moenner, Universite de Bordeaux, for generously providing their time and valuable suggestions in evaluating my thesis as the jury of my thesis defense. I am very grateful to Prof. Sophie Javerzat, Universite de Bordeaux for accepting be the referee, detailed reading my thesis. I would like to say special thanks to Prof. Chia-liang Cheng for his time out of his busy schedule and suggestions about my thesis.

Sincere thanks to members of my research group for being my loved friends and trusted allies as well as providing their patience and efforts about the experiment preparation and statistical discussions of my data

analysis problems.

Special thanks to my friends in Bordeaux whom made my life at the University of Bordeaux richer and livelier.

Finally, I would like to express my sincerest thanks and gratitude to my family in Taiwan who have provided their deep love and encouragement throughout my PhD work. Despite being thousands of miles away, they have been an integral part of my life and I owe it all to them.

Three-dimensional Infrared Imaging for Chronic Kidney Disease Investigation

Table of Contents

List of Figures

List of Tables

List of Abbreviations

ADMD	Asymmetric dimethylarginine
FAC	Fatty acyl chain
AFM	Atomic-force microscopy
AGE	Advanced glycation end product
ANF	Atrial natriuretic factor
ANP	Atrial natriuretic peptide
AOPP	Advanced oxidation protein products
ApoA-IV	Apolipoprotein A-IV
ATR	Attenuated total reflectance
$BaSO_4$	Barium Sulphate
BNP	Brain natriuretic peptide
CaF2	Calcium fluoride
CKD	Chronic kidney disease
CFA	Correspondence factor analysis
CRP	C-reactive protein
CT	Computed tomography
cTnT	Cardiac troponin T
CVD	Cardiovascular disease
ECM	Extracellular matrix
ESRD	End-stage renal disease
FGF	Fibroblast growth factor
FPA	Focal plane array
FTIR	Fourier transforms infrared spectroscopy
Gd	Gadolinium
GFR	Glomerular filtration rate
GGT	γ-glutamyltransferase
H&E	Hematoxyline and eosin
hs-CRP	High-sensitivity-CRP
IL-8	Interleukin-8

KIM-1	Kidney injury molecule-1
L-FABP	Liver-type fatty acid-binding protein
LN-MRI	Lymphotropic nanoparticle enhanced magnetic resonance imaging
MDA	Malondialdehyde
MRI	Magnetic resonance imaging
MSCT	Multislice computed tomography
NAG	N-acetyl-β-o-glucosaminidase
NGAL	Neutrophil gelatinase-associated lipocalin
NT-proBNP	N-terminal brain natriuretic peptide
OCLs	Quantum-cascade lasers
OCT	Optical coherence tomography imaging
Ox-LDL	Oxidized low-density lipoproteins
PCA	Principle component analysis
PET	Positron emission tomography
PLS	Partial least square
PTX3	Pentraxin 3
SEM	Scanning electronic microscopy
sTNFrii	Soluble tumor necrosis factor receptor II
TAS	Total antioxidant status
TBARs	Thiobarbituric acid reactive substances
TGF-β1	Transforming growth factor-β1
TIMP-1	Tissue inhibitor of metalloproteinases-1
OCLs	Quantum-cascade lasers
UUO	Unilateral ureteral obstruction

Introduction

Chronic kidney disease is a progressive renal dysfunction, which loses renal function over time because of direct and indirect factors. Such as physical obstruction, microorganism infection and thickening renal tubules are the main direct factors; for indirect factors, the increased blood pressure, anemia and poor nutritional supply, mainly attributed to the complication are led by hypertension and diabetes mostly. FTIR imaging technique has been proposed to be a useful tool to characterize the chemical change of biosamples with pathological conditions. To define the histopathological changes of the kidney with CKD by 3D chemical FTIR imaging is helpful to investigate the molecular information of CKD tissue, especially focusing on the study of the renal unit, glomerulus.

In the present study, the imaging methodology of 3D FTIR imaging provides access to the chemical parameters of mapped tissue specimens of interest. By using several computational algorithm applied on the obtained spectral dataset of renal sample, the samples with different severity of CKD can be discriminated with the evaluation of lipid-to protein ratio, unsaturation level of F.A.C.s sub-molecules and barium sulfate, reflected to the morphometric change of glomerulus level.

The tasks of this thesis project is as the following:

1) To characterize the chemical change of renal tissue of CKD based on the spectral data obtained by FTIR soectramicroscopy
2) To image the compositional information of pathological renal samples for histopathological purpose by FTIR imaging
3) To discriminate the biochemical parameters of glomerulus level between pathological, its contralateral kidneys of a mouse with CKD and healthy kidneys with traditional and advanced algorithm applied on Spectral data
4) To discriminate the pathological severity of the kidneys during the CKD progression with multivariate data treatment of FTIR 2D dataset
5) To visualize the spatial distribution of chemical/molecular change of glomerulus level for characterizing the histopathological parameters attributed to CKD development.

CKD prevalence

Chronic kidney disease (CKD) becomes one of the major worldwide public health problems, due to its increasing number of afflicted patients as well as the poor prognosis of morbidity and mortality [1, 2]. In the United States, the prevalence of end-stage renal disease (ESRD) progressing from CKD is increasing exponentially [3]. The number of patients enrolled in the ESRD Medicare-funded program has increased from ~ 10,000 in 1973 to 615,899 in 2011. Patients with ESRD consume a disproportionate share of healthcare resources. In the USA, the total cost of the ESRD program reached $49.3 billion in 2011 [2, 3] and overall annual Medicare costs more than $75,000 per person, including expensive cares such as $32,922 for transplant patients and $87,945 for hemodialysis therapy. Despite the magnitude of resources

committed to the treatment of ESRD and the substantial improvements in the quality of dialysis therapy, patients continue to experience significant mortality, morbidity and reduced quality of life. The same trend was observed in Europe and certain developed countries in Asia, such as Japan [4].

CKD is particularly serious in Taiwan, where the incidence of ESRD is now the highest in the world. The prevalence of CKD increased from 1.99% in 1996 to 9.83% in 2003. The overall incidence rate during 1997 to 2003 was 1.35/100 person-years. However, the awareness of CKD is low in contrast to its high prevalence in society which increase the difficulty in earlier diagnosis.[5, 6]. The factors compounded with other increasing risk of developing CKD, include older age, diabetes, hypertension, hyperlipidemia, and the female sex [7, 8] , making this progressive disease an even more serious public health issue in Taiwan.

General information about the kidney

The kidney is a complex organ that is composed of a variety of different cellular structures. Its internal anatomy contains three main sections inward: the cortex, the medulla and the pelvis (Figure 1A) [9]. The blood carrying cellular wastes is filtered by renal units called “nephrons” (Figure 1B), located in the cortex, removing water-soluble entities into the urine. This blood filtering process takes place in the glomerulus, the microvasculature of the nephron, through mediating the surface charge of the glomerular basement membrane (GBM) and the pore size in the membrane of the glomerulus barrier [10].

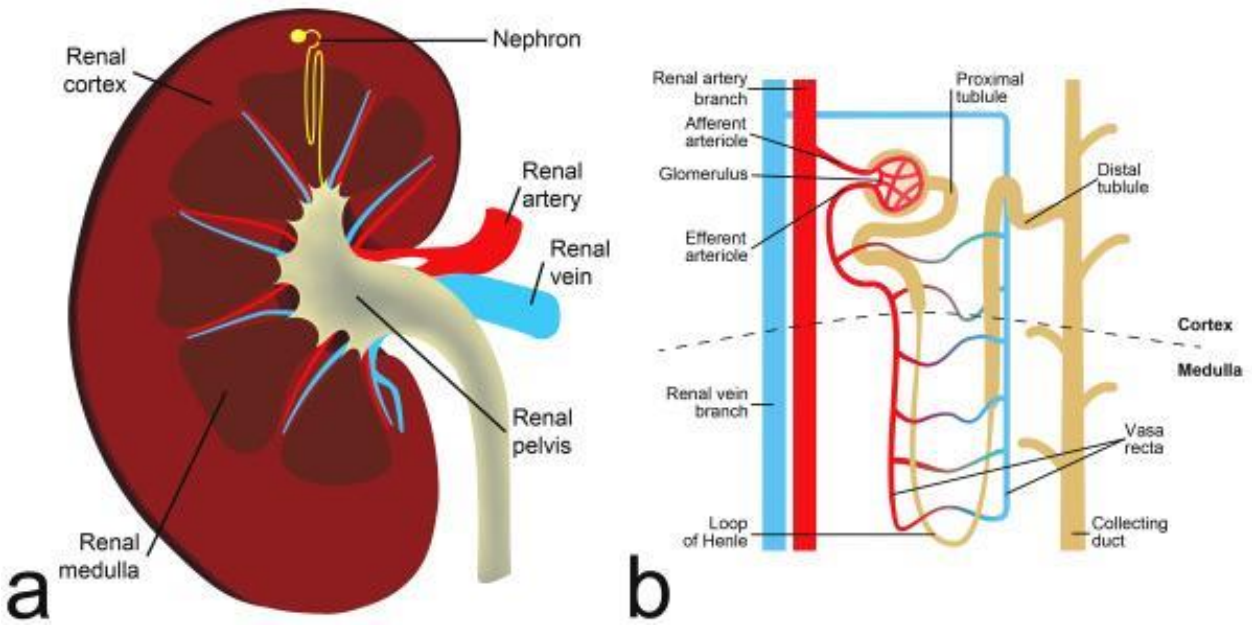

Figure 1. Schematic overview of the anatomy of a kidney. (A) Coronal section of the kidney; (B) schematic diagram of a nephron [9]. The nephron is the functional unit of the kidney. The glomerulus and convoluted tubules are located in the kidney cortex, while collecting ducts are located in the pyramids of the medulla.

The renal filtering efficiency of the glomerulus declines when it is subjected to stress from different origins or pathological conditions of the organs, which consequently could cause renal failure and further lead to the loss of kidney functions (Figure 2) [10].

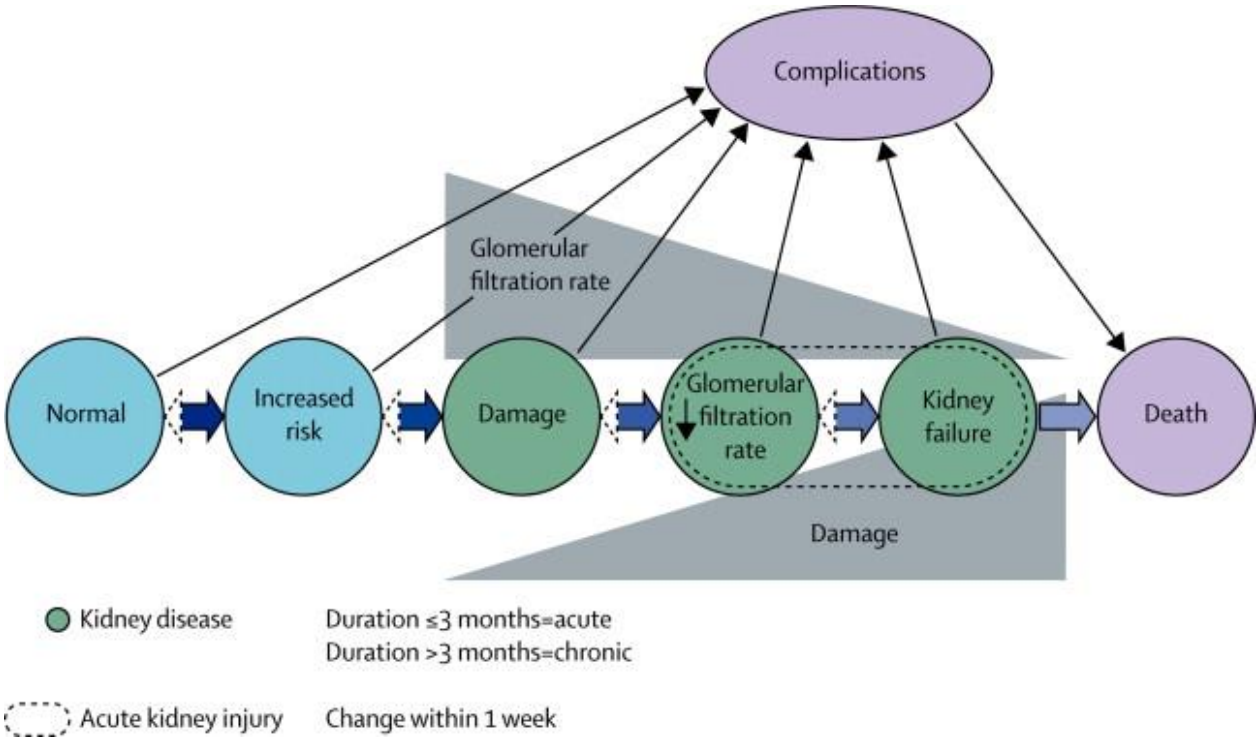

Figure 2. Conceptual framework for the progression of kidney injury. The risk factors for kidney damage (blue), stages of progression of kidney disease (green) and the complications and death (purple). Thick horizontal arrowheads represent the transition between the progression of kidney disorder and the outcomes to death. Dashed arrowheads represent the remission of kidney disorder which has less frequency than the progression. Solid black arrow lines represent the complications of kidney injury, which includes nephron disorder and cardiovascular disease. CVD, for example. Glomerular filtration rate (GFR) reduces as the kidney disease progresses, while kidney damage increases in severity [11].

The kidney pathologies often induce secondary pathologies in the body due to the accumulation of toxic entities that have not been properly filtered to be removed by urine [12]. The very complex anatomy-function correlation from macroscopic (organ) to microscopic (glomerulus) levels increases dramatically the difficulty in analyze the kidney pathology.

The kidney's function and body homeostasis

The kidney has several physiological functions that mediate the interactions of organs within the body, including endocrine secretion, metabolic activities (with glycogen storage for ex.) and the regulation of blood pressure; however, its primary role is the elimination of waste products. There are two ways the kidney controls the homeostasis of the body system: The first is by being the activator through proper functioning,

thus supporting systematic balance. The other is by being the target, receiving signals from other organ systems to activate downstream reactions. Consequently, the quality of kidney functions are strongly affected by a variety of disorders, including metabolic syndromes (diabetes, hypertension and obesity), immune-mediated injuries, dysregulation of hormone secretions (impaired balance of erythropoiesis), an impaired respiratory system (lung infiltration) as well as pathological conditions originating from the kidney itself (ex. glomerulonephritis, nephrosclerosis and polycystic kidney disease) [11]. The complications and disorders brought about by renal injury may further contribute to the progression of kidney damage: for example, cardiovascular disease (CVD)-induced chronic kidney disease [13]. On the other hand, the presence of renal disease usually initiates secondary diseases or worsens the progression of existing acute or chronic pathologies in patients. Some examples are given below (Figure 3).

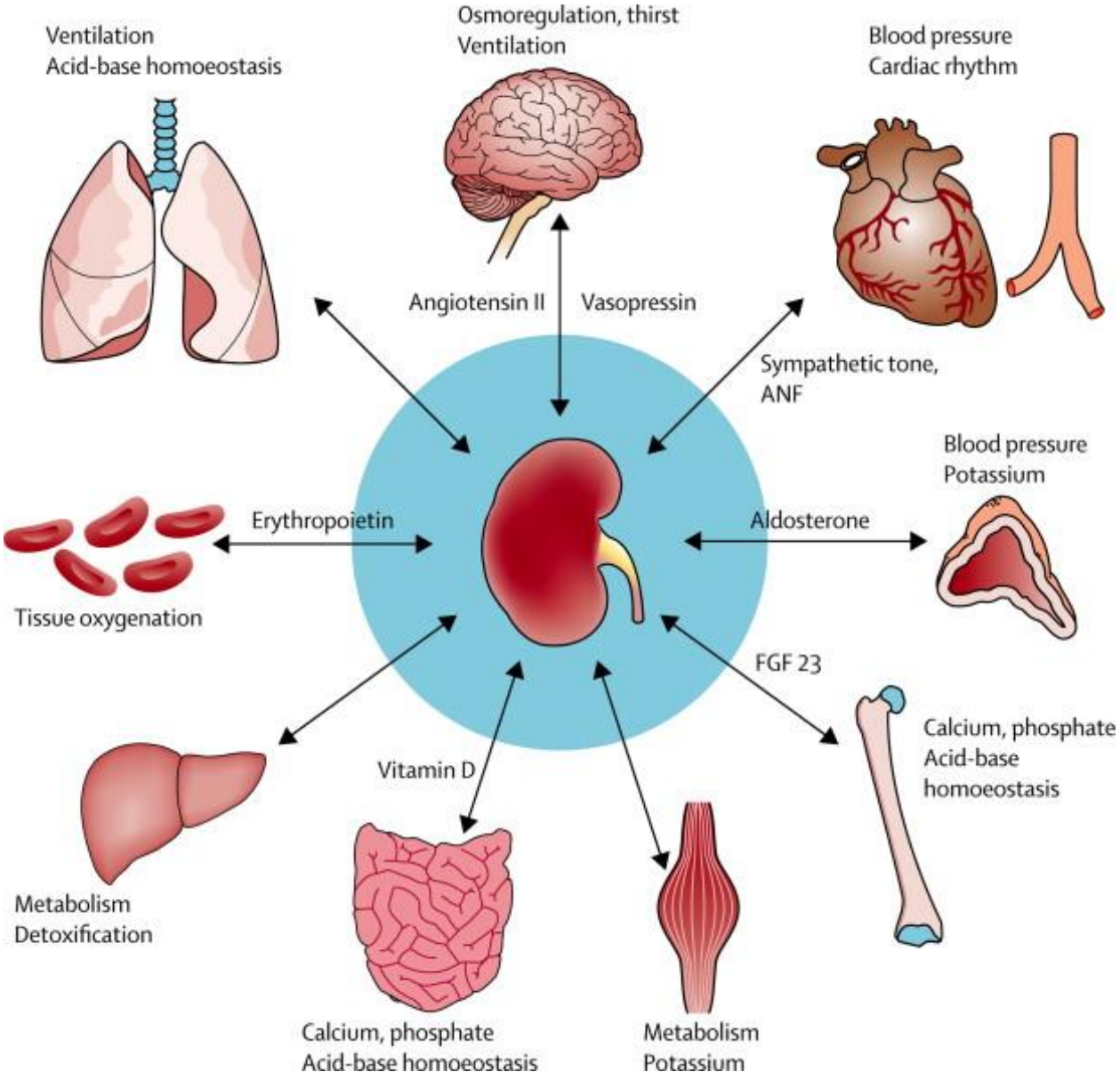

Figure 3: Kidney function on body homeostasis. The interactions between the kidney and other organ systems are mediated properly in order to maintain the systemic balance of body. FGF= fibroblast growth factor. ANF= atrial natriuretic factor [11]

The result from the wide interactions existing between the kidney and other organs is that many pathologies can affect the body' homeostasis, and thus make the appreciation of the physiological function of the kidney difficult. It is obviously more complex once a pathology occurs, either in the kidney to affect other organs, or from these organs to affect the kidney functions.

Defining chronic kidney disease

When a disease affects the kidney progressive renal injury can occur, and will later be followed by renal inefficiency and an impaired filtering function; this pathological development is referred to as 'chronic kidney disease' (CKD) [1, 14]. It is difficult to detect the early symptoms of CKD before the situation of the patient presents comorbid disorders [15]. During the progression of CKD, the disorders induce functional and anatomical alternations in the organ, which both interactively contribute to the complexity of CKD. The decrease in kidney function in CKD is primarily caused by the loss of functional nephrons, the basic units of blood filtration and cleaning [16]. The efficiency of glomerular filtrating activity is tied to the reduced amount of working nephrons, and has thus become a standard of estimating the level of kidney injury in CKD. In 2002, the National Kidney Foundation (NKF) gave a clinical guideline that proposes the definition of CKD based on the level of GFR, and created the classification of 5 stages to characterize the development of CKD (Table 1) [17-19]. In this report, CKD is characterized by a decrease in GFR to a level below 60 ml/min per 1.73 m^2 of average body surface area for at least three months' time, or a significant increase of biochemical markers in the urine (ex. albuminuria) of the patient. The latter is based on the structural injury of the glomerular membrane barrier, in which the permeability to macromolecules is altered, allowing for the appearance of proteinuria in the CKD patient.

Stage	Description	GFR (mL/min/1.73 m^2)
1	Kidney damage with normal or ↑ GFR	≥90
2	Kidney damage with mild ↓ GFR	60–89
3	Moderate ↓ GFR	30–59
4	Severe ↓ GFR	15–29
5	Kidney failure	<15 (or dialysis)

Chronic kidney disease is defined as either kidney damage or GFR <60 mL/min/1.73 m^2 for ≥3 months. Kidney damage is defined as pathologic abnormalities or markers of damage, including abnormalities in blood or urine tests or imaging studies.

Table 1. The stages of chronic kidney disease based on the estimated GFR value [19].

Renal failure in CKD

Numerous studies have confirmed as well as discussed the pathophysiological characteristics and the progression of CKD in human and established animal models [20-22]. The common features include appearance of fibrotic tissue, increased oxidative stress, inflammatory infiltration and cellular shape aberrations, which collectively contribute to the pathogenesis and progression of CKD [23]. Biomolecules - including DNA, protein, lipid, and carbohydrates - are usually subject to oxidative stress, and their alteration leads to dysfunction in cellular functions. Renal fibrosis is the most significant clinical outcome of a severe CKD, and it appears at the end-stage of renal function [24]. Renal fibrosis occurs progressively in either renal interstitium or glomeruli, and alters the renal parenchyma by forming scar tissue, which is mainly composed of collagens [25, 26]. The destruction of normal kidney parenchyma' tissue due to proliferated fibrotic components leads to a distorted function and structure of glomeruli, renal tubular and also causes microvasculature reductions, all resulting in the decrease of glomerular function. It finally results in the retention of fluids in renal tissue, as well as a hypoxic condition that is induced by impaired oxygen supply from scarred blood vessels [27]. However, the level of pathophysiological features in CKD does not only correlate with the estimated GFR in CKD patients [28]. Existing research indicates that increased oxidative stress and inflammation are observed to be prevalent in patients with CKD earlier in the course of kidney disease than previously recognized by the estimate of GFR, and these observations would not be closely correlated with estimates of GFR. Hence, there is a need to use a reliable methodology with sensitivity and quantitative value for determining the level of each biochemical parameter useful for staging the kidney injury in CKD, which will be especially important in the early detection of disease symptoms [29].

Glomerular patho-physiology

During the progression of CKD in human and animal models, the glomerulus is the most susceptible sub-structure of renal tissue [30]. Capillary-loop glomerulus, with its selective permeability to blood circulation, is the central functional part of nephrons in the kidney. The segmented renal tubule which collects filtered fluid from glomerular capillary is followed by the reabsorption of water and small molecules back to body (Figure 4). Blood filtration takes place in the glomerular part of the capillary tube, selectively transferring water-soluble molecules (urea, glucose, various salts, amino acids, and mineral ions) across the glomerular barrier but retaining high molecular weight plasma components and cells, like albumin and erythrocytes, forming the primary urinary fluid. The portals on glomerular barriers are a cluster of windows with diameters between 60-100 nm, which restrict the cross-traffic of blood-filtrated solutes with the selectivity in size and surface charge. Besides the glomerular capillary, the glomerular vasculature consists of afferent arteriole and efferent arteriole, which serve as the entrance and exit for blood flow in glomerulus, respectively. The ongoing afferent arteriole is of larger diameter than the outgoing efferent arteriole, which mediates glomerular blood pressure as a control system in regulation of GFR [31]. Each kidney holds approximately 900,000 to 1,000,000 nephrons in an adult human [32], depending on age, size, race, gender as well as birth weight [33]. A lower nephron number is considered as a risk factor in CKD, and the overloading of renal filtration in the remaining working nephrons is often a consequence, which further worsens the glomerular injury, and is followed by a loss of more working nephrons [20]. Thus pathologies in the kidney are mostly degenerative or evolutive.

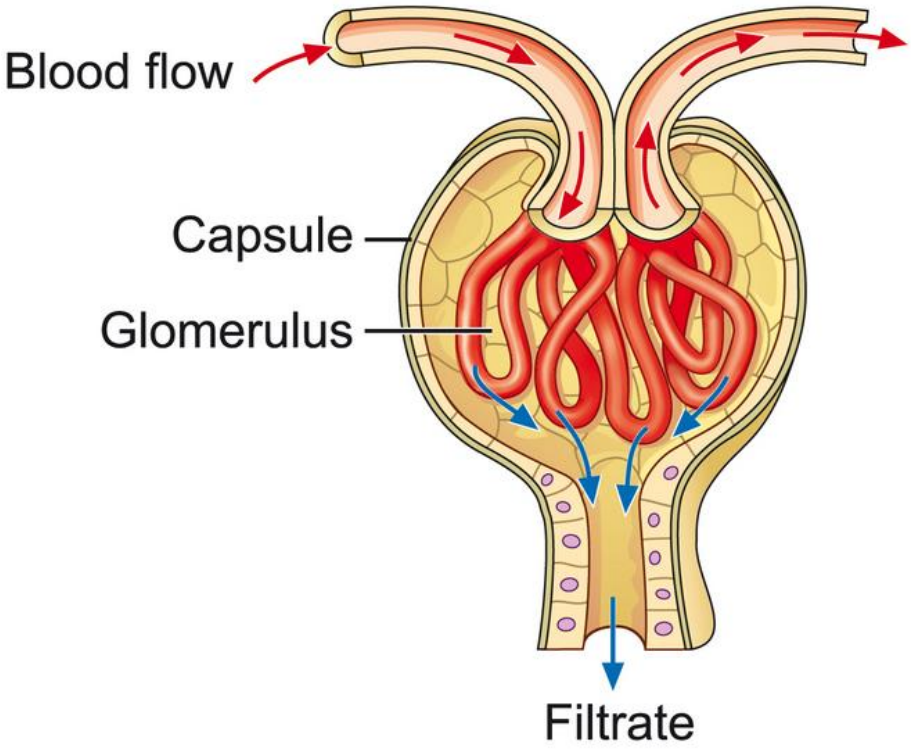

Figure 4. Cross-section of a glomerulus. The glomerulus is a tuft of capillaries located within Bowman's capsule of the kidney. Blood enters the capillaries of the glomerulus by an arteriole called afferent arteriole and leaves by an efferent arteriole. The capillaries are lined by a layer of endothelium cells that has a unique structure, allowing blood components to be filtered and resulting ultimately in the formation of urine (http://www.fmc-renalpharma.com/the_kidneys.htm).

Degenerative glomerular efficiency

Numerous renal disorders involve glomerular injury, which can be unspecific histopathological features of proliferated scars, thickened glomerular membrane, macrophage infiltration and cell proliferation in the renal parenchyma [34]. Most evaluating methods rely on histological or fluorescent staining on prepared tissue specimen. The pathogenesis of glomerular lesions refers to the fibrotic scarred or hyaline-deposited glomerular vasculature in glomerulosclerosis (ref). The inflammation of the glomerulus refers to glomerulonephritis, characterized with hyper-cellularity. Under the conditions of injury, the thickening of the impaired Bowman's capsule membrane causes the decreased diameter of the vascular pole of glomeruli, or the urinary pole of Bowman's capsule. The glomerular function impairment thus represents the outcomes of the filtration inefficiency, proteinuria, and uremia.

The activated signal pathway responding to increased oxidative stress, inflammation and fibrosis in renal degeneration promotes the renal functional deterioration that triggers abnormal cell growth, cellular death of necrosis and apoptosis as well as alternates the selective binding capability or permeability of regulator protein in mediating cellular processes. Abnormality of fibroblast growth may occur in the renal tubule, glomeruli and the renal artery or veins, which in turn affect the reabsorption and blood circulation within the

kidney, reducing glomerular efficiency. The transformed cellular shape may exhibit a different structure due to increased oxidative stress, causing abnormal tissue architecture. A report from the study of urinary obstruction-induced renal damage has indicated elevated levels of oxidative stress and a diminished amount of anti-oxidant catalases within the kidney. On the other hand, increasing oxidative stress and inflammation in turn promotes the progression of renal dysfunction.

In histopathology, glomerular lesions have several categories based on the patterns of glomerular injury, either in geometry or in origin site, such as the extent of injured glomeruli in the kidney (focal or diffused), the pathological level of injured glomeruli (segmental or global) and whether the lesion originated from glomeruli, or was spread into glomeruli (glomerulonephritis or glomerulopathy). The geometric pattern of glomerular injury is thus much reliant on the examination of morphological change on a large amount of individual glomeruli in the kidney, to differentiate the glomerular pathology.

Glomerular importance in CKD

Most research studies the level of kidney injury through the examination of molecular change, via genetic and cellular experiments in biopsies and structure alternation. This is done through optical microscopic imaging in 2-dimensions (2 D). Histopathological approaches to evaluate renal pathology have performed well in clinical trials and medical studies by providing contrast between signal visualization evidence with staining, and preliminary quantitation of renal specimens. A variety of highly specialized types of cells are in charge of maintaining renal homeostasis in the kidney, and the structural change as well as the functional variation of these types of cells are tightly integrated to generate the net extent of kidney function. However, the structural complexity of glomeruli and its associated glomerular filtration remains the barrier for the incomplete conclusion of glomerular injury, which is strongly correlated with renal function in traditional approaches. The score of renal tubule lesions and interstitial injuries examined in the histopathological results represent the limited correlation with glomerular conditions.

The reports show that the glomerular volume in the kidney represents an indicator of glomerular injury, as the glomerular disorder does not exhibit symptoms in the histopathological level at the beginning of renal impairment. The change of size, shape, and microstructure of glomeruli thus makes a great contribution to the examination of glomerular injury, especially in some glomerular diseases. Therefore, reaching a more accurate reflection of renal function via scoring the glomerular injury comes down to the requirements of morphometric information of glomeruli provided by imaging approaches. In facilitating the exploration of glomerular architecture within visualization artwork, the task of reconstructing the full 3D characteristics of anatomic and functional alternations is turning to be the key target of current bioimaging methodologies.

Justification of GFR and other markers of the kidney in clinical and experiment studies

As the increasing prevalence of CKD has been observed in the developed countries of the world, the new pathological methodology for detecting CKD in its early stages as well as its severity is becoming an important issue concerned by nephrologists. Current histological protocols used widely in clinics are usually assigning GFR tests and urine assays for proteinuria [35, 36]. In the evaluation of CKD severity, GFR value is the most common indicator of renal function, but not tightly related to the early structure alternations in the kidney which would identify the subtle damage [37]. Many aspects of physiological factors about glomerular, tubular, and interstitial tissue can contribute to the occurrence of proteinuria, and the significant structure damage of renal tissue usually appears before the proteinuria is measureable [38]. The GFR estimation for diagnosing renal function typically measures the variance of the many molecules involved with the system disorder, which are usually associated with renal function. Several molecular studies also contributed to the finding of potential biomarkers related to kidney disease with some desirable properties [39]. Table 2 lists the molecules that have been discussed for the involvement with renal disorders [40]. The category of biomarkers listed is on the basis of pathological mechanism.

	Biomarker
Kidney function (GFR)	Cystatin C
	β-Trace protein
Tubulointerstitial injury	NGAL
	KIM-1
	NAG
	L-FABP
Glomerular injury	Podocin
	Nephrin
	Podocalyxin
Endothelial dysfunction	ADMA
Oxidative stress	Ox-LDL
	AOPP
	TBARS
	Plasma and urinary F_2-isoprostanes
	MDA
	Protein reduced thiols
	TAS
	Protein carbonyls
	AGE
	Urinary 8-hydroxydeoxy guanosine
	4-hydroxy-nonenal
	Antioxidant enzyme activities (e.g., superoxide dismutase, glutathione peroxidase, catalase)
	GGT
Inflammation	CRP and hs-CRP
	PTX3
	sTNFrii
	IL-18
	Tenascin
	TIMP-1
Fibrosis	TGF-β1
Cardiovascular dysfunction	ANP
	BNP and NT-proBNP
	cTnT
	Adrenomedullin
Metabolic disorders	Adiponectin
	FGF-23
	ApoA-IV

Table 2. Renal biomarkers involved with pathological progress [40]. Abbreviations: ADMA, asymmetric dimethylarginine; AGE, advanced glycation end product; ANP, atrial natriuretic peptide; AOPP, advanced oxidation protein products; ApoA-IV, apolipoprotein A-IV; BNP, brain natriuretic peptide; CRP, C-reactive protein; cTnT, cardiac troponin T; FGF-23, fibroblast growth factor-23; GFR, glomerular filtration rate; GGT, γ-glutamyltransferase; hs-CRP, high-sensitivity-CRP; IL-18, interleukin-18; KIM-1, kidney injury molecule-1; L-FABP, liver-type fatty acid-binding protein; MDA, malondialdehyde; NAG, N-acetyl-β-o-glucosaminidase; NGAL, neutrophil gelatinase-associated lipocalin; NT-proBNP, N-terminal brain natriuretic peptide; Ox-LDL, oxidized low-density lipoproteins; PTX3, pentraxin 3; sTNFrii, soluble tumor necrosis factor receptor II; TAS, total antioxidant status; TBARS, thiobarbituric acid reactive

substances; TGF-β1, transforming growth factor-β1; TIMP-1, tissue inhibitor of metalloproteinases-1.

The clearance rate of endogenous plasma substrates in blood and urine

Analyzing body matrices like blood and urinary biopsies in order to evaluate the amount of plasma substances provides a flexible and easy access point to quantify the variations of global renal function from the two kidneys of patients. Several biomolecular clearances rates such as creatine and insulin are evaluated within 24 hours, with the standard method for estimating GFR serving as the estimation indicator when considering acceptable applications in hospitals for most patients, as well as the preliminary assay in laboratory studies. However, the goal of pursuing more accurate analysis representing detailed information of the renal function still remains. The poorer quantitative measurement of determining GFR value represented by standard equation is attributed to the heterogeneity of race, sex, and the nature of the individuals as well as age of the patient. The other issues in performing standard biopsy methods include the time-consuming nature of analysis procedures, the limited availability in obtaining biopsies of some patients as well as emerging cases of the patient.

Bioimaging approaches for CKD

Different imaging modalities provide a way to monitor the complexity, diversity and the distribution of systematic disorders of the patients on the respect of morphology and function (Figure 7) [41]. Methods such as X-ray CT [42], magnetic resonance imaging (MRI) [9, 43], positron emission tomography (PET) [44], optical microscopic imaging (confocal fluorescent imaging, two-photon imaging [45], optical coherence tomography imaging (OCT) [46]), ultrasonography [47] and scanning electron microscopic (SEM) imaging are applied to visualize the renal parenchyma in the examination of glomeruli, renal tubules, renal arteries/veins and other renal tissue. Table 3 illustrates a comparison of the imaging techniques, performed on the kidney. The advantage of these imaging modalities is the ability to provide detailed structural and functional information on tissues and organs. The noninvasive characteristics of some imaging techniques exhibits the capability of visualizing full 3D reconstructions of renal vasculature, with or without additive imaging agents depending on imaging instruments.

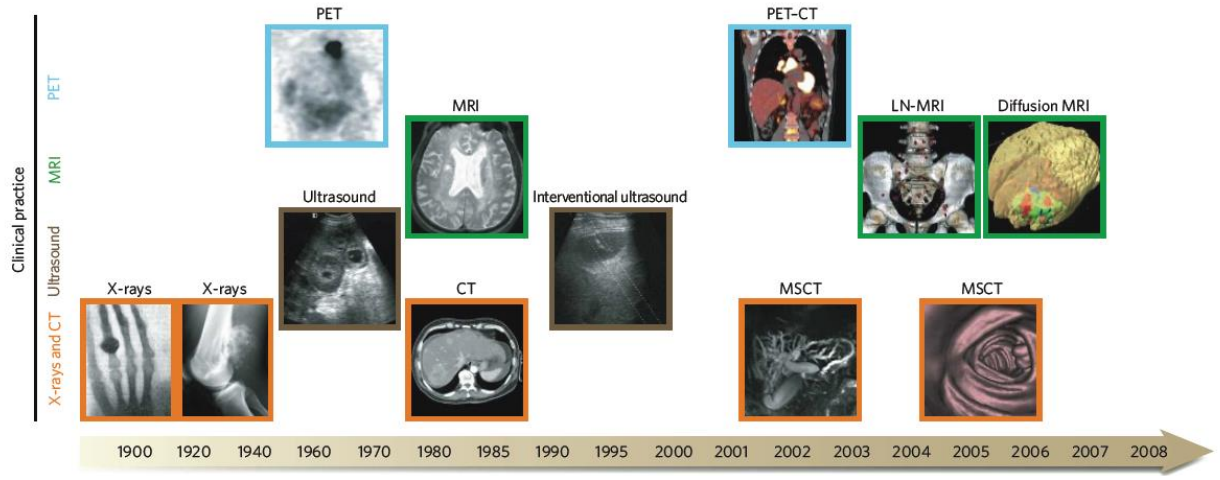

Figure 7. Imaging techniques used in biomedical research. Many macroscopic imaging technologies (shown above the timeline) are in routine clinical use, and there have been huge advances in their capabilities to obtain anatomical and physiological information since the beginning of the twentieth century. Shown here are some examples of bones (X-rays), soft tissue (ultrasound, MRI and CT rows), 3D organs (CT and MRI rows) and physiological imaging (MRI and PET rows) [41]. MSCT= Multislice computed tomography. LN-MRI= Lymphotropic nanoparticle enhanced magnetic resonance imaging.

Technique	Resolution	Time	Depth	Multi channel	Imaging agent used	Clinical use	Reference
X-ray CT	50 µm	Minutes	No limit	No	Iodinated molecules, Barium particles, Carbon dioxide	Yes	[42, 48]
MRI	10-100 µm	Minutes to hours	No limit	No	Magnetic chelates, Magnetic particles	Yes	[9, 43]
Ultrasound	50 µm	Seconds to minutes	cm	No	Microbubbles	Yes	[49]
PET	1-2 mm	Minutes to hours	No limit	No	^{18}F-, ^{64}Cu- , ^{68}Ga- or ^{11}C-labelled compounds	Yes	[44]
Multiphoton fluorescence imaging	1 µm	Seconds to minutes	200 µm	Yes	Photoproteins, Fluorochromes	No	[45]
Intravital microscopy	1 µm	Seconds to minutes	< 1 cm	Yes	Photoproteins, Fluorochromes	Not yet	[50]
OCT	5-10 µm	Seconds to minutes	1-2 mm	No	No need	Not yet	[46]

Table 3. Overview of imaging system performed on renal studies.

X-ray computer tomography

CT, equipped with an X-ray light source, is an imaging tool that has the high penetration capabilities to create 3D reconstruction visualizations of imaged subjects in clinical and medical research [51-54]. The interior structure of a sample examined by X-ray CT is globally extracted to differentiate the anatomic features of soft tissue and hard tissue (ex. bone skeleton) via phase-contrast signal, due to the difference of refractive index between cellular components of tissues [55]. For example, in bone imaging, X-ray micro-CT is used as an accurate tool to precisely measure changes in bone stereology, volume and micro-architecture. Thanks to the 3D information extracted from biosamples while using micro-CT imaging, CT provides a feasible access to quickly and effectively assess phenotypic parameters of soft tissue [56].

Vascular imaging in small animal is also made possible by either injecting blood contrast agents for *in vivo* imaging microvascular anatomy (Figure 5), or by *in vitro* casting vasculature with silicon-based compounds [57, 58]. 3D volumetric imaging of microvasculature within the organ or the tumor allows for statistical examinations of the physical parameters within blood vessels in a quantitative manner, as well as the ability to observe the 3D architecture of vascular system while the organ remains intact. Hence, X-ray micro CT technology provides a means to explore the microvascular network, even with disease conditions in development.

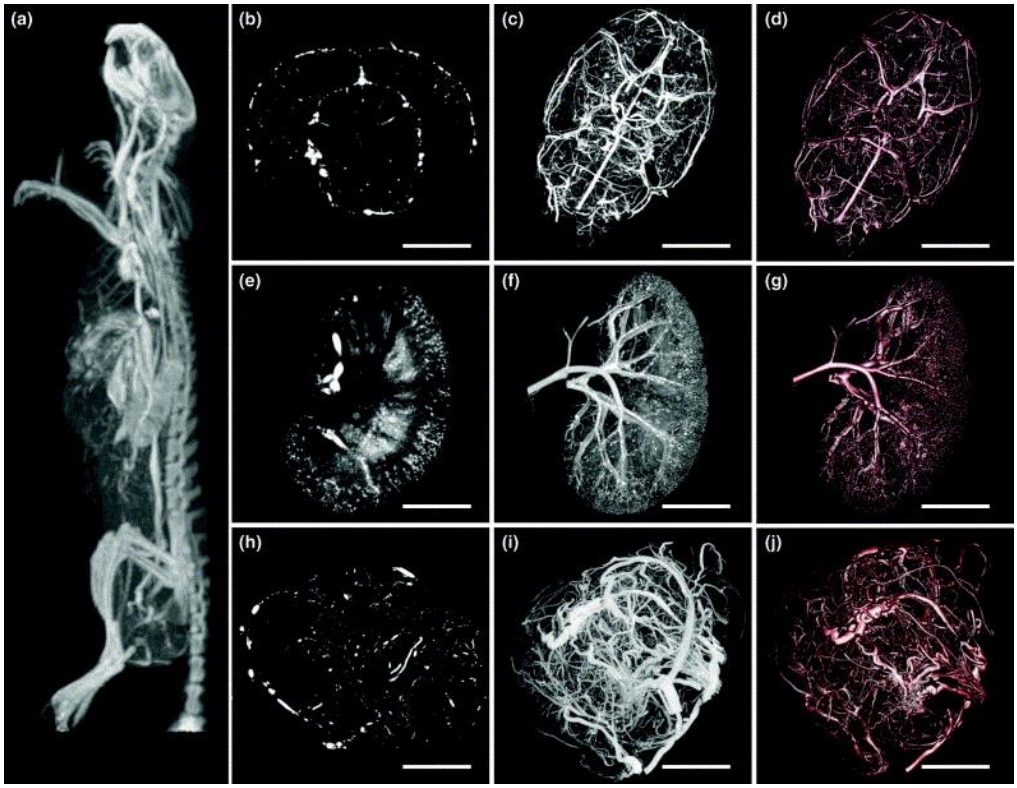

Figure 5. Micrographs of micro-CT images in vasculature imaging. (A) A micro-CT projection through a clinical CT image of the intact rat. A mammary fat pad tumor of 1.5 cm was developed in this animal. The visualization of microvascular network in the brain (B-D) and kidney (E-G), and abnormal vessels within the tumor (H-J) [59]. (B, E and H) are the projections of multiplanar reformatted images. (A, C, F and I) are the maximum intensity projections. (D, G and J) are the projections of volume rendering. Scale bar is 0.5 cm.

Magnetic resonance imaging based morphometric analysis of glomeruli in whole kidney

Recent renal studies using MRI imaging techniques show significant achievements in the examination of glomerular morphology and functional information [60-62]. Highly biocompatible MRI contrast agents are perfused into vasculature for in situ and in vivo bioimaging, followed by the quick elimination of contrast agents in 24 hours; which makes the later observations with other experiments workable without destruction damage [63-65]. The advantage of MRI imaging is that it holds the capability of creating a 3D quantitative

visualization of glomeruli, via labeling with MRI contrast agents against GBM in small animal models and human kidneys [62, 66].

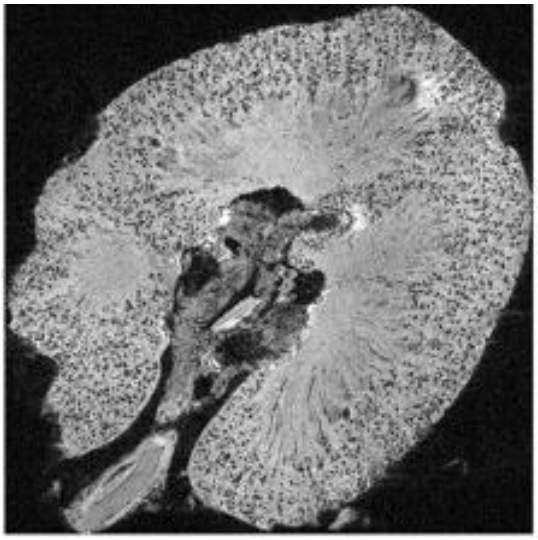

Figure 6. Micrograph of a 2D projection of 3D MR image of a human kidney injected with labelling image agent for the visualization of glomeruli. The MR image exhibited dark spots throughout the renal cortex of the agent-labeled kidneys. Each dark spot in the cortex is ~50–80% darker than the surrounding cortex [43]. Field of view = 6 × 10.5 cm^3

Quantification of glomeruli in normal or diseased kidneys entails the examination of glomerular size, the total number and the pattern of distribution in a whole kidney of a dog, a rat and a human, respectively, based on in situ measurement of MRI data. This includes each glomerulus in kidney, and not the estimation used in stereology performed in histology [43, 62, 67]. Though there is a difference in afore mentioned information between MRI and stereology [68], it is important to note that the bias of estimation or measurement in different methodologies, and the heterogeneous nature of each kidney from the individuals [69]. The perfusion efficiency and leaking level of the MRI contrast agent within glomeruli is further examined to describe the histopathological change of correlation with glomerular morphology in some reports [61]. Architecture disorders of glomerular capillary, epithelial podocytes and glomerular basement membrane somehow contribute to protein leakage, reflecting on MRI image data by the distribution of the imaging contrast agent in the examined kidney.

Image processing and statistical analysis of the MRI signal should be preprocessed to eliminate noise inference and set a proper threshold for digital data computing, which may need supporting information acquired by other methodologies. The reports also indicated the concern of separating MRI signal changes from the blood- or the MRI contrast agent- artifacts that reduce false signals of glomeruli. The reconstructive digital data based on nondestructive sample preparation represents quantitative analysis in micrometer resolution, and takes significantly shorter time than that of the stereological method.

Renal ultrasonography morphology

Ultrasound (US) imaging in clinical use as well as medical studies has been frequently used to visualize the interior structure of many organs, and also to monitor the stage of disease progression in small animal models and human [70]. The advantages of US imaging is that it is an inexpensive and noninvasive imaging modality that can be used in clinical diagnosis. Renal ultrasonography is a feasible modality in diagnosis and prognosis for evaluating renal size, renal mass, and symmetry (shape) of the kidney in the patients (Figure 7) [47, 71, 72]. Another advantage of ultrasonography for bioimaging is the usage of contrast agents such as microbubbles to compensate for the limitation of low sensitivity in small blood vessels (< 2 mm in diameter), and provide an access point to perform serial examinations of the patient's target disease [73]. Using contrast agents in ultrasonography prevents the interference from any movement of examined objectives, which may cause artifacts recorded in the data [74].

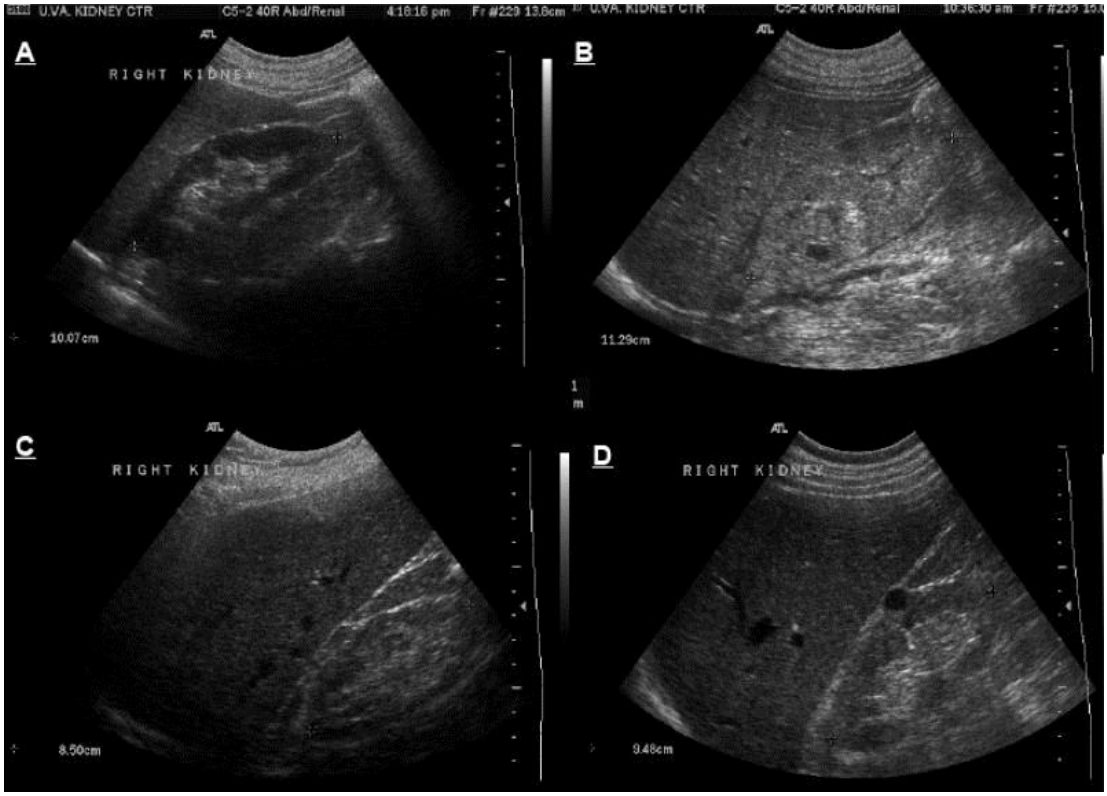

Figure 7. Ultrasonography of the kidney. (A) normal kidney, (B) enlarged and echogenic kidney with loss of differentiation between cortical, medullary and sinus fat compartments in a case with acute kidney injury, (C) small, slightly echogenic kidney with thin cortex in a patient with chronic kidney disease and (D) normal size but echogenic kidney with a single simple cyst in a patient with chronic kidney disease secondary to diabetic nephropathy. [47]

High blood flow in the kidneys make US imaging quite suitable to be applied in the examination of renal vasculature. The morphological information of the whole renal vascularity, including the renal artery, sub-

capillary as well as renal hemorrhage can be revealed by the enhanced-Doppler signals of US imaging, and provides a fast and easy way to identify of vascular disorders and lesions in the kidney [49]. The global quantification work of renal vasculature is possible to reach in 3D US imaging with contrast agent-enhanced US imaging [75, 76]. The accessibility of US imaging coupled with physical microbubbles in clinical use has been why it has been proposed to study kidney impairment, but the renal function should be taken into concern, and not without regard to patient's renal condition. However, lower resolutions, sensitivity and specificity of US imaging either in laboratory work or clinical use remain the barriers of fine examination in kidney studies. No report of US imaging shows the glomerular anatomy and function, though there are some studies that claim the supplementary role in diagnosing glomerular disease [77]. Exposure to mechanical ultrasound in the kidney can cause capillary hemorrhage of nephrons, leading to the consequence of nephron injury, observed in some reports [78, 79].

Microscopy techniques in histology

Hematoxylin and Eosin (H&E) staining as a basic tool for histopathology

Using the H&E method to stain biosamples is the most common method, routinely used in histology to identify cellular components of tissue, and also to distinguish tissue morphology. The advantage of the H&E method in histopathology is to provide a well-acceptable standard by well-trained pathologists for determining the presence of disease, disease grading and the measurement of disease progression. As of recently, there are proposals of using automated computational methods in detecting and segmenting image datasets to perform the histological identification of shapes and topology on a series of 2D images, to be used in reconstructed image work [80, 81].

With the counterstaining of the nucleus in purple, and the eosinpholic structure in a different grade of red with chemical dyes, the classification of cellular components and the identification of the anatomic features of the tissue is aimed towards discriminating the markers for the pathological state, on the basis of the relevant analysis through light microscopy. Figure 8 exhibits the architecture of glomeruli and the renal tubules of the healthy kidney, and a pathological kidney damaged by the uptaking of mercuric chloride ($HgCl_2$), examined by histopathological H&E staining [82].

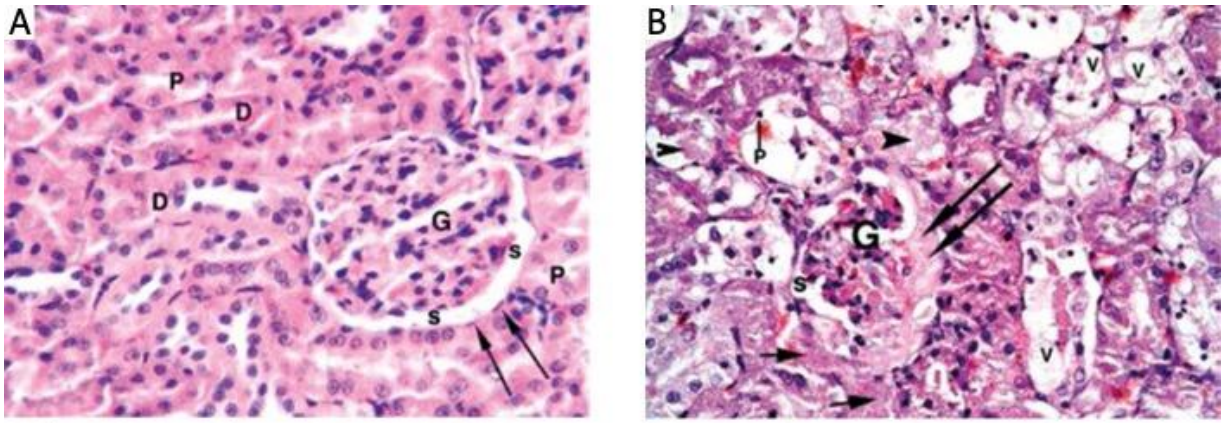

Figure 8. H&E stained micrographs of renal tissue. (A) Normal glomerulus (G), parietal layer of Bowman's capsule (arrows) and urinary spaces (s) in a control rat. Note: normal proximal convoluted tubules (P) and distal convoluted tubule (D) (H + E; 400×). (B) Interstitial exudate (short arrows), shrunken glomerulus (G) with fluid exudate (long arrows) filling the urinary spaces. Note: Cytoplasmic vacuolation (V); pyknotic nucleus (p) with intra-luminal cast formation (arrowhead) of the tubular epithelium in a rat fed with $HgCl_2$ [82]. Fold= 400X

Fluorescent imaging of glomeruli for functional study

Through usage of fluorescent probing in the various molecules participating in structural organization and physiological processes, the mechanism and morphology involved can be examined with quantitation and visualization. Very specific labeling, with fluorescent probes directly against the molecules provides a reliable indication for representing the inherent information of biological samples. Thanks to the innovations of optical and physical developments in imaging modality, multiphoton image data is collected in sharp, high resolution, and with deep optical imaging capabilities greater than ten micrometers, which is the limited thickness for confocal laser imaging. When applied to in vivo animal imaging, the optical depth of imaging is demonstrated to be up to 150 μm below the surface, while imaging dissected thick specimens is around 1 mm via optical dissecting in z-axis with optimized focal depth step. To our understanding, multiparametric analysis of physiology and anatomy in biopsies offers a practical way to build 3D visualization of physiology in glomeruli via various labeling markers imaged by multiphoton microscopy. As another way, a simple fluorescent imaging without specific recognition can be performed to represent a glomerular structure by injecting fluorescent material into blood vasculature system (Figure 9) [83].

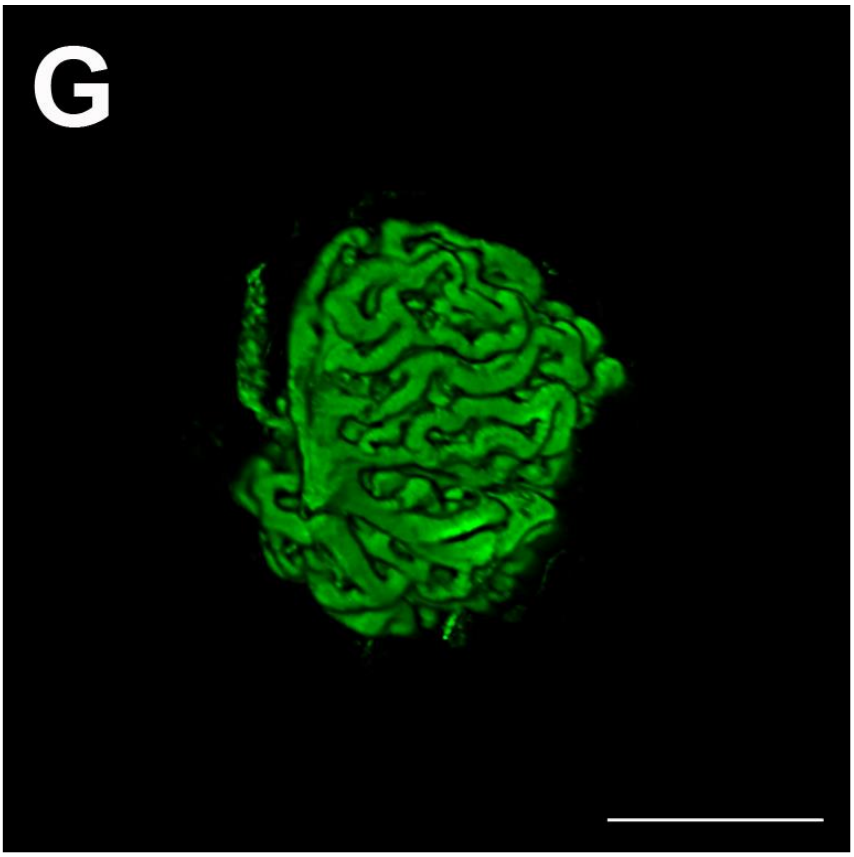

Figure 9. Micrograph of fluorescent microangiography of a glomerulus in kidney. The kidney was perfused with the mixture of agarose and fluorescent microspheres before imaged by confocal fluorescent microscopy. The image represents of a 3D reconstructed projection of a glomerulus [83]. Scale bar = 100 μm

Alternative method: Morphological visualization of glomerular vasculature by corrosion casting-based investigation

Corrosion casting methods coupled with optical microscopic instruments have been used to study the microvascular architecture of biosamples such as tumor tissue, the brain, liver and kidney [84-88]. By perfusing resin particles that preserve the shape of blood vessels within the biosamples, the morphological variation of vasculature related to pathological states is stereologically examined to verify the grading of the disease, and locate the distorted vascular position. The reconstructed imaging of blood vessel networks of the casted biosamples is established by a variety of imaging modalities, such as SEM and X-ray microscopy [87, 89]. Recent studies indicate that the corrosion casting method, coupled with ultrahigh resolution Nano-CT X-ray microscopy, have shown improved imaging quality, with sub-micron resolution in the 3D geometric visualization of renal microvasculature (Figure 10) and glomerular capillary loop(Figure 11) [90].

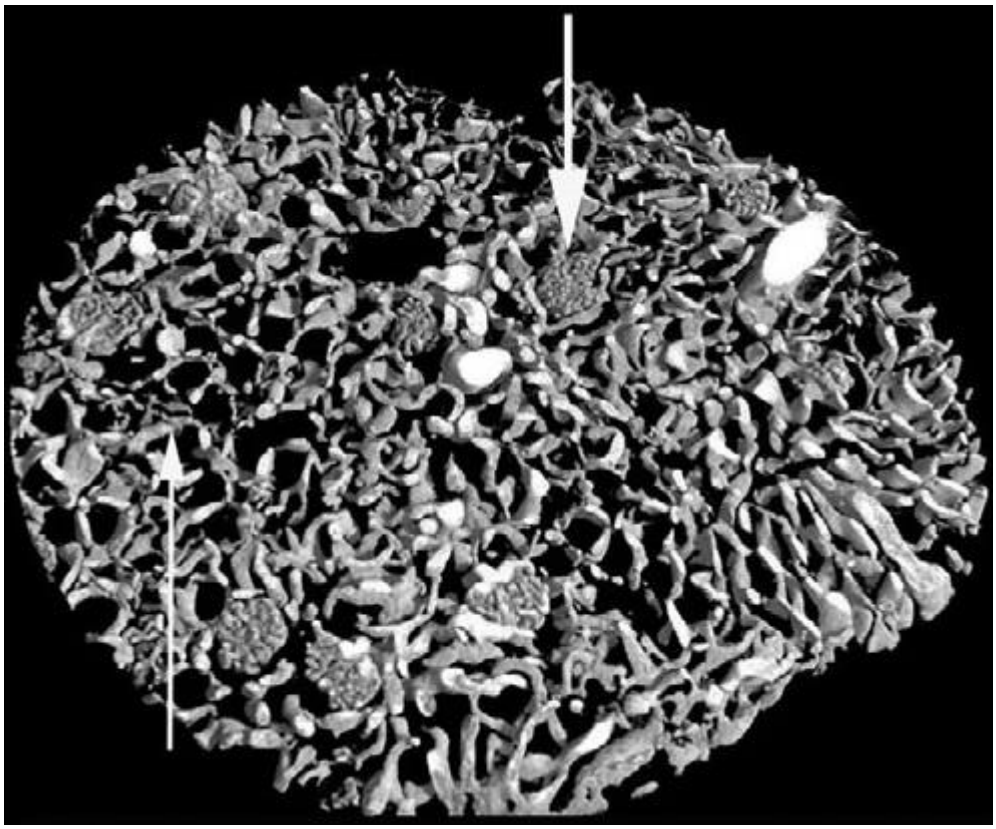

Figure 10. The reconstructed micrograph of a dissected region of casted kidney by Nano-CT. The capillaries of the glomeruli were resolved (large arrow) as well as peritubular capillaries (small arrow) which were irregular in shape and surrounded blank spaces normally are occupied by the proximal and distal tubules of the kidney [90]. Voxel resolution is 0.77 μm.

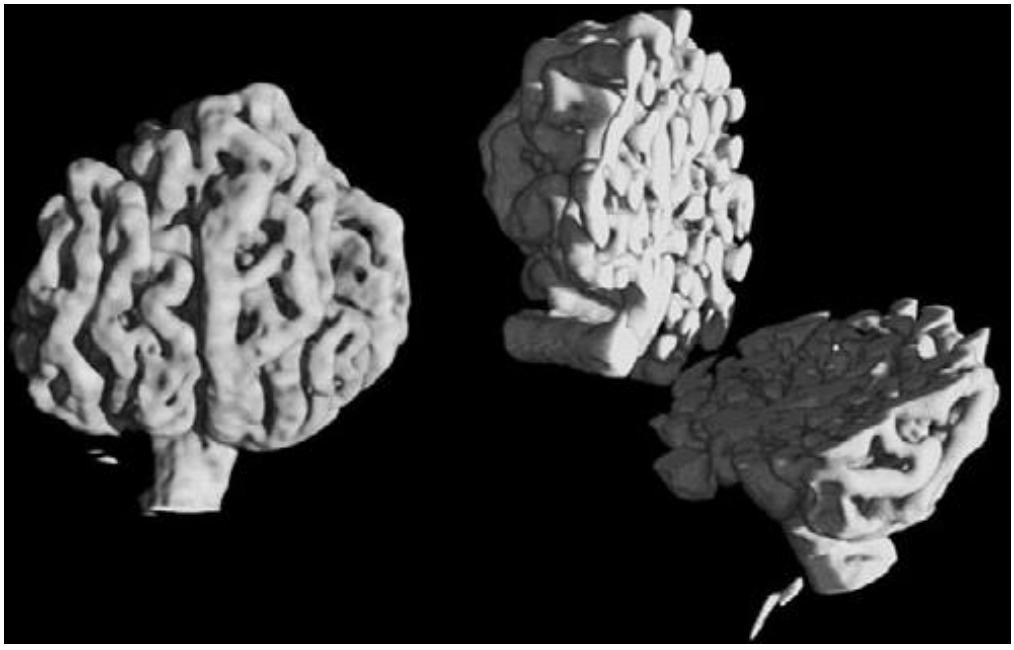

Figure 11. The reconstructed micrograph of a casted glomerulus by Nano-CT. Branched capillaries were clearly resolved (Left). The model was also available to view the interior of a glomerulus (Right) [90]. Voxel resolution is 0.5 μm.

Clinical imaging techniques for evaluating renal function in CKD

Medical imaging with proper tracing compounds are considered to be helpful in identifying the causes of CKD, as well as being able to characterize the features of CKD patients (Table 4) [91]. The method of measuring the kinetic curve of gadolinium (Gd) chelates contrast agent by MRI is used to trace glomeruli in certain studies [92, 93]. The time-density signals of contrast tracers by MRI could be useful for the estimation of functional imaging, with the statistical analysis of quantification of perfusion, quantification of glomerular filtration rate, estimation of tubular function. These measurements could parameterize renal function and/or renal morphology while using such contrast agents injected into kidney. With real-time 3D visualization of kidney morphometry, it is possible to access the activity of a single kidney on the basis of intrarenal tracer kinetics and differentiation between the global GFR of each kidney within patients. The examination of an MRI agent's clearance in a specific kidney may feasibly allow for a more accurate diagnosis of renal disease, for both clinical management and reference information.

Similar to kinetic MRI measurement, another imaging option used to estimate the GFR value in a single kidney is the X-ray tomography, with a contrast agent for monitoring dynamic glomerular function based on tissue and vasculature density kinetics. The Renal Mass Index gathered by CT scanning acts as a potential indicator of GFR value, which exhibits high correlation with the measurement through clearance of iopromide. Absolute quantitative measurement of the concentration of a CT contrast agent in a perfused kidney allows for real time monitoring in GFR over time, as well as providing the anatomic information through angiography.

The potential limitation of imaging modalities in estimating GFR is the injection of contrast agents into the patients in clinics. Allegory response and nephrotoxicity induced by injected contrast agents may result in negative effects of renal disorder, especially those with poor renal efficiency.

IMAGING STUDY	*WHAT THE STUDY HELPS IDENTIFY*
Plain-film radiography of kidneys, ureters, and bladder	Ureter or bladder stones
Renal ultrasonography	Kidney size, obstructive kidney disease, polycystic kidney disease
Renal Doppler ultrasonography	Renovascular disease, renal vein thrombosis
Radioisotope renal scanning	Individual kidney function, renovascular disease, obstructive uropathy
Computed tomography	Kidney mass or complex cyst
Magnetic resonance angiography	Renovascular disease
Renal angiography	Renovascular disease, renal artery thrombosis/thromboembolism, polyarteritis nodosa
Retrograde ureterography	Upper urinary tract obstruction

note: *Intravenous pyelography generally is not performed in patients with chronic kidney disease because it may precipitate acute renal failure.*

Information from references 1 and 28.

Table 4. Imaging options in chronic kidney disease.

Emerging technique: Infrared spectral imaging in biochemical analysis

General information of IR spectromicroscopy

Electromagnetic waves of infrared (IR) radiation span between the red end of the visible light, to the starting end of microwaves (780 nm to 1000 μm wavenumber), and is composed of three parts, recognized as near-IR, far-IR and mid-IR, respectively (Figure 12). For IR spectral investigation in biological specimens, the most commonly useful region is the mid-IR region between the wavelength 2.5 μm to 25 μm, corresponding to the frequency region in the unit of reciprocal centimeters, from 4000 cm^{-1} to 400 cm^{-1}. In the mid-IR region, the IR vibrational spectrum observed on biosamples contain many unique features of organic contents, which absorb a specific frequency of mid-IR radiation to enter the resonant state. The energy absorbed by intra- or inter- molecular bonds generates the periodic motion, resulting in a net charge in the dipole of electron density between the atoms of chemical groups within molecules, which is in turn related to atomic masses and the strength of chemical bonds. Therefore, this spectral variation is useful in the differentiation

of disease disorders through the analyzing of collected IR spectra signals. The advantage of Fourier transform (FT) IR spectrometers, coupled with microscopy for biomedical studies are thus becoming an analysis method with reproducible measurements on the sample, with spatial analytical capabilities of biochemical components of specimens, free-labeling from tracers in samples, and most importantly, the ability to acquire structural or functional signals of the biological components in their natural state.

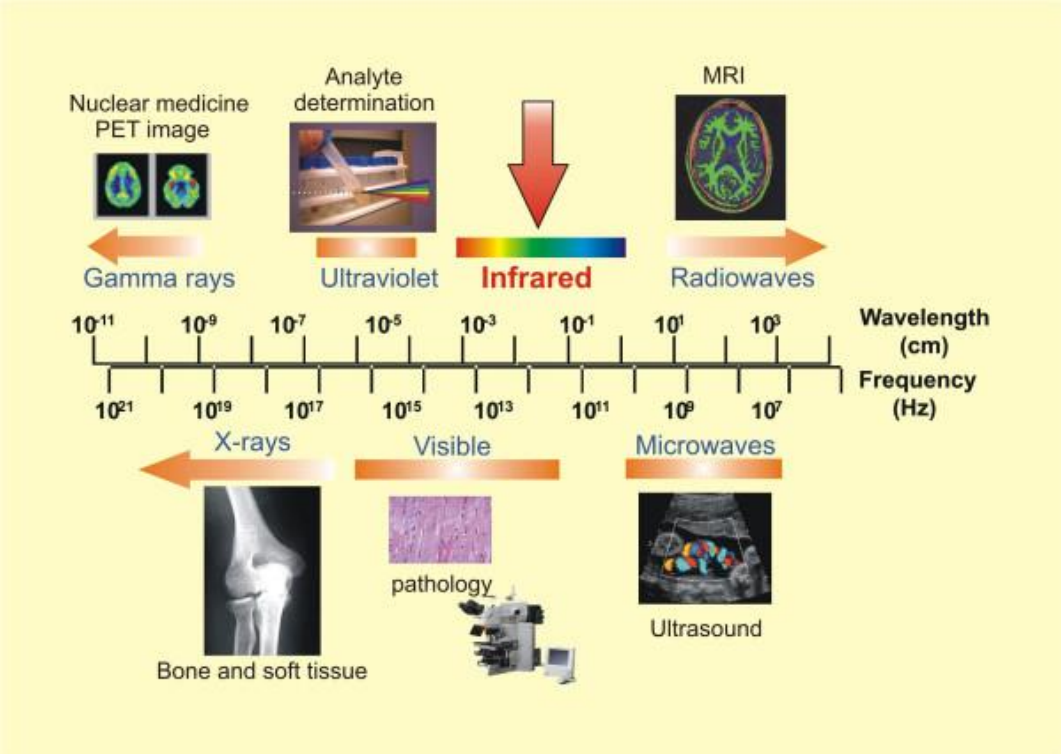

Figure 12. Electromagnetic spectrum of wavelength and frequency and it bio-applications. Here is a classical electromagnetic spectrum aligned with its common and established biomedical imaging application. IR region is located between visible and microwave regions with indication of red arrow [94].

FTIR spectral information in biological samples

The vibrational models of the molecular family of the biosamples can be quantitatively measured by mid-FTIR spectroscopy. For biological specimens, the most useful spectral regions are 1200-900 cm^{-1} for carbohydrates, 1700-1480 cm^{-1} for protein and 3050-2800 cm^{-1} for lipids (Figure 13) [95, 96]. The recorded wavenumber of specific molecules families of biosamples are quietly constant but the overlapping of the absorptions between different molecular families is observed because various molecules existed within the biosamples. Proteins mainly contribute to the absorption on Amide I region which peak is basically around 1650 cm^{-1} (the most vibrational mode is C=O stretching plus C–N stretching and N–H bending) and Amide II region which peak is basically around 1540 cm^{-1} (N–H bending and C–N stretching). Lipids majorly contribute their absorptions to several interval regions such as one is for C-H stretching vibrations on the

interval of 3050-2800 cm^{-1}; another is for C=O stretching vibration peaked around 1740 cm^{-1}. The absorption of glycogen is majorly around 1030 cm^{-1}. The PO^{-}_{2} stretching vibrations attributed from nucleic acids are peaked around 1080 cm^{-1} for symmetric vibration referring to ν_s (PO_2^-) and around 1225 cm^{-1} for asymmetric vibration referring to ν_{as} (PO_2^-) [97]. Position and intensity of the absorption spectra (or bands) are determined by the molecular and/or conformational structure (ex. α-helix, β-sheet, β-turn and random coils of protein secondary structure [98]) of these components within the biosamples. These unique fingerprints of absorption spectra are useful to identify biochemical compositions of the biosamples and provide the information about the nature, the content, and microenvironment of the bio-components [99].

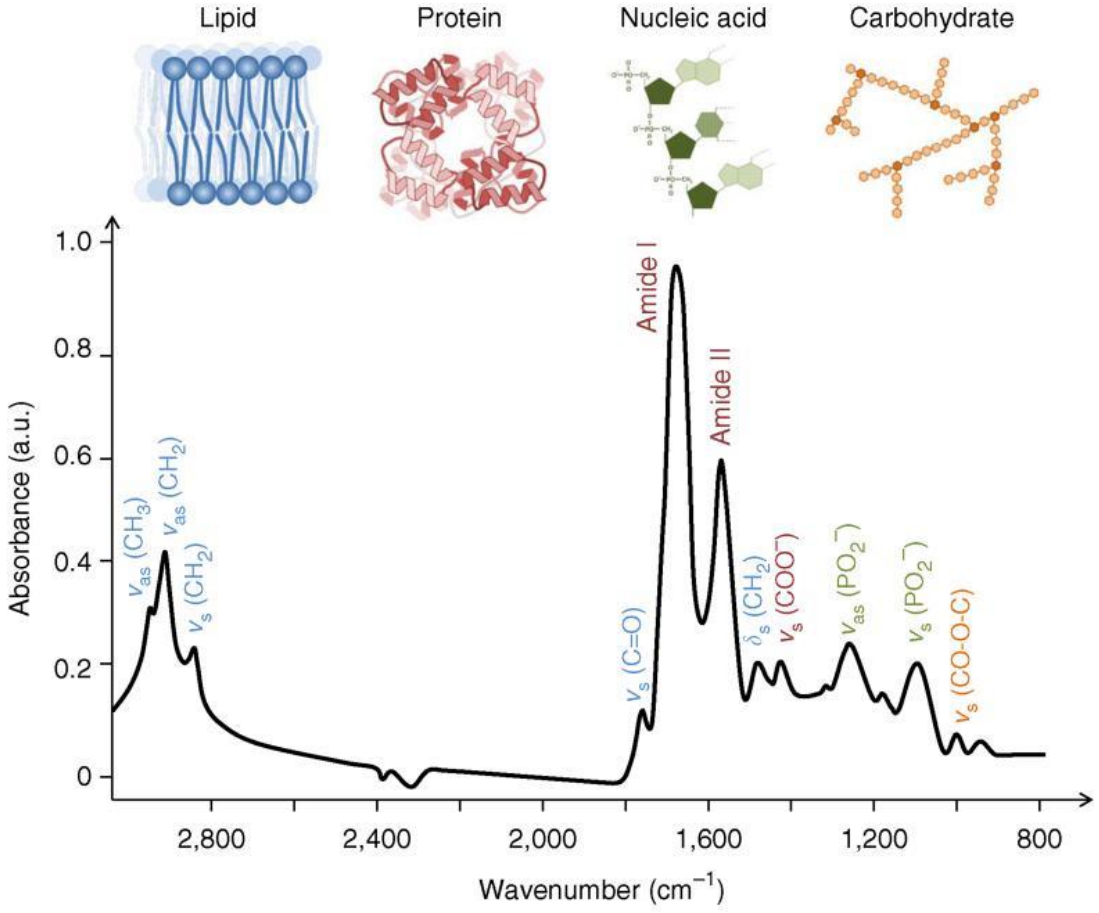

Figure 13. The typical biological spectrum on the spectral interval of 3000 cm^{-1} to 800 cm^{-1}. Major biochemical components of biosamples are assigned in their proper position on the spectrum. ν for stretching vibration; δ for bending vibration; s for symmetric vibration; as for asymmetric vibration [95].

FTIR imaging system

Modern FTIR spectro-microscopy has three major components: the IR light source, the interferometer and the detector to couple with the computer, in order to save the large data acquisitions composed of the whole of spectral information (Figure 14). A thermal light source such as a tungsten carbide Glowbar is a

convenient bench-top source of IR, providing continuous polychromatic IR radiation, which generates a wide range of frequencies spanning broad bands from 500 to 4000 cm^{-1}. A monochromic laser IR source focuses on a narrow range or a single frequency. Other available choices for IR light source are quantum-cascade lasers (QCLs) [100, 101] and synchrotron X-rays [102, 103] with the benefit of improved imaging quality [104]. For the imaging purposes of IR instruments, a detector with multi-channels arrays and a focal panel array (FPA) is equipped to perform microscopy for the faster collection of data, with over 4096 (64x64) pixels and more with each data acquisition [105]. These types of IR sensitive detectors are composed of a large number of small detectors arranged on a grid-like pattern, similar to the mapping system. For a sample model using IR spectromicroscopy, transmission, reflection and attenuated total reflection (ATR) are generally available for the users depending on the experiment requirements and sample characteristics.

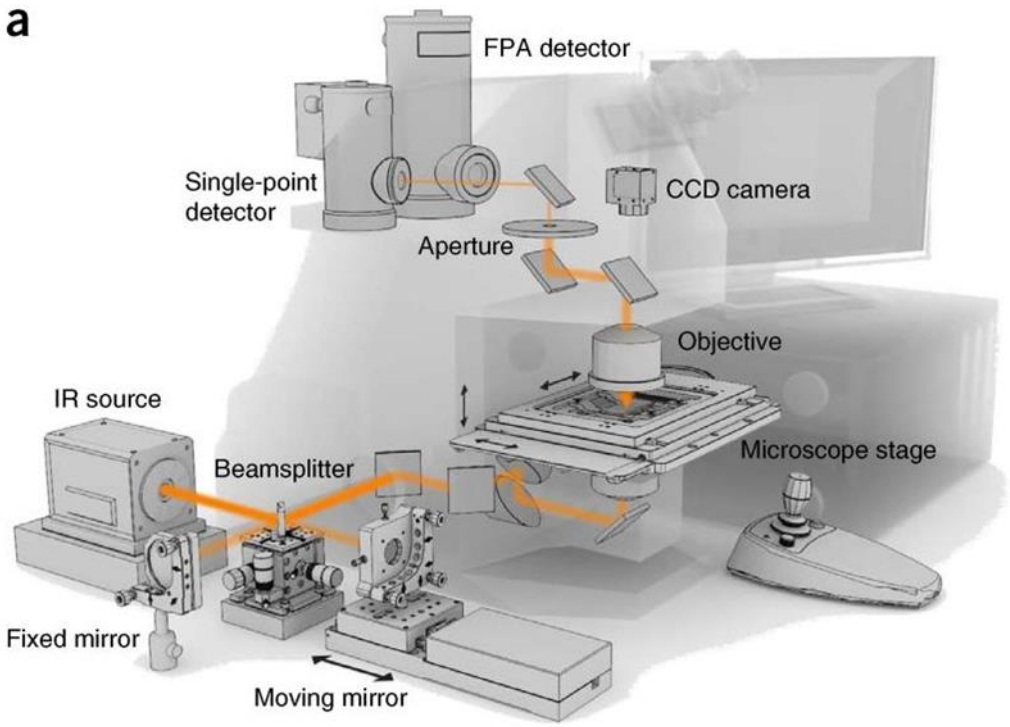

Figure 14. The schematic layout of FTIR spectro-microscopy. The instrumentation of this FTIR modality represents the general purposes, which includes transmission and the reflection model of sample configurations (only the transmissions model is shown in the layout), dual detectors for point mapping and imaging mapping, external interference and computer for data acquisition and processing [106] .

During the data acquisition of pixel spectra obtained from each grid point of a setting pattern by IR spectro-microscopy, equipped with a FPA detector, the individual spectral pixel renders the images corresponding to each wavenumber of a selected region. This presents a spectral work in term of FTIR imaging, which combines the spectral multiplexing and multichannel detection of optical microscopy (Figure 15) [107]. For bioscience, FTIR imaging on biosamples provides a resolved information pool specifically supported by the chemical characteristics examined from the spectra of complex tissue or cells [108, 109].

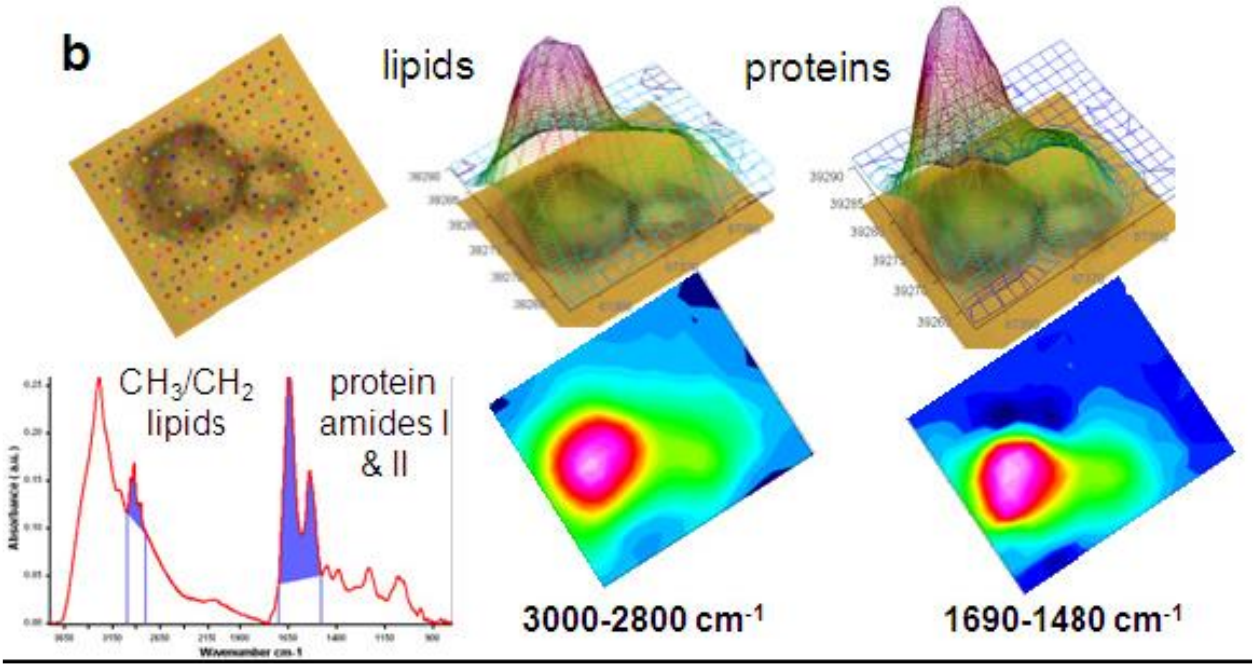

Figure 15. The 2D mapping of the individual formalin-fixed or air-dried cells by micro-FTIR. The FTIR images of the cells are plotted by representing the integration of spectral intervals from a series of spectra, collected point by point scanning a selected area [107]. For the spectral range of 3000-2800 cm^{-1}, the plot represents of the lipid intensity by the ratio of CH_3 to CH_2 groups in lipids; for the interval between 1690 cm^{-1} and 1640 cm^{-1}, the protein content is represented by the integration of amide I and amide II region.

Biomedical application of FTIR imaging

Since several decades ago, IR spectroscopic technique has been extensively used as an analytical tool in biological studies, the usage includes biofluids and complex tissue. In a few early studies, non-imaging IR works on the differentiation of tumor markers and the DNA features of cell lines. Xenografted tumor cells and tumor tissues gave examples of identifying pathological state [110, 111]. The development of microscopy allows this IR technique to not only be an alternative optical platform for histopathology in the laboratory, but also a promising technique in clinics [112, 113]. FTIR imaging modality is becoming able to routinely and rapidly provide high-quality data for experiment use, as well as be easily accessible to users [114].

Thanks to the technique innovations for IR modality, the improvements such as better sensitivity and spatially resolved information for chemical characterization of the biosamples as well as high throughput data recording makes this imaging approach be receiving an address for diagnostic and prognostic purposes. FTIR image data provides the morphological and biochemical information of the biosamples, which was thought to be useful in clinics. IR measurement on biofluids is also an ideal approach with the advancement of fast and non-invasive sample collection potential biomarkers for clinical purposes [115]. By using such methods, spectral fingerprint data of biofluids is available for histological classification by

computational data treatment [116, 117].

The art of 3D FTIR imaging technique on histopathology

Histopathological methods for classifying FT-IR imaging data have been developed only recently [118, 119]. The algorithm is aimed towards acquiring high confidence levels by using a large amount of tissue samples. The optimal set of data metrics was incorporated with an algorithm with diagnostic potential. Then, this model is applied on the FT-IR image data treatment. Spectral and spatial information extracted from each data point of the FTIR image dataset are used to determine the presence of the disease and its severity. In traditional histological methods, supervised classification is performed on the chemically stained data, followed by classification by an expert pathologist for setting the gold standard. The combination of classifying the FT-IR imaging data coupling, added with H&E stained visible image data is believed to provide further improvements in tissue segmentation. For the first step, the image data is aligned and overlaid sequentially. This can be done by using a smoothing filter to identify rough shapes and/or morphological features. Segmentation and feature extraction algorithms then process the combined data sets. This method can thus yield highly accurate classification results on the basis of morphological and chemical information in 3D.

Why combine X-Ray tomography and FTIR imaging for CKD analysis?

The study of CKD animal models by X-Ray tomography has reached an unprecedented level of performance at the Nano-X Laboratory in Taipei. Using intense X-Ray beams (synchrotron radiation), a 3D analysis of glomeruli distribution in kidneys has become feasible in 3D (Figure 16). However, the glomerulus cannot be characterized with the respect of GFR and their micro-environment. Combining a chemical microscopy technique with high-resolution X-ray tomography imaging has thus received attention, and its prospects at being able to complete the 4D information consisting of 3D morphology, and spectral characteristics at the glomerulus level of the kidney are also promising.

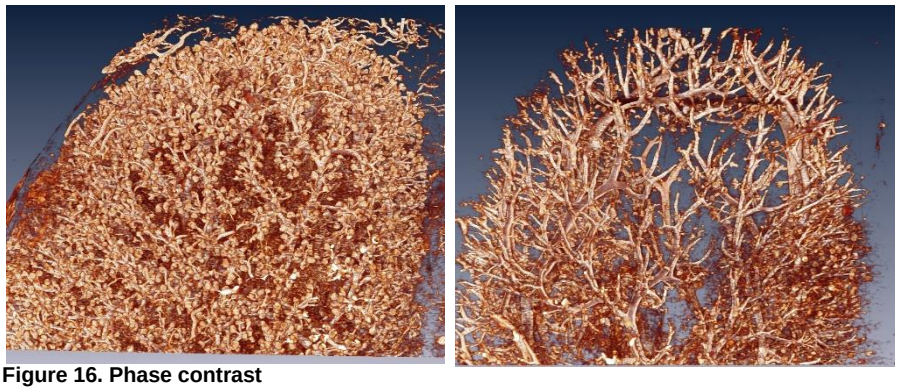

Figure 16. Phase contrast microradiographs of healthy and pathological kidneys.
The number of glomeruli is obviously higher in healthy kidney (left) and accompanied by a denser microvasculature in the cortex than observed on the pathological specimen (right) - (unpublished data – Academia Sinica).

Our preliminary work by using FTIR imaging has shown the result of a structural, metabolic, molecular parameter on renal specimens (Figure 17), although it was limited to 2D analyses and at the single glomerulus level. We obtained preliminary evidence that several biochemical differences could be highlighted by FTIR microscopy between a healthy kidney and one that is pathological.

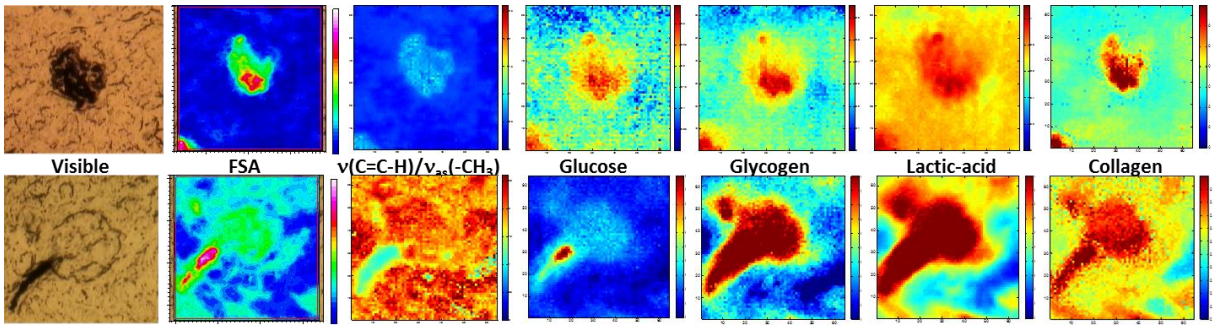

Figure 17. Example of biochemical, molecular and structural parameters found discriminant between healthy (top) and pathological (bottom) mice kidney samples by FTIR imaging. Diabetic nephropathy model in *db/db* mice. Left to right: Visible image (10 µm-thickness, 171x171 µm area with a glomerulus); Full IR absorbance image (FSA: 3900-900 cm^{-1} – scale 200 - 950); Oxidative stress level in tissue exhibited by $_{\nu}$(C=C-H)/$_{\nu as}$(-CH_3) absorption ratio (scale 0 - 2.6); glucose distribution (1033 cm^{-1} band – scale 0 - 0.35); glycogen distribution (1025 cm^{-1} band– scale 0 - 0.65); lactic-acid distribution (1127 cm^{-1} band– scale 0 - 1.1) collagens distribution (1637 cm^{-1} band– scale 0 - 0.35).

Objectives

Current pathological methodologies used in laboratories and hospitals remain as insufficient quantitative diagnosis, with limited 2D information in renal epidemiology. Most imaging techniques performed in renal studies are very reliant on indirect measurement of chemical substrates, injected into or against tissue specimens to acquire histopathological information. To date, 3D FITR imaging could be proposed as a potential approach to evaluate the multiple parts of chemical/molecular information based on probe-free techniques, in order to provide global information of a sample specimen for histological purposes.

The objective of this PhD thesis project is to use FTIR imaging to investigate the biochemical difference and morphological changes of the glomerulus level present in the kidneys of mice with CKD. We use functional algorithms of spectral clustering and spectral curve fitting to quantitatively differentiate the variation of the spectral features and the content of functional groups ($-CH_2$, $-CH_3$ and -C=CH) in fatty acyl chains (F.A.C.s) molecules inherited in renal specimens. The results are based on the 3D measurement of consecutive renal biopsies of the mice, with CKD examinations using the practical potential of 3D spectral imaging in the renal histopathology with geometrical examination.

In our work, we first studied the difference of lipid and protein content between a pathological kidney and its contralateral kidney of mice with CKD, and a healthy kidney of a control mice that has not undergone surgery. To distinguish the histopathological change in renal specimens of mice with different levels of CKD, the characteristic absorptions of lipid molecules on -CH stretching region and protein Amide I region, respectively, is analyzed to discriminate the biochemical change of glomerular region and non-glomerular region in renal specimens. Then, based on unpublished work in our laboratory about the estimation of the multi-parameter algorithm, we proposed to analyze the 3D geometric variation of molecular content change and the globally spectral characteristics in F.A.C.s molecules in glomeruli. The aim of this study is to characterize the pathological glomeruli of the kidney at the different level of stress (days 4 to 14 undergoing UUO) based on the spectral chemical characteristics.

The last part of the objective in this thesis is to evaluate 3D FTIR imaging in examining 3D glomerular morphology with disease progression. In the previous work of the laboratory, we found that filling blood capillaries with barium sulfate microparticles was a superb way to mark the microvasculature position in tissue organs. Thus, we propose to discriminate the 3D morphological change of glomeruli based on the characteristic absorption of barium sulfate injected into the renal blood system.

Methodology

The PhD thesis work is part of a bilateral research program between the Inserm U1029 laboratory in Bordeaux and the Nano-X laboratory of Academia Sinica in Taipei. The main aim of this bilateral project is to setup a multimodal imaging facility using common contrast agents to merge images from different imaging modalities, and the usage of common data treatment methods to ensure a combination of sample information obtained from different sources. The two major techniques developed in this context are the X-Ray and IR microscopies, both for obtaining 3D images of biosamples, from cells to animal models and for human biomedical research purposes. In the future, the goal will be to analyze biospies or surgical exereses, where the imaging methods will be applicable to provide relevant information about the sample, notably for diagnostic purposes.

This methodology section thus aims at defining how we could proceed in developing animal models suitable for multimodal imaging, i.e., applying both X-Ray and IR microscopy techniques, which imaging contrast agent could be used for such multimodal image acquisition; and how an infrared microscopy methodology has to be developed in order to reconstruct 3D chemical images of the biosamples.

Animal experiments

In present work, we used the mouse model of CKD, initiated through physical surgery of unilateral ureteral obstruction (UUO). Chronic renal injury was induced in B6/C57 male mice by obstructing one ureter for up to 14 days. In this work, the UUO model initiated a rapid sequence of events in the obstructed kidney, leading to reduced renal blood flow and GFR within 24 hours. At the time points of 4, 9 and 14 days after UUO, the obstructed kidney of the mice had varying degrees of hydronephrosis. In the past, one of the advantages of the UUO model was the presence of the contralateral kidney as a control sample in the experiment. In the present study, the contralateral kidney is considered another experiment group for verifying the renal and/or glomerular functions in UUO mouse model.

The experimental mice were euthanized and processed with injection of PBS saline solution to drain out the blood. The kidneys were collected immediately after perfusing the animals with a prepared imaging agent solution (barium sulfate, $BaSO_4$) and were frozen in liquid nitrogen. Sample preparation for tissue imaging was performed by cutting the kidney into sections 10-µm thick using cryostat set at −20 °C. Tissue sections were subsequently placed on CaF_2 IR-transparent slides and left to be completely dehydrated at room temperature.

Imaging contrast agents

Contrast agents in bioimaging techniques provide a direct visualization of targets of interest. When the

imaging technique reach a microscopic resolution, it becomes feasible to trace the functional part of the vascular system of an organ or the whole body, limited by the field of view of the technical setup. The digital information revealed by an imaging agent in a biosample can be processed with different computing algorithms to quantitatively evaluate histopathological features. For example, when using X-ray imaging to examine the vasculature of an organ, small-size gold nanoparticles (Au-NPs) can be used to image the morphology of individual blood vessels, which are further collectively compared by appropriate statistical methods. Another contrast agent, $BaSO_4$, is a good candidate for examining the vasculature of a tissue or an organ, but due to the larger dimension of NPs (∅ ≥ 1 μm), it is not likely that all microvessels can be imaged in this way. These imaging contrast agents have not been associated with a significant toxicity in live animals after IV injection. Thus, a microscopic view of the vascular system in tissue and organs is feasible. It allows for generating quantitative information about the vascular network, such as the density, the angles of branching point per volume, the dimension of blood vessels and change in their diameter…etc. Our previous publication has shown that using Au-NPs and $BaSO_4$ to image tumor vasculature is efficient in discriminating different tumor phenotypes in small animal models by FTIR imaging [120].

In present studies, the $BaSO_4$ microparticles suspended in the sucrose solution is washed with PBS saline solution three times, to replace the sucrose solution with PBS solution before used in vessel perfusion. This work of resuspending $BaSO_4$ in a physiological buffer is thought to preserve the physiological balance of blood vessel during perfusion treatment.

FTIR imaging

Data acquisitions

Consecutive tissue sections were obtained from a mouse kidney to allow the stacking of 2D images and full glomeruli reconstructions. After cryosectioning (10-μm thick tissue sections), every tissue section was deposited on a CaF_2 window (2-mm thick) and analyzed by FTIR imaging, using an Hyperion 3000 spectral imaging system equipped with a Vertex 80 spectrometer (Bruker-Optics, France), a liquid-N_2 cooled focal plane array (64×64 elements 40×40 μm each) detector, and a SuperGlowbar source (18V – 6-mm diameter at detector position). A ×15 magnification level and condenser were used for obtaining a final FTIR image, with a pixel dimension of 2.6×2.6 μm, thus at ∼λ/2 for the mid-IR spectral interval. All infrared images were obtained in transmission mode from the tumor sections in the 4,000–900 cm^{-1} range by using 500 scans with spectral resolution of 4 cm^{-1}. Once the visible image was obtained, the tissue area was selected to cover one glomerulus. Typically, the FTIR images were obtained for 2x2 FPA scanning, thus covering a 171x170 μm tissue area. All data acquisition, post-processing (atmospheric CO_2 and baseline corrections), and image constructions were performed using rubber band corrections with the 64-points method, by sub-routines of the Opus 7.5 software (Bruker-Optics, France).

Spectral interval absorptions

Before calculating the spectral absorption parameters, firstly the average spectrum was taken from the FTIR image of each obstructed renal tissue. The averaged spectrum of each diseased group was found to be almost identical in terms of absorbance values (comparable intensity scale between spectra). After baseline correction had been applied on each FTIR image spectra, classification of FTIR spectra of renal tissue was performed by using the absorption intensity ratio between the spectral interval of fatty acyl chains (3050-2800 cm^{-1}) and the Amide I spectral region (1700-1600 cm^{-1})of proteins, respectively. The lipid-to-protein ratio based on intensity integration of these spectral regions is used to differentiate the biochemical changes of renal tissue from healthy to diseased animals. Then, the average spectrum of 4096 pixels per FPA from each central section of glomerular tissue block was used for further statistical analysis. Thus, the spectral alterations between the experimental conditions reflect pathological alterations rather than experimental uncertainties. This single 2D FTIR analysis is also performed in the advanced spectral curve fitting process.

For specifying the morphological change of glomerulus within renal tissue, the spectral absorption of imaging agent $BaSO_4$ is used as an indicative marker of glomerulus structure, and is verified by its intensity domination in the spectral interval of 1220-995 cm^{-1}, which is composed of four main bands discussed in our previous result [120]. Before investigating the anatomical information of glomerulus, the dominating contribution of $BaSO_4$ is determined by the absorption intensity of the integrated area attributed to four spectral intervals. The last main band (1220-1160 cm^{-1}) of $BaSO_4$ is found to show the highest absorption intensity compared to the other spectral intervals. Thus, we decided to choose this spectral interval as an index to verify the glomerular structure. For evaluating the 3D interior anatomy of the glomerulus, the integrated absorption of 1220-1160 cm^{-1} for $BaSO_4$ is also used to quantitatively measure the pathological change caused by the UUO with the benefit of visualization information.

Statistical analyses on spectra

Hyperspectral data analysis is often viewed as a statistical pattern recognition problem in a three dimensional hyperspace, often envisaged as a hyperspectral data cube. These methods usually begin with a statistical approach to find image ‘end members’. Statistical methods range from simple hierarchical cluster analysis, to complex methods such as minimum noise transforms and the RSI ‘hourglass’ method. In contrast to these statistical methods, a more traditional spectroscopic approach can be taken, where the analyst concentrates on recognizing absorption band shapes in each individual spectrum. This has the advantage of a direct connection between the transmittance spectrum of the target pixel and its chemical composition. When the hyperspectral dataset is viewed in this way, classifications are made according to underlying physical properties, rather than simply on their similarity to other pixels in the dataset. We decided to test both of approaches, classifying spectra for recognizing families of entities having large similarities,

but also by developing a curve-fitting method allowing to extract individual bands that could be assigned to known chemical entities.

Classical cluster analysis

The spectral clustering method we used is a multivariate algorithm, which aims to categorize spectra data into separate groups according to their characteristics (here the variables are spectral intensities, used either at the single wavelength level, the spectral region level or through a combination of either). Clustering is performed such that the spectra which are held within a cluster are as similar as possible (homogeneous in spectra data profile) while other spectra placed in different clusters are as dissimilar as possible. Therefore, different chemical characteristics found within biological tissues can be separated and characterized. In present studies, cluster analysis was performed in the range of 3050–2800 cm^{-1} with the use of 2^{nd} derivatives (calculated with the Savitzky–Golay algorithm and a 9-points smoothing level). The number of classes range at least from 3 to 12 clusters to verify the appropriate classifying number. After the clustering classification, generated clustering images are taken to match with the bright-field image to verify the distribution pattern of cluster groups, in order to determine a group which has as much as similarity of the glomerulus.

Curve fitting

The chemical components of biosamples examined by FTIR imaging were studied by a curve fitting procedure that individualize bands constitutive of a broader spectral interval. The method we used includes the ability to detect small relative shifts in absorption band central wavelength, the ability to separate overlapping absorption bands in a stable manner, and relatively low sensitivity to noise [121]. The reader is invited to confer to the reference mentioned here for a detailed curve-fitting procedure. I used this curve-fitting procedure for the extracting absorption band in the 3050-2800 cm^{-1} spectral interval, although I did not participate to the development of this method per se. Here, the ν=(-CH)/$\nu_{as}(CH_3)$ and the ν=(-CH)/$\nu_{as}(CH_2)$ ratio can be used as indicative indexes of fatty acyl chain unsaturation in lipid contents of tissues, which is directly linked to oxidative stress. The unsaturated/saturated ratio was calculated by taking the ratio of the area of the C=CH olefinic band (3012 cm^{-1}) to that of the C–H_2 stretching band (2928 cm^{-1}) or to that of the C-H_3 stretching band (2975 cm^{-1}) specifically recognized and extracted by the curve fitting process on all spectra of 2D images.

3D FTIR image reconstructions

After the data treatment of three kinds of analysis methods mentioned above on the raw FTIR image data, the generated FTIR spectral image with its characteristic spectral information is used in 3D stacking procedures for plotting 3D visualization. Before performing 3D stacking work, an alignment work is carried out to precisely position the two adjacent images of consecutive FTIR image data in their X, Y and tilt positions. However, realignment procedures can sometimes be impossible due to tissue deformation (at the sample sectioning step, where tissue deposition on substrate can lead to irreversible tissue shape modifications). It has made the number of finalized results in this PhD work quite limited, and thus did not allow for large statistical studies on a cohort of samples. To align the adjacent FTIR images of consecutive tissue sections, feature tracking based on the morphological detail in every tissue section is performed to complete the 3D alignment work. Because of the tissue deformation generated during the sample preparation, the morphological features within the tissue used for the alignment lies on the similarity shared between two adjacent sections. The final step of stacking 3D FTIR imaging is to merge all aligned 2D FTIR images with corrected voxel size in the X, Y and Z axis. A 3D video was finally obtained by producing a sequence of 3D stacked images, aligned properly with the use of Amira software. The rotating axis of a video, either with one of the three axes or in the coordinates of any position, is dependent on the best view of the point of interest within the reconstructed objective. The aligned frame of 2D images is rendered to a 10-second movie composed of 250 frames at the final phase of generating the 3D movie.

For verifying functional change of the glomerulus in a kidney, we use barium sulfate intensity in the spectral interval of 1160-1220 cm^{-1} to mark the vessel position pixel by pixel for generating a full view of the glomerular ball. The position parameters based on barium sulfate absorption is used, in order to load into the alignment process on the 3D image stacking of cluster analysis. Thus, a functional change and the chemical characteristics of a glomerulus is examined with 3D information. Moreover, the information of 3D FTIR imaging is completed by merging two datasets of 3D stacking images, using the information generated from a set of raw image data.

Results

In this PhD work, we proposed a spectral image based approach for analyzing biochemical issues, specifically the change of the glomerulus level of a kidney with CKD by multivariate analysis. Functional studies with 3D volumetric imaging on biosamples should be conducted into the pathological aspects of a disease study, after X-ray based imaging techniques provide remarkably clear and informative images in anatomy of the biosamples. To allow for quantitative and visual advantages on biological studies, an imaging agent based on nano-size gold particles was developed with multi-optical characteristics for X-ray, luminescence and possible IR imaging. Its chemical characteristics of biocompatibility, and its large internalization by tissue cells are suitable for its use of multimodal bioimaging. In the core study of this thesis, the 3D glomerular microvasculature is examined by using barium sulfate microparticles injected into blood vessels to reveal the morphology of the vasculature network of individual glomeruli within the kidney, which have different levels in severity of CKD (day 4 to day 14). The statistical results gleaned from the successive sections of a glomerular tissue block showed the lipid peroxidation and the ratio variation of lipid and protein molecules which exist between healthy and pathological kidneys, all completed by FTIR spectral imaging. With the chemical characterization based on the spectral data by 3D FTIR imaging, the grade of CKD in the small animal model can be determined based on the molecular components of the glomerulus unit within the kidney.

Publication No. 1:

Title: the future of infrared spectroscopy in biosciences: in vitro, time-resolved, and 3D

In this paper, we propose the new potential developments of IR imaging technique, including: 1. the analysis requirements of IR bioimaging for its current performance and; 2. the improvements of 2D IR imaging to 3D IR volumetric visualization; 3. to push its application to real-time cellular measurements. FTIR spectroscopy has been used as an analytical tool, used to study the chemical information of examined samples for decades. The development of microscopy, which can be equipped with IR spectroscopy and the utilization of an array-based IR detectors, help IR imaging in becoming an imaging technique that is a convenient tool for histological studies. The advances of FTIR imaging are majorly attributed to its simpler sample preparation, faster measurement of biosamples compared to other imaging technique, and highly feasible access to quantitative analysis due to spectral metrics of IR data, acquired through IR instruments. However, IR imaging techniques have limitations on lower spatial/lateral resolutions of image data, lower sensitivity for tracking the element/molecules within biosamples, and temporal resolution so it cannot compete with other imaging technique in the analysis of biochemical change on biosamples, nor the structure information of small molecules. Other challenges for FTIR imaging in biosciences include the long-term demand for different levels of biological compositions, from sub-molecules, cells, tissue… to satisfy the multimodal requirement by researchers. Such cellular experiments in IR imaging have been performed with the data acquisition of ATR to obtain even real time record of the cells. As of recently, the development of IR instruments with improved physical properties on optical devices has been proposed, to allow for better performance in IR data collection and data quality. This will contribute to the accomplishments of 3D measurement in an efficient way.

In biological studies, the application of FTIR imaging has been maintained in 2D scale measurement for a long time because demanding high throughput of data metrics in 3D has to face many passes to reach feasible and reliable accomplishments in biosciences. The utilization of a high-energy light source, such as a laser source, was considered as one of the reliable choices for increasing the strength of IR imaging technique on bioscience by overcoming the diffraction limit of Glowbar IR light, as well as shortening the time requirement for 3D bulk data acquisition. Thanks to the high-energy source used in IR modality which upgraded its capability to obtain data measurement with improved quality, its applications in measuring cellular level or 3D tissue blocks by IR spectroscopy becomes more practical, because of better S/N quality, enhanced sensitivity for the sub-cellular molecules and rare elements as well as more reliable spectral data of successive tissue specimens. For live IR imaging, cellular samples requires stricter experiment setup to maintain its conditions as same as its culturing state.

Vol. **129** (2016) *ACTA PHYSICA POLONICA A*
No. 1

Proceedings of the L Zakopane School of Physics, Zakopane 2015

The Future of Infrared Spectroscopy in Biosciences: in vitro, Time-Resolved, and 3D

Hsiang-Hsin Chen[a], Vladimir Bobroff[a], Maylis Delugin[a], Raphael Pineau[a], Razia Noreen[b], Yao Seydou[c], Satarupa Banerjee[4], Jyotirmoy Chatterjee[d], Sophie Javerzat[a] AND Cyril Petibois[a*]

[a] Université de Bordeaux; Inserm U1029 LAMC, Allée Geoffroy Saint-Hillaire, Bat B2, 33600 Pessac, France.
[b] Department of Applied Chemistry and Biochemistry, Govt.College, University, Faisalabad, Pakistan
[c] Centre for NanoHealth, Institute of Life Science 2 Building, Swansea University, Singleton Park, Swansea, Abertawe, SA2 8PP, UK
[d] School of Medical Science and Technology,Indian Institute of Technology, Kharagpur-721302,

Infrared (IR) spectroscopy is at the cross-roads, with the requirement to compete with cutting-edge technologies in biosciences, mostly based on analytical performances dealing with the super-resolutions: time, lateral/spatial, and contrast. IR microscopy is diffraction limited in most cases, thus not accessing to high lateral/spatial resolutions. Additionally, it has a poor signal-to-noise ratio on a single scan, thus requiring long-lasting acquisitions that are not suitable to analyze ns-lasting biochemical events. However, it is unique because it provides a broad global chemical information of the sample contents. It is also unique because it does not require heavy sample preparation nor labeling and can be coupled to other techniques (multimodality). Finally, it is again unique because it provides quantitative measurements, thus suitable for 1D to 4D data exploitation procedures. This short review shows that IR spectroscopy will be certainly subjected to a second century of innovations, maintaining its influence in the panorama of cutting-edge analytical techniques.

1. Introduction

FTIR spectroscopy has been developed more than a century ago for analytical chemistry purposes, in 1893 in its principle by Nichols [122] and popularized a bit later by William Coblentz [123]. The purpose was to develop the first spectra database of molecules and to release tables of wavelengths at which various materials absorb IR light. For almost half a century [124], FTIR spectroscopy has remained a unique analytical resource to probe the structure of small molecules, but its influence in chemistry has been minored by the development of other techniques, notably Nuclear Magnetic Resonance (NMR) and crystallography. After a century of instrumentation development, the main use of this technique has moved from molecular analyses towards the understanding of complex biological systems [125]. In the 90's, FTIR spectroscopy instrumentation focused on other applications with the release of spectrometers able to collect spectra on sample holders dedicated to quantitative, thus reproducible and comparable, measurements. The study of biofluids [126-128] has first shown that triplicate ––––––––––

* corresponding author ; e-mail: cyril.petibois@u-bordeaux.fr

measurements

allowed to obtain high reproducibility in spectra acquisitions with no more than 1% of change in absorptions on average[129, 130]. Another major advance in FTIR instrumentation for biological applications has been the development of the microscopes, as while their principle was established as early as 1949 [131], their ability to be used with both visible and IR modes [11] was found useful for bioscience. FTIR imaging systems have the advantage of a quite fast spectra acquisition since the microscope is coupled to an array of IR detectors, which may be linear (16 or 32 detectors) or focal plane (64*64 or128*128 detectors) [96]. At this state of technological development, FTIR imaging was considered as cutting–edge technology for biosciences since the reduction of time for spectra acquisitions [132] allowed applications to large tissue areas and thus opened IR to the medical field [114]. The use of high-intensity (or high-photon flux) sources could be also considered as a major advantage to obtain high S/R levels with shorter acquisition durations [133-136]. Cell imaging applications were also demonstrated taking into account a few analytical requirements to fit analytical standards in biology [133, 135, 137-139]. However, in the current competition for proposing high-performance analytical means for biosciences, it seems that FTIR instrumentations suffer from a major lack of R&D efforts, and traditional manufacturers have not released major innovations for almost 20 years. It results that the most obvious advantages of FTIR spectroscopy and microscopy for biosciences – a global chemical characterization of unaltered samples without labeling – are now completely outreached by many other techniques, notably those based on shorter wavelengths (UV to X-Ray range). In this context, several key challenges must be considered by the IR spectroscopy community to open new avenues for IR applications in biosciences. This review tackles the main R&D efforts to consent for achieving this objective.

2. Analytical requirements for bioimaging by IR spectroscopy

Molecular bio-imaging has imposed a new way to analyze cells and tissues (figure 1). From vibrational spectroscopies (mainly infrared, and Raman) to particle-based techniques (using energy of X-rays, -rays…), a wide range of microscopy techniques now fit some of the analytical features required for biological investigations [140]. The first feature is about the spatial resolution, which is determined by the physical principle of the technique[141]. In the electromagnetic spectrum, the wave-matter interactions can be exploited to reveal biosample features within the nm to cm range. The nm dimension refers to molecules, the fundamental bricks of living systems, and the cm range refers to the functional units (tissue structures) of these ones (figure 1). Because they are complex and structured systems, cells and tissues require to obtain data only at the micrometric scale or better for morphological analysis (anatomic imaging, from cytoskeleton in cells to multicellular assemblies in tissues). Major techniques exist for sub-micron analysis of cells and their sub-compartments [138]. The place of IR microscopy is interesting in this panorama of analytical techniques as it allows analyzing some of the most fundamental structures of biological specimens, i.e. at micron-scale dimensions, thus at the sub-cellular, cell, and sub-tissue levels. This is a range of dimensions that is currently poorly covered by existing microscopy techniques, which are either resolving super-resolution features on small volumes (or limited field-of-view), or do not provide sufficient lateral/spatial resolutions on larger specimens (mm^3 or bigger). IR microscopy has the advantage of a quite low diffraction limit (typically

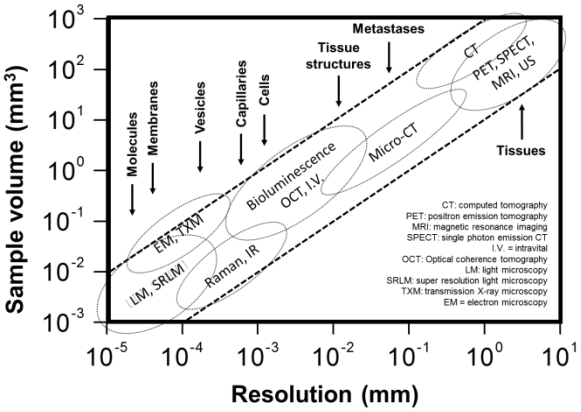

Figure 1: Analytical techniques allowing a microscopic analysis of biosamples, from nanometer to millimeter dimensions and for different biological targets.

~3-20 µm for the 4000-500 cm^{-1} mid-IR interval), but also a weak penetration depth (5-30 µm for soft materials like tissues), thus limiting its applications in biosciences.

Another feature to consider in biological imaging is the temporal resolution, which will determine the applications of techniques for time-resolved analyses. This temporal resolution for biological applications is also related to sample stability during data acquisitions [142]. The physical properties of imaging modalities will determine their applicability on time-resolved analyses in biology. Most of imaging modalities using accelerator-based sources are not designed for analyzing living specimens due to the utilization of high energy beams. However, molecular dynamics may be determined out of the living environment, such as for the analysis of proteins folding or conformation under stress conditions (pH, temperature, etc.), where high energy may be required for time-resolved data acquisitions within the ms-ns range of time [143].

The third main feature to consider for determining the applicability of imaging modalities to the biological field is the sensitivity. In this domain, it is clear that accelerator-based sources play their most significant role for enhancing analytical performances, namely by increasing the S/N level. This allows one to perform data acquisitions closer to the diffraction limit or to reduce the time of acquisition for obtaining information on kinetics of biological samples, the so-called time-resolved experiments. In this sense, IR microscopy has not been considered as a valuable technique for biological dynamics. The major developments of IR instrumentation to biological applications so far have been focused on sub-diffraction live cell imaging [134, 136, 139] and high-throughput 2D tissue analyses [96, 112, 137, 140]. Therefore, in the battle for achieving the best compromise between sensitivity, resolution, and time of acquisition, IR microscopy remains limited by the low-photon flux of its conventional IR sources (Glowbar) and the diffraction limit.

3. From FTIR to IR spectroscopy and microscopy… the road to 3D

In principle, FTIR microscopy is too slow in spectra acquisitions and provides too weak S/N levels to allow comparison between large spectra data sets, i.e. millions to billions of spectra. The S/N being dependent on environmental factors as well as electrical noise from the analytical instrumentation, there is little chance to obtain highly reproducible spectra for long-lasting acquisitions. This limit is affecting biological applications in the sense that quantitative changes in many chemical contents distribution (in cells or tissues) will remain very limited for physiological reasons. The example of glucose concentration in a normal physiological condition is a good demonstrator of what the biological variability is: blood concentration is normally ranging between 0.8 and 1.3 g/L and remain very close to 1 g/L in most of the cellular and extracellular compartments. Therefore, one may not expect major changes in glucose concentration distribution in tissues, and analyzing this molecular parameter at the microscopic spatial resolution will require accurate quantitative method with low margin of error in measurements, at least not superior to 2-5 % of average value. FTIR spectroscopy and microscopy have not demonstrated that level of accuracy on triplicate measurements in biofluids [129, 130], and thus one may not expect obtaining such analytical performance on successive tissue sections analysis. This slow acquisition issue must be overcome to expect developing FTIR microscopy for 3D applications. Although IR microscopy is not suitable for direct tomographic measurements on biosamples – because: 1- IR photons have limited depth of penetration in matter [96, 133], 2- biosamples contain >60% of water with unmanageable absorptions [139], and 3- transmission measurements do not allow resolving absorptions in a true confocal geometry [136] – its quantitative nature should allow the reconstruction of a 3D matrix of spectra.

The recent release of microscopes powered by IR-laser sources is allowing new approaches for biological applications, with the opportunity to obtain high S/N spectra in short time, probably 2 or 3 orders of magnitude faster than with the Glowbar sources. The wavelength-by-wavelength signal acquisition do not require the use of the Fourier transformation for spectra reconstruction

(thus reducing mathematical approximations in absorption calculations), and provides absolute count of photons on detector, thus ensuring more accurate quantitative analysis of biosamples. These microscopes are not yet exempt from limits. They use several quantum-cascade lasers to cover a large spectral region (1700-900 cm^{-1} is currently proposed), which poses the question of the signal intensity reliability and continuity between lasers. This is a fundamental question to consider quantitative analyses of chemical contents in 3D tissue blocks. Anyway, with a fast and high S/N level spectra acquisitions, IR microscopy should allow reconstructing a large 3D matrix of IR spectra for tissue analyses (see proposed method in figure 2). The main purpose might be to introduce a new concept of spectral data treatments and exploitation, named 'spectromics' [144], which is essentially the use of any spectral information (or combination or calculation of data extracted from spectra) that allows discrimination of two objects (ex. healthy vs. pathological tissue or sub-structures inside the same tissue volume). Different spectral data treatment methods have been developed so far to extract an individual (ex. an IR band) or a well-identified (ex. amide I region) chemical information from spectra.

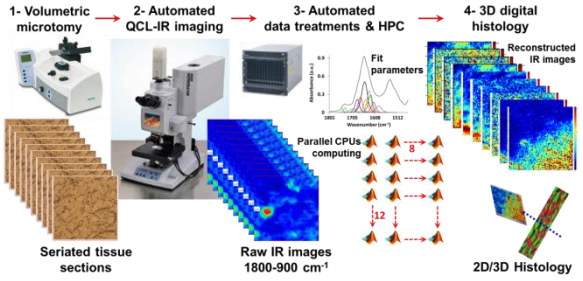

Figure 2: Developing 3D IR microscopy for tissue block analysis. The concept of 3D digital histology can be developed by IR microscopy due to its intrinsic advantages, i.e., a global chemical analysis of biosample contents, a quantitative access to these ones, and a suitable sampling methodology for unlimited chemical data treatments of raw matter. The proposed methodology includes an automated tissue sectioning for obtaining reliable 2D images (visible and IR) that can be further stacked for 3D block reconstruction. Spectral data treatments are further performed for reconstructing 3D chemical information distribution with quantitative value in the tissue.

The 3D reconstruction of these data might provide unique information about a tissue, with 3D resolved sub-structures correlated to biochemical or metabolic events. This would lead to the combination of morphological and molecular data into the same 3D image of a biosample, thus comparable to the MRI/CT or PET/CT multimodal imaging methods, but with three major advantages: 1- a single technique would be used (thus using a single dataset of IR data), 2- 3D reconstruction will be performed at the microscopic scale (down to /2, i.e., a 3-µm spatial resolution is achievable), and 3- without the use of any label or imaging contrast agent, thus avoiding sample manipulations and alterations.

4. From dry to wet biosampling in IR microscopy, and down to nanoscopy

Recently, it has been proposed to use the attenuated total reflectance (ATR) acquisition method to obtain live cell images without constrain of the diffraction limit [139]. With synchrotron radiation source, this imaging can be performed in short time, i.e., in less than one minute, thus allowing to characterize macromolecular sub-cellular contents change

[134]. Again, benefiting from the above mentioned innovations for high-speed and quantitative analyses, IR microscopy might become the first analytical technique able to determine metabolic and biochemical change in cells *in vitro*, thus opening the way to pharmacological experimentations on dose-response effects of drugs at the single cell level [138, 145]. In fact, live cell imaging might concentrate all the benefits from technological innovations found in the new line of IR microscopes, with time-resolved, highly

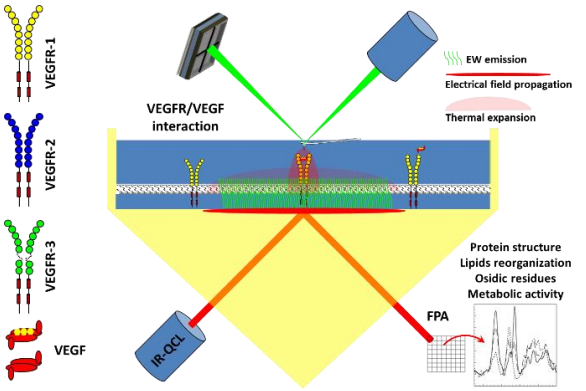

Figure 3: Principle of time-resolved *in vitro* IR spectroscopy, with high-speed and nanometric analyses. Nano-IR analyses are feasible with 3D rendering from AFM measurements. The example here shows a sketch for protein-receptor (VEGF/VEGFR) interaction analysis by both non-contact liquid AFM and ATR-IR microscopies in a coordinated mode. A ms-range spectral acquisition is possible with analysis of conformational change of protein-receptor interaction by IR spectroscopy using the amide I&II spectral interval (1700-1500 cm^{-1}) and with polarized beam for magnifying the amideI/amideII absorption changes.

sensitive and quantitative measurement below the diffraction limit (down to λ/400 as IR-laser sources are coherent, thus not limited by diffraction, which is reinforced by the use of ATR

devices that are collecting the evanescent wave on surface of the reflecting substrate),all features collectively inaccessible for any other microscopy technique, except maybe for Raman, but this one will be less sensitive and more resolutive than the IR microscopy. This might open again the debate between these two vibrational spectroscopy techniques for high-end microscopy applications in biosciences, to the delight of spectroscopists!

The *in vitro* applications with ATR devices have been also developed for the measurement of nano-scaled biosamples [146], namely proteins or sub-cellular species, such as chromosomes of polymerized biomolecules [147]. The coupling to an atomic-force microscope (AFM) is fundamental as it allows a 3D rendering that can be coupled to the co-localized acquisition of IR spectra, thus providing a volumetric and quantitative analysis of nano-sized biosamples (figure 3); down to pixels of ten nm only [148]. This innovation should allow the development of fundamental experiments that are currently not possible with X-Ray free electron lasers (X-FEL) or other super-resolution analytical techniques, namely the real-time nanoscopy in structural biology [149]. The example shown in figure 3 is showing possible application for *in vitro* analysis of membrane protein (a receptor) interaction with a ligand (here a growth factor), which can be performed with biochemical/metabolic cascade of

event if a microfluidic device is developed for that purpose.

5. Conclusion

IR spectroscopy offers significant analytical advantages over most of the other techniques in the field with a quantitative and global chemical rendering of a biosample. The recent methodological efforts allowing to perform *in vitro* analyses for single cell imaging and data treatments methods for extracting given chemical data from spectra, among other examples, show the relevance of the development of a new line of microscopes, much faster, sensitive and resolutive than the first generation. Laser-powered IR microscopes are arriving and promise analytical performances that should facilitate the development of time-resolved (in the ms range) and 3D (for tissues) applications with incomparable outputs. The strength of IR-lasers is also making that nano-resolved species can be analyzed at $\lambda/400$, thus approaching the single molecule level with quantitative and volumetric rendering thanks to the coupling of an AFM. This should reintroduce the IR microscopy and nanoscopy into the panel of cutting-edge technologies for enhancing our knowledge on biosamples, from single molecule, to single cell and to tissues (even organs in small animal models), as well as in routine analyses for biomedical and biological research purposes.

References

[1] E.F. Nichols, *Physical Rev*, **1** 1 (1893).

[2] W.W. Coblentz, Investigations of Infrared Spectra, in: T.P.P.N.M. USA (Ed.) Carnegie Institute of Washington, Washington D.C., 1905, pp. 1.

[3] E.J. Ambrose, A. Elliott, *Proceedings of the Royal Society of London*, **260** 206 (1951).

[4] D. Naumann, D. Helm, H. Labischinski, *Nature*, **351** 81 (1991).

[5] C. Petibois, V. Rigalleau, A.M. Melin, A. Perromat, G. Cazorla, H. Gin, G. Deleris, *Clin Chem*, **45** 1530 (1999).

[6] G. Budinova, J. Salva, K. Volka, *Appl Spectrosc*, **51** 631 (1997).

[7] K.J. Ward, D.M. Haaland, M.R. Robinson, R.P. Eaton, *SPIE: Fourier Transform Spectroscopy*, **1145** 607 (1989).

[8] C. Petibois, G. Cazorla, A. Cassaigne, G. Deleris, *Clin Chem*, **47** 730 (2001).

[9] C. Petibois, G. Cazorla, H. Gin, G. Deleris, *J Lab Clin Med*, **137** 184 (2001).

[10] R. Barer, A.R.H. Cole, H.W. Thompson, *Nature*, **163** 198 (1949).

[11] C. Petibois, G. Déléris, *Trends Biotechnol*, **24** 455 (2006).

[12] P. Innocenzi, T. Kidchob, J.M. Bertolo, M. Piccinini, M.C. Guidi, C. Marcelli, *J Phys Chem B Condens Matter Mater Surf Interfaces Biophys*, **110** 10837 (2006).

[13] D.C. Fernandez, R. Bhargava, S.M. Hewitt, I.W. Levin, *Nat Biotechnol*, **23** 469 (2005).

[14] C. Petibois, M. Cestelli Guidi, *Anal Bioanal Chem*, **391** 1599 (2008).

[15] C. Petibois, G. Deleris, M. Piccinini, M. Cestelli Guidi, A. Marcelli, *Nat Photonics*, **3** 179 (2009).

[16] C. Petibois, M. Cestelli Guidi, M. Piccinini, M. Moenner, A. Marcelli, *Anal Bioanal Chem*, **397** 2123 (2010).

[17] C. Petibois, M. Piccinini, M. Cestelli-Guidi, A. Marcelli, *J Synhrotron Rad*, **17** 1 (2010).
[18] B. Drogat, M. Bouchecareilh, C. Petibois, G. Déléris, E. Chevet, A. Bikfalvi, M. Moenner, *J Cell Physiol*, **212** 463 (2007).
[19] C. Petibois, *Anal Bioanal Chem*, **397** 2051 (2010).
[20] M. Cestelli Guidi, S. Yao, D. Sali, S. Castano, A. Marcelli, C. Petibois, *Biotechnol Adv*, **31** 402 (2013).
[21] C. Petibois, K. Gionnet, M. Goncalves, A. Perromat, M. Moenner, G. Déléris, *Analyst*, **131** 640 (2006).
[22] E. Levenson, P. Lerch, M.C. Martin, *Infrared Phys Technol*, **51** 413 (2008).
[23] H. Fabian, P. Lasch, D. Naumann, *J Biomed Opt*, **10** 031103 (2005).
[24] M. Cestelli-Guidi, M. Piccinini, A. Marcelli, A. Nucara, P. Calvani, E. Burattini, *J Opt Soc Am A*, **22** 2810 (2005).
[25] C. Petibois, B. Desbat, *Trends Biotechnol*, **28** 495 (2010).
[26] C. Petibois, E. Goormaghtigh, A. Travo, V. Bobroff, Method for determining absorption bands, in: Inserm (Ed.), France, 2014.
[27] C. Petibois, *Anal Bioanal Chem*, **397** 2031 (2010).
[28] C. Mayet, A. Deniset-Besseau, R. Prazeres, J.M. Ortega, A. Dazzi, *Biotechnol Adv*, **31** 369 (2013).
[29] S. Ghosh, N.A. Kouame, L. Ramos, S. Remita, A. Dazzi, A. Deniset-Besseau, P. Beaunier, F. Goubard, P.H. Aubert, H. Remita, *Nat Mater*, **14** 505 (2015).
[30] J. Houel, E. Homeyer, S. Sauvage, P. Boucaud, A. Dazzi, R. Prazeres, J.M. Ortega, *Optics express*, **17** 10887 (2009).
[31] C. Petibois, *Anal Bioanal Chem*, **399** (2011).

Publication No. 2 (Project): Applying 3D FTIR imaging to CKD investigation

This paper represents the core study of the PhD work, with the development of a methodology for characterizing biochemical and functional changes in glomeruli in the development of the CKD pathology within small animal models. The animal models were prepared at TSGH in Taipei (supervision: Prof. Ann Chen and Dr. Shuk-Man Ka), the analyses by X-Ray tomography were performed by the Nano-X laboratory in Taipei (supervision: Prof. Yeukuang Hwu), and the analyses by FTIR imaging were performed at the Inserm U1029 LAMC laboratory in Bordeaux (supervision: Dr. Cyril Petibois). The aim of this international integrated project is to explore a new methodology involving 3D multimodal imaging techniques for diagnosis analysis; specifically, progressive renal disease. The merging of X-ray/IR imaging techniques to investigate the pathological features of CKD has the advantages of characterizing 3D anatomical information of the kidney, and allowing for global examination of biochemical contents of the renal tissue blocks. This is a systematic approach of combining morphology and function study to study a disease progress at the organ level.

The deficiency of the glomerulus level in the kidney is a heterogeneously progress of losing renal function, and the level of filtering efficiency in individual glomerulus units vary region by region in a kidney organ. The changes and occurrences of renal pathological causes on the obstructed kidney make the diagnosis and prognoses of obstruction induced CKD (UUO animal model) inaccurate, and thus faces the difficultly of tracing disease development. We propose to use the FTIR imaging strategy to examine the functional change of the glomerulus level in CKD by performing 3D reconstructed tomography of glomeruli. Several parameters of molecular contents of tissue blocks analyzed by multivariate data treatment reveal the key information of stressed glomeruli regarding of the microstructure, oxidative stress and the content balance of lipid to protein ratio. We aim to reconstruct a 3D FTIR image based on bulk spectral data, to visualize the spatial distribution of a variety of sub-

molecules of glomerulus and its microenvironment, to further examine pathological changes of the CKD development.

Title: 3D FTIR imaging of the kidney glomeruli' micro-environment in chronic kidney disease

Hsiang-Hsin Chen[1], Vladmir Bobroff[1], Adrian Travo[1], Maylis Delugin[1], Ann Chen[2], Shuk-Man Ka[2], Bai-Hung Kao[3], Yeukuang Hwu[3], Cyril Petibois[1]

[1] INSERM U1029 LAMC, Université de Bordeaux, Allée Geoffroy Saint-Hillaire, Bat B2, 33600 Pessac, France.

[2] Department of Pathology, Tri-Service General Hospital, National Defense Medical Center, No. 325, Sec. 2, Cheng-Gung Road, Taipei, Taiwan.

[3] NANO-X Laboratory, Institute of Physics, Academia Sinica, No 128, Sec. 1, Academia Rd. Nankang, Taipei 115-29, Taiwan.

Abstract: A mouse model of chronic kidney disease (CKD) has been analyzed using a chemical histology technique, FTIR imaging, for a 3D reconstruction of glomeruli to determine biochemical and functional changes during the pathology development. With 3D reconstructed FTIR imaging on CKD tissue specimens, the results showed the loss of glomerular filtration rate along with an increase of lipid peroxidation related to oxidative stress, spectral characteristics on lipid molecules and changed protein-to-lipid ratio. By using $BaSO_4$ microparticles perfused into renal blood vessels, the distribution of BaSO4 revealed by the spectral integration of 1160-1220 cm^{-1} spectral interval is used as an indicative index for glomerular microvasculature with morphological abnormalities of inner glomerular capillaries. In this study, we propose a methodology based on 3D FTIR chemical imaging as a functional histology tool for determining lipid peroxidation level and blood vasculature of glomeruli supported by the statistical results of 3D spectral data.

Introduction:

60

Chronic Kidney Disease (CKD) is a health problem in the world, and has rare symptoms that are detected before the appearance of severe pathological signs with the combined complications [18]. In the U.S., there is a higher prevalence of 10.6 % in the earlier stage (stage 1, 2 and 3) of CKD than the moderate stage (stage 4, 0.2 % prevalence) or late stage (stage 5, 0.1 % prevalence) by estimating the GFR [3]. More than 11 % percentage of Americans aged over 65 year old have CKD at stage 3 [150]. The progression of CKD eventually leads to the end-stage renal failure (classified as stage 5), which causes the permanent loss of kidney function, and the patients are treated with the options of taking renal replacement treatments (either dialysis or transplantation), which increases the load on financial issues in national policy. Additionally, the death rate of the population with stage 4 of CKD is up to 45.7 %, while for the stage 2 and 3 the rate is less but still significant, with 19.5 % and 24.3 %, respectively [151]. The statistics gathered in analyzing the mortality and clinical treatment of people with CKD of mild to moderate stages indicates that death is more common than the rate of renal replacement treatment, which is less than 2 % for stage 2 and 3, respectively, and nearly 20 % for stage 4.

Many systematic disorders affect kidney function by altering the glomeruli, the functional part of renal unit nephron, which performs selective ultrafiltration for body clearance and the maintenance of systematic balance. A variety of etiological factors contribute to glomerular injury, such as genetic disorders, microenvironment stress, microorganism infections, uptake of harmful material as well as the physiological decline of activity due to aging [1, 152]. Progressive glomerular injury in CKD represents the consequences when partial glomeruli are damaged, which generally are affected by tubular atrophy due to proliferated fibrosis in the renal interstitium, and the response of compensatory hyperfiltration of glomeruli in remaining nephrons due to the loss of sufficient nephrons. Histopathological patterns of glomerular change have two categories in morphological abnormalities, with variation in glomerular size and vasculature structure, and functional disorder with impaired selectivity in filtrating materials. Both types of features on glomerular disorder is involved with extent of severity in kidney damage. Hence, to

diagnose and manage glomerular injury, referring to impaired kidney functions should incorporate the analysis in morphometric aberration and molecular dysfunction.

The current method to evaluate the level of glomerular damage depends on either the level of glomerular filtration efficiency or the appearance of proteinuria attributed to the impairment of glomerular barrier. Nephron number, and the filtration rate in each nephron determinate GFR value. Both indicators are involved with body matrices. In some glomerular disease, the diagnosis requires the renal biopsies to estimate the expression and states of biomolecules correlated with the pathological change which cannot be indicated by blood or urine. However, the lack of morphometric information remains the reason of insufficiency in the diagnosis of glomerular disease. As this regards the need for a reliable method to assess glomerular injury, it raises the priority of performing quantitative analysis that is coupled with imaging capability, to provide the support in morphometric information.

Many research results in laboratory and clinical studies have demonstrated that Fourier-transform infrared (FTIR) spectral imaging is capable of discriminating chemical changes in biological specimens [114, 142, 153]. This technique is based on the absorption of IR photons by molecular bonds, with a specific spectrum of all absorptions occurring for a given biomolecule. For a biosample, for instance a tissue, it provides a global view of all its chemical compounds [97]. It thus provides a non-supervised recognition tool of chemical changes in biosamples, and thus allows investigations of various pathological conditions where molecular parameters are modified or affected. By using an analysis by FTIR imaging, it is feasible to monitor the variation in the structure and the property of biochemical features, including nucleotides, proteins, lipids, and carbohydrates. Thanks to reagent-free methods, the advantage of an FTIR imaging for preserving biochemical contents in their native state allows for measuring quantitative and structural changes of physical and chemical characterization on pathological specimens [112]. To that end, numerous algorithms have been developed to unravel the chemical

changes found in spectra, such as spectral clustering classification, principal component analysis (PCA), partial least square (PLS) calibration, curve fitting to extract individual absorption bands from spectra…etc [154-157]. For tissue section analysis (called 2D FTIR imaging), this allows us to map chemical parameters with a quantitative value, thus making it possible to determine the distribution of concentrations [158, 159], of molecular structure changes [160, 161], and even of biochemical parameters, such as oxidative stress [162, 163]. However, the limit at using 2D FTIR imaging is that it does not provide details on spatial distribution of tissue sub-structures, such as blood and lymph vessels, cellular organization and arrangement…etc.

Recently, an approach of 3D FTIR imaging has been proposed [164] to visualize the compositional information of thick samples, to improve the expansion of spectral analysis. The procedure to perform data acquisition is currently used to collect a series of tissue sections to obtain their corresponding 2D FTIR images, before completing a 3D stacking. The development of a 3D FTIR image reconstruction methodology would change the face of chemical microscopy for a multidimensional analysis of tissue contents, combining both the anatomical and molecular parameters of tissues from the same spectral data cube. Slice to slice stacking of 2D spectral would thus offer a more practical way to acquire a global analysis of tissue contents in laboratory for biomedical research as well as for clinical applications. 3D IR reconstructed images offer analytical performances of choice to understand the development of CKD at the glomerulus level, with a microscopic approach of the tissue sub-structure (few microns), and potentially a global chemical analysis of biochemical, structural, and functional features if a methodology is developed accordingly. The functional aspect can be obtained by using an imaging contrast agent perfused in the blood system, thus allowing us to appreciate the GFR at its smallest level.

We used an animal model of mice subjected to unilateral ureteral obstruction (UUO) to study the CKD pathological development at the glomerulus level by FTIR imaging. Complete UUO initiated a sequence

of decreased renal functions in the obstructed kidney with respect of timing, severity and duration while avoiding the interference of chemical materials, genetic engineering and viral/bacterial infection [165-167]. The aim of present work is to develop a methodology of analyzing progressive renal tissue on the basis of infrared imaging with quantitative chemical information and 3D visualization capability. In our results, 2D and 3D reconstructed FTIR images provided functional and biochemical analyses from the same dataset. Spectroscopically, the change in the ratio between lipids and proteins, the increased lipid peroxidation, and filtration change in glomerular vasculature (using perfused contrast agent $BaSO_4$) on glomerular disorder is discriminated, which reveals the pathological variation of glomerular disease in the progression of CKD.

Method and materials

Animal experiment and tissue sample preparation

All animal experiments are performed in male B6/C57 male mice strain of 8 weeks, purchased from the National Laboratory Animal Center, Taipei, Taiwan. Complete UUO surgery is operated in the right kidney of each mouse after being anesthetized with a mixture of isoflurane and oxygen. The advantage of the UUO animal model used to study CKD is that the consequence of histopathological events after UUO is highly predictable and reproducible within a short-term stage (usually within two weeks). In present studies, $BaSO_4$ microparticles suspended in PBS are perfused into blood vessels of each kidney of a mice, which have been perfused with PBS for removing blood, subjected to UUO and without the operation, respectively, in 4, 9 and 14 days after UUO. After their death, the kidneys excised are immediately frozen in liquid nitrogen for later microsectioning by cryo-microtome. Serial sections are cut in 10 μm thickness under -20 C by cryostat and then placed on IR-transparent CaF_2 substrates for further FTIR chemical imaging after air-drying for a few minutes at room temperature.

FTIR data acquisition and data processing

All FTIR image data of air-dried renal specimens was recorded in the spectral interval of 900-3900 cm^{-1} in transmission model with Bruker Hyperion-3000 FTIR microspectroscopy, equipped with a 64 x 64 pixel FPA detector with a field of view of 167 x 167 μm^2. The background data is recorded in the blank area outside the tissue deposition in CaF_2 window. Each spectrum on one FPA FTIR image in 4096 pixels was obtained with 500 scans at 4 cm^{-1} resolution. All spectral processing and classification is performed using Kinetics and "Cluster Menu", written by our group members, in Toolbox of MATLAB2012. The data processing is operated on the entire spectra of imaging data sets, not truncated spectra. The subtraction of baseline correction in each spectrum uses 6 reference points at 925, 1800, 2100, 2500, 2700 and 3700 cm^{-1}.

Spectral clustering analysis

Clustering classification provides a direct identification via the reduction of complexity in sample to evaluate the biochemical feature and the content of various tissue components in specimens. The advantage of clustering characterization in spectral data is that this data treatment is performed on unsupervised data to discriminate the spectral difference of raw spectrum. The level of spectral similarity in spectral shape and magnitude shared in individual spectra of matrix is the estimating standard of assigning the spectra to its belonging cluster.

The selected spectral interval for algorithms by clustering analysis is at C-H stretching region (2800-3050 cm^{-1}) for F.A.C. absorption and at $BaSO_4$ donating region (1160-1220 cm^{-1}), respectively. Application of spectral clustering is performed on background corrected image data with normalization in Amide I region. Every spectrum plotted as a square pixel on resulting image in the FTIR map is coded as a false color square corresponding to its assigning membership of its belonging cluster.

Curve fitting

The Curve fitting algorithm provides detailed information of chemical components attributed to individual bands in FTIR spectrum. The spectral parameters including wavelength of bands, amplitude (peak height), band-width and band shapes, which possess unique features representing a discriminative vectors of biochemical variations in tissue. The performance of curve-fitting in spectra of FTIR image data is operated point to point by auto-algorithm in MATLAB software. To localize the position of subpeaks of assumptive bands, which is always fixed, it is obtained by secondary-derivative analysis to enhancing the separation of overlapping bands in spectrum. Thus, curve fitting provides the multiple compositional information of spectra on FTIR imaging.

A spectral interval of interest in 2787-3115 cm^{-1} corresponding to the CH stretching region has undergone the performance fitting treatment by using 27 component bands for the best fitting in tissue. The area of fitted bands provides the quantitative information of samples, which is more specific, to justify the concentration of constitutions than integration of border spectral interval. The band peak located at 2925 cm^{-1} and 3014 cm^{-1} stand for asymmetric CH_2 group and olefinic -C=CH group, respectively.

3D FTIR imaging construction

The 3D visualizing of glomeruli composed of a series of tissue sections is constructed by stacking adjacent 2D FTIR images after the multivariate approaches. The alignment work before each successive 2D image stacking is performed to correct the image position of each adjacent spectral data for generating an accurate distribution of biochemical content in tissue. The spectral range for the integration to present the absorbance of SO_4 group of $BaSO_4$ microparticles is set in the region of 1160-1220 cm^{-1} for the purpose of revealing the spatial distribution of the amount of perfused $BaSO_4$ microparticles correlated with the anatomic alternation of glomerular capillary. The resultant 3D volume render imaging was plotted as 256 color-coded palettes, and smoothed by using Gaussian interpolation

processing. Through representing the 3D spectral features revealed by cluster classification, each resultant 2D cluster map is assigned with a constant color that displays the geometric information, not the quantitative indication before 3D image rendering.

Result and discussion

Variation of biochemical compositions on renal specimen in UUO model

Two spectral intervals of 2800-3050 cm^{-1} and 1600-1700 cm^{-1} on FTIR image are used to calculate their integrated area for estimating the lipid and protein content, respectively, on all renal biopsies of obstructed kidneys. As shown in Figure 18, chemical imaging allows for the visualization of the distribution of lipid and protein on renal samples, respectively. Both lipid and protein content are more enriched in the glomerular area than in any other non-glomerular area of all renal samples, including the obstructed kidney and the normal kidney by representing FTIR image with false color code. Interestingly, there is obviously an increasing lipid to protein ratio on glomeruli in an obstructed kidney after 4 days of obstruction compared to a normal kidney. In the duration of extended renal obstruction, the ratio on glomeruli in an obstructed kidney then returned down to levels similar as in a normal kidney. At day 14 of UUO, it became a more homogeneous state of lipid to protein ratio on whole tissue section, which was distinguished from other obstructed renal samples and normal renal samples.

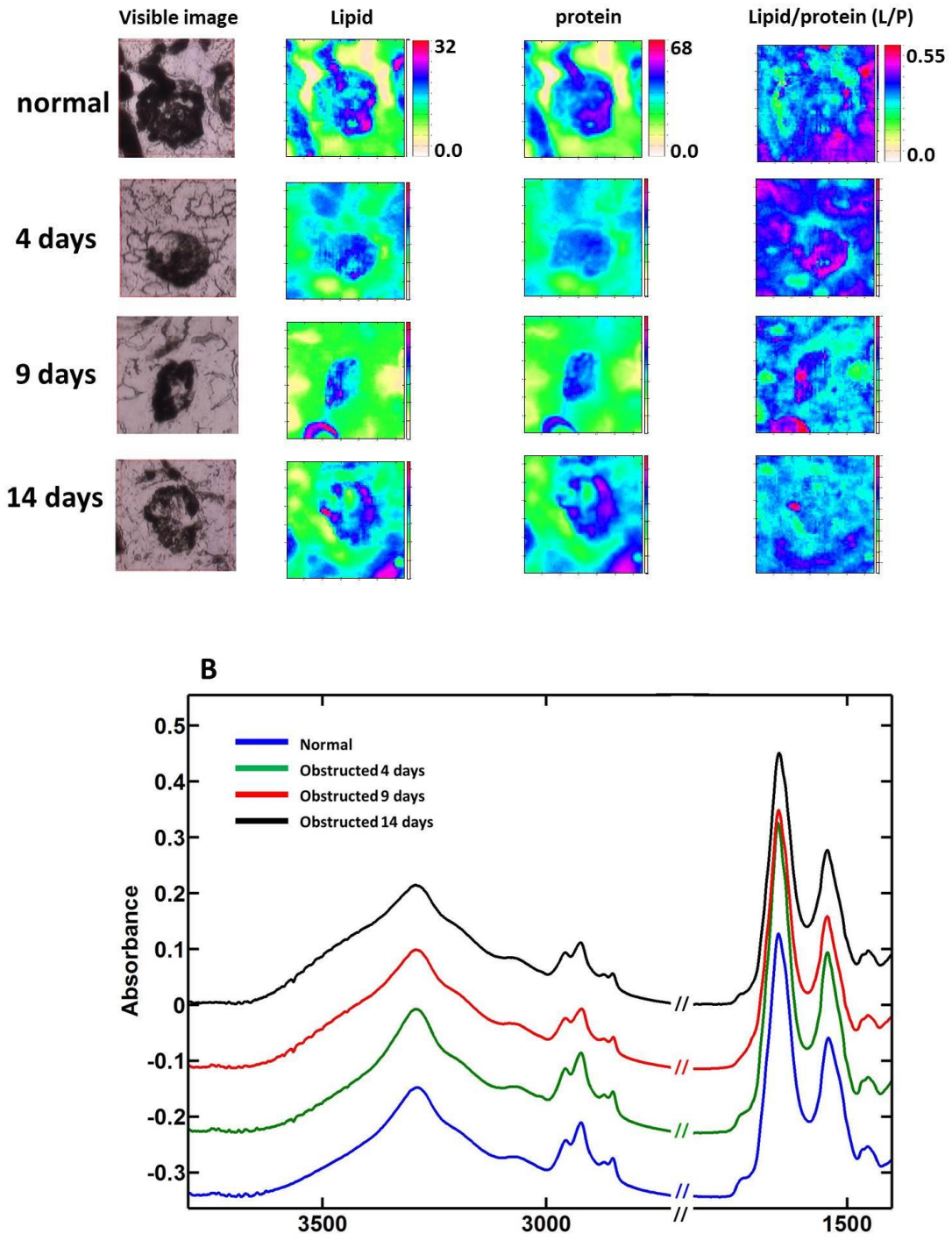

Figure 18. The variation of biochemical content in the kidney of UUO mice. (A) The FTIR spectral images display the quantitative information of lipid and proteins by integrating the spectral interval of 2800-3050 cm^{-1} and 1600-1700 cm^{-1}, respectively, in renal samples. The value representing the molecular content is the integrated area under the selected spectral interval in each spectral pixel of FPA image. (B) The

average infrared spectra of 4096 individual spectra in FPA image data. The spectral range displayed is 1400-3800 cm^{-1}.

In respect to the statistical analysis on the FTIR spectral image, the change of molecular components of a kidney with CKD was evaluated by measuring the average lipid-to-protein ratio in all renal samples. The data treatment analyzed a series of 2D spectral images, generating the successive 2D result from a cubic tissue compared with single 2D result of the central tissue section of glomeruli. Firstly, the whole renal tissue is taken for evaluating, to examine whether there is a difference in variance of biochemical components in each sample. Figure 19 shows the statistical results of the lipid to protein ratio by integrating spectral interval corresponding to total lipid and amide I, respectively, in each FTIR data of all biopsies. The result indicates that spectral analysis in molecular contents of each successive specimen is capable of discriminating the biochemical change of CKD induced by UUO in our renal study. By looking closely at the spectral variance in glomeruli in figure 19C, the result from successive 2D data shows a large increase in lipid to protein ratio on glomeruli in the 4-day obstructed kidney, compared to either the normal kidney or the contralateral kidney. The same result is demonstrated in the FTIR image data represented in false color in the last right-hand panel of figure 18. The advantage of this approach is that successive 2D FTIR data provides an insight directly estimating the change of biochemical composition, either in whole tissue or functional unit glomeruli in a geometric viewpoint during the development of renal disease.

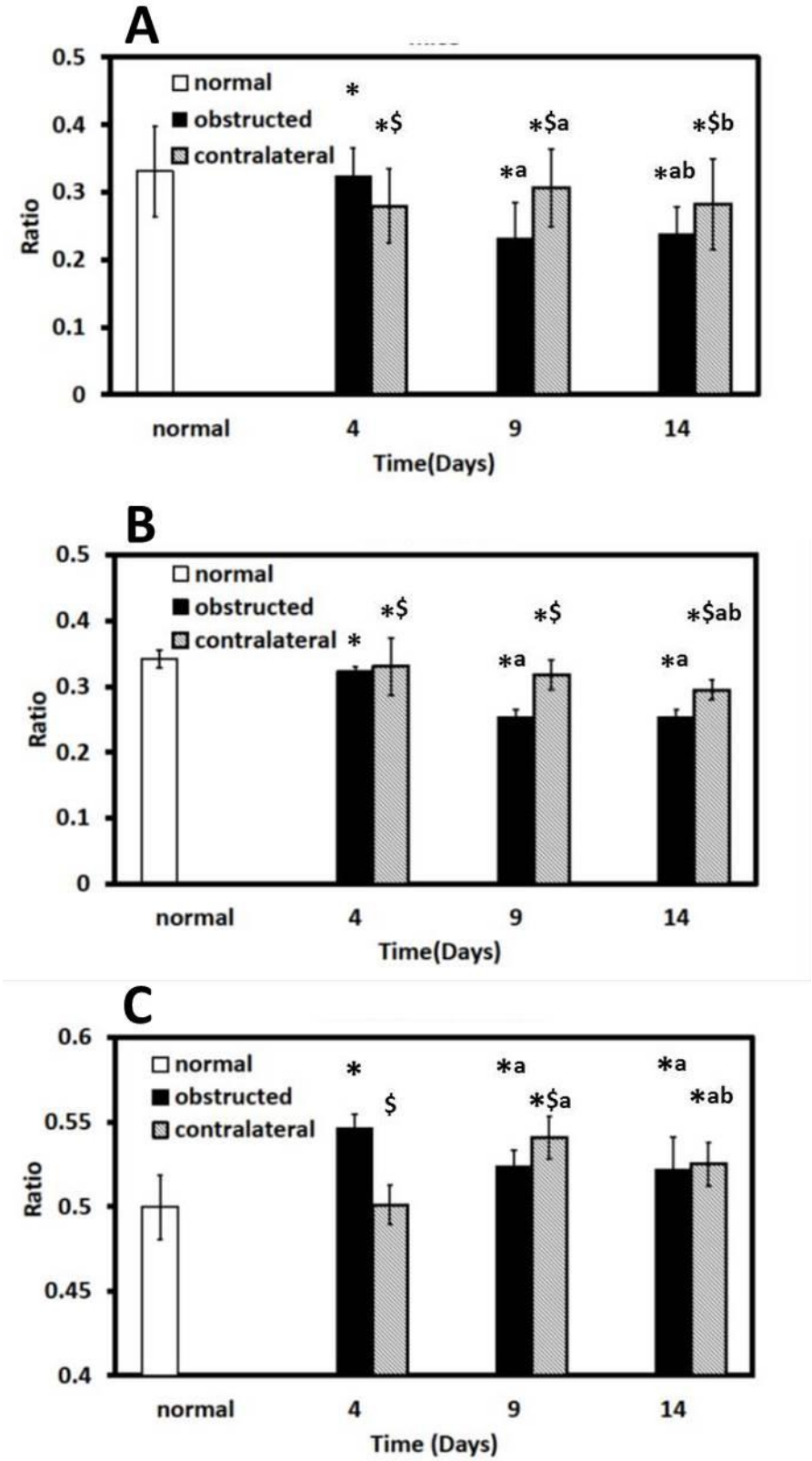

Figure 19. Statistical pattern of lipid to protein ratio in renal specimens of UUO mice. The average ratio is representative of the intensity of lipid to protein on (A) the central section of whole renal tissue (B)

successive sections of whole renal tissue (C) successive sections of glomeruli. There are 4096 spectra in each FPA of renal specimen. $P < 0.05$. ***** vs. Normal. **$** vs. Obstructed. **a** vs. 4d. **b** vs. 9d.

The same approach is performed to study the variation of chemical state within F.A.C. molecules in renal samples, by curve fitting to evaluate the intensity and characteristics of individual bands in the CH stretching region. In our study, the ratio of the intensity at 3014 cm^{-1} and 2925 cm^{-1} is computed to monitor the lipid peroxidation reflecting oxidative stress, which is reported to have significantly increased in the UUO model [168]. The result of analyzing each spectra of whole renal tissue indicates the ratio is increased in an obstructed kidney and its contralateral kidney after 4 days, compared to a normal kidney shown in Figure 20. However, in the early stage of 4 days after the obstruction, oxidative stress in the glomerular area of a contralateral kidney increases more than in obstructed kidney, which maintains similar levels as in the normal kidney.

The result of our study in the UUO model, investigated by spectroscopic imaging, shows that oxidative stress is significantly enhanced in the obstructed kidney and its contralateral kidney when regarding mice subjected to UUO treatment. Lipid peroxidation worsens in the obstructed kidney during the middle stage of UUO, and this was found by analyzing both whole renal tissue and the glomerular area of the renal specimen. For monitoring the pathological state of glomeruli, the significant point showed in the data is that more peroxidation expression was observed in the contralateral kidney, not in the obstructed kidney, of the mouse with CKD induced by UUO.

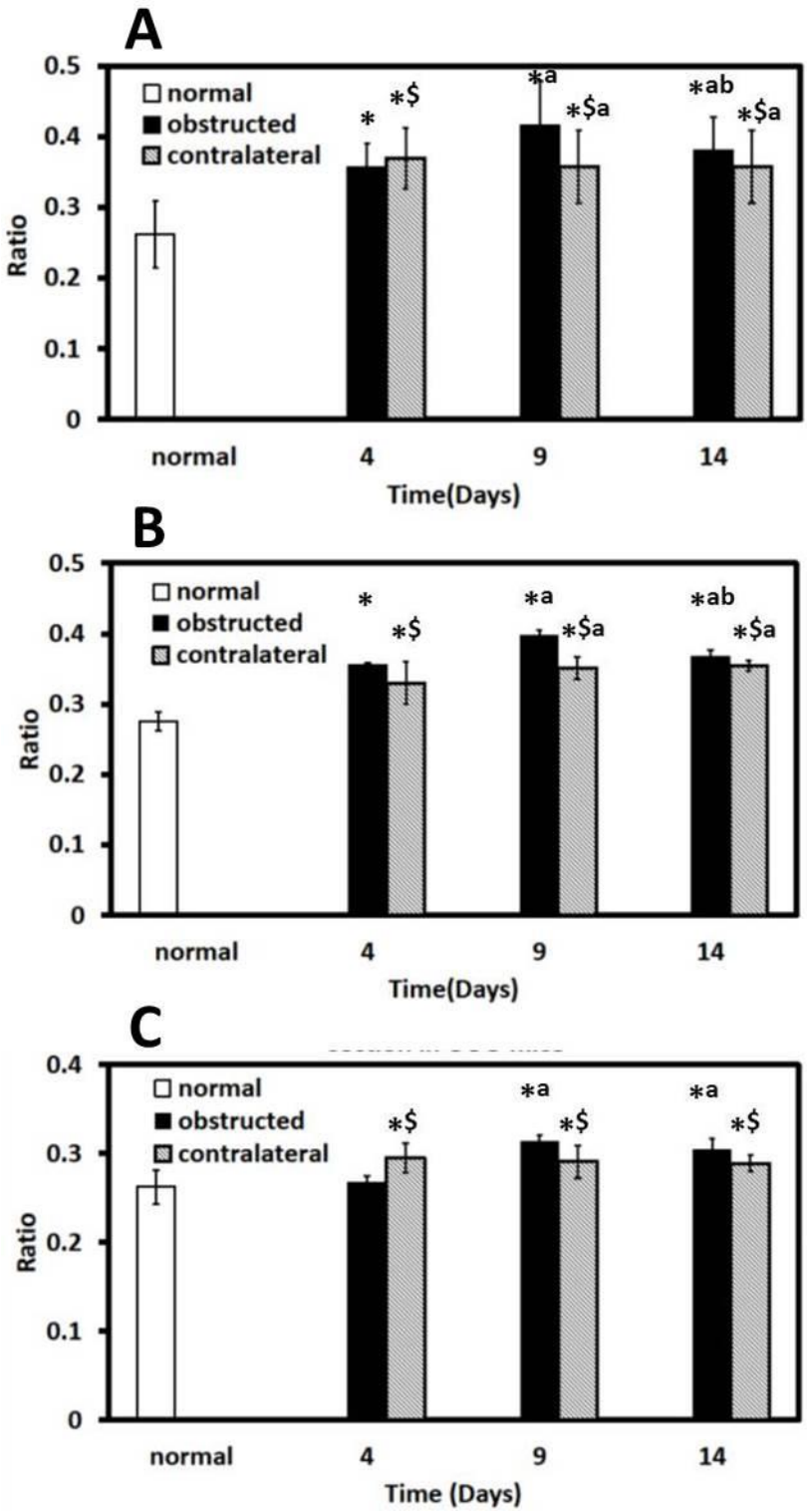

Figure 20. The unsaturation level of fatty acid chains molecules in kidney of UUO mice. The average ratio is representative of the intensity of bands at 3014 cm^{-1} and 2925 cm^{-1} on (A) the central section of whole renal tissue (B) successive sections of whole renal tissue (C) successive sections of glomeruli.

There are 4096 spectra in each FPA of renal specimen. $P < 0.05$. ***** vs. Normal. **$** vs. Obstructed. **a** vs. 4d. **b** vs. 9d

Glomerular injury scoring

In order to evaluate glomerular function in CKD, multivariate approaches of FTIR imaging is carried on to differentiate distinct tissue structures in glomeruli. Perusing the contrast agent, $BaSO_4$, helps to image the vascular network in nephrons and to quantify the glomerular injury, as well as to trace the localization of glomeruli in a serial of renal tissue sections.

We took two methods to measure quantitatively the glomerular scoring in obstructed kidneys and its contralateral kidney in each mouse. In the examination of the morphometric changes on each glomerulus, the spectral integration method is applied on each FTIR image of a series of specimens in the spectral interval of 1160-1220 cm^{-1}, assigned majorly to the absorbance of $BaSO_4$ microparticles. The reason of choosing the spectral interval mentioned above is because the integrity area of averaged spectra is between 1160 and 1220 cm^{-1} in renal tissue, and when perfused with $BaSO_4$ microparticles it is over twice as big as in non-perfused renal tissue shown in Figure 21. Thus, the integrity intensity in the spectral interval of 1160-1220 cm^{-1} can show the most significant difference, compared to the other spectra intervals in the 995-1220 cm^{-1} range.

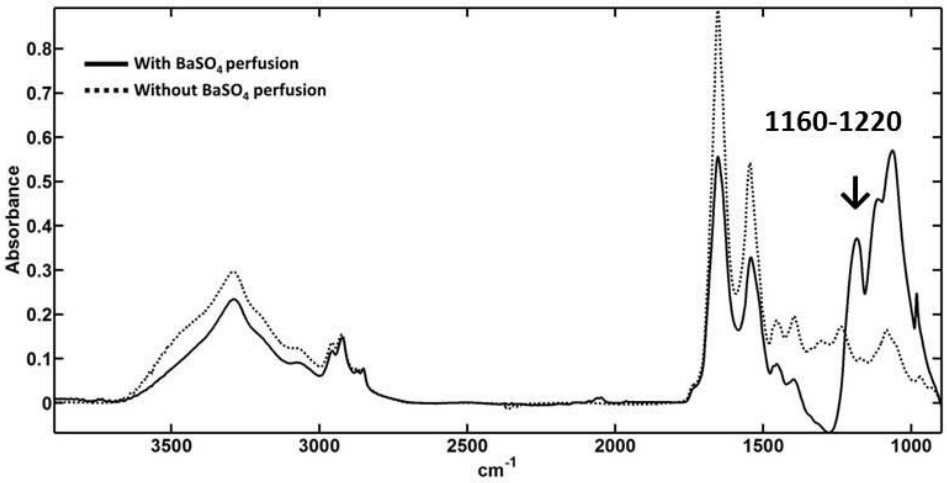

Figure 21. Average infrared spectra from renal specimens treated with or without $BaSO_4$ perfusion. The solid line is representative of the $BaSO_4$ treatment, while the dashed line is for the specimen without treatment. The spectral range for $BaSO_4$ is between 1160 cm^{-1} to 1220 cm^{-1}.

Spectral integration of representing signal intensity in 1160-1220 cm^{-1}, donated by a SO_4 group of $BaSO_4$ microparticles is a simple and useful way to clearly locate the position of glomeruli in a serial renal section. Figure 22 is the result showing the volume change of glomeruli caused by the kidney obstruction. The reduction of glomerular size in a obstructed kidney is up to 30 % at day 4, and continued up to 70 % at day 9 compared to the measurement of control group mice without surgery. At day 14, the obstructed kidney showed 70 % reduction of glomerular size, with no further shrinkage undergoing. It can be suspected that the critical value of glomerular size was reached when kidneys suffered the physiological stress. In the contralateral kidney of each group, enhanced growth on glomerular size was observed when a 30 % increase of the volume was found both at day 4 and day 9. Then, in 14 days, a decrease of glomerular volume appears, following the early-stage growth. These results show that obstruction in the kidneys lead to glomerular volume reduction, while a comprehensive growth is stimulated in its contralateral kidney.

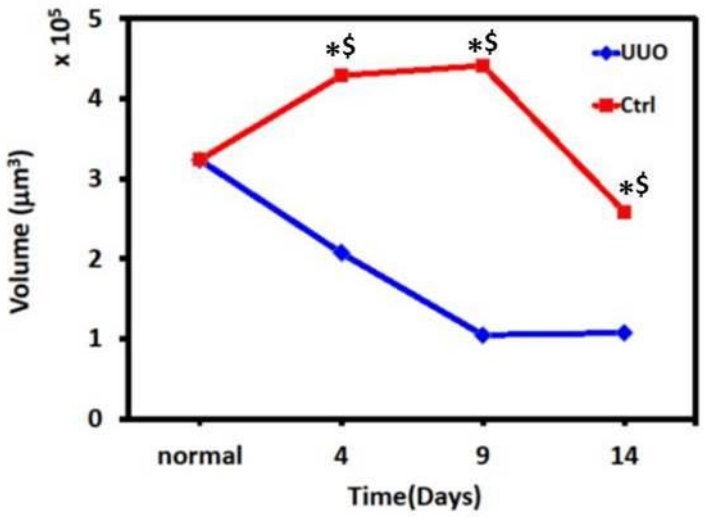

Figure 22. The variation of glomeruli volume in kidney due to UUO.

The second is determined by verifying spectral characteristics in tissue samples through clustering analysis. In our work, the CH stretching region (2800-3050 cm^{-1}) is used in the analysis, which is dominated mainly by the acyl chain of lipid molecules. In our study, 4 assemblies in clustering classification are applied to the data of obstructed kidney from 0 to 9 days, and were set in data processing as increased number of clusters was attributed to periglomerular tissue and normal glomerular composition (Figure 23 A). In this figure, the population of the black cluster was raised on the glomerular region in the obstructed kidney after 4 days, and in the contralateral kidney after 9 days of the obstruction, respectively. The spectral intensity of the black cluster's response to enhanced stress by the obstruction is generally lower than the other three clusters in most of the spectral frequency of CH stretching regions shown in figure 23 B. We further statistically examine the stereological change of the spectra feature (coded in black color) on the glomerular region in each group (Figure 24). The result shows a 2.37 fold increase of spectral feature in CH stretching region on glomeruli in the 4-day obstructed kidney, following the reduction to one-third in day 9 compared to a normal kidney. The histopathological state of CKD induced by UUO is thus stereologically elucidated by verifying the biochemical information of whole glomeruli.

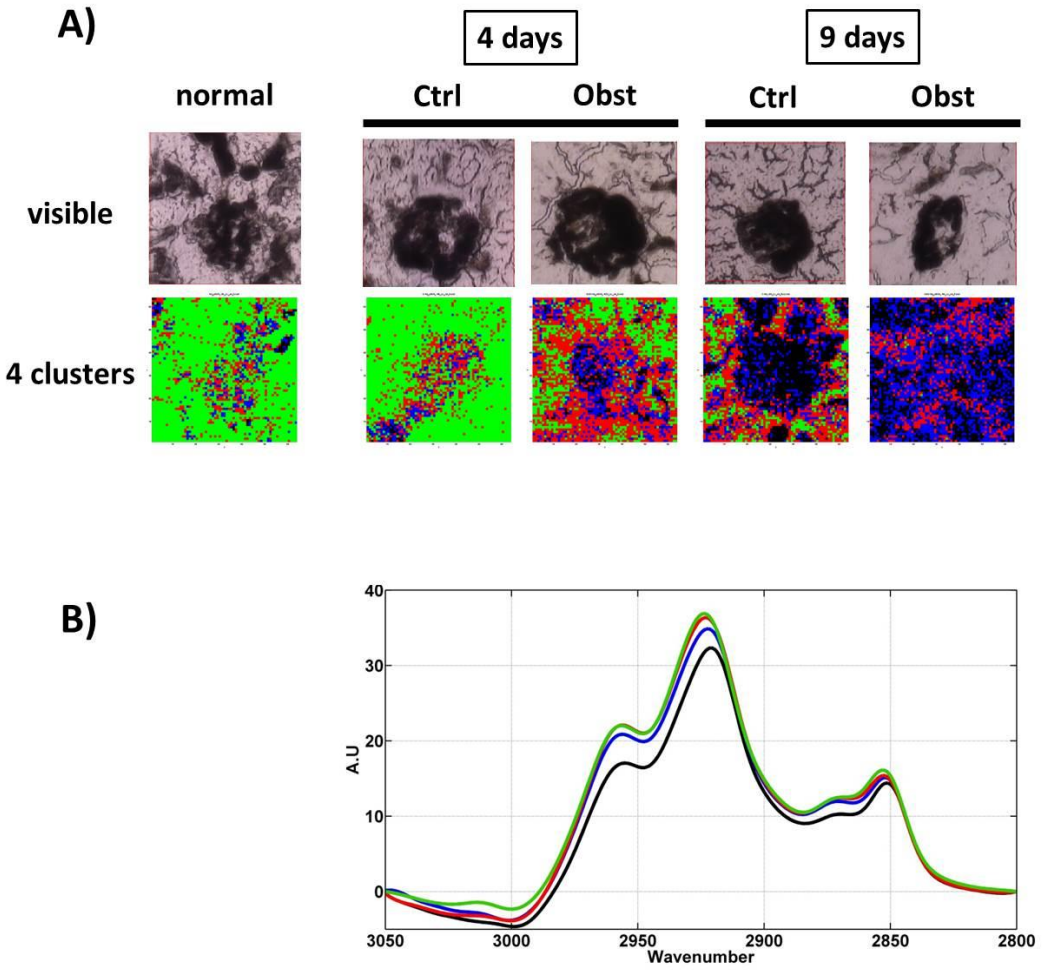

Figure 23. Spectral feature on the F.A.C. region in UUO mice. All FTIR data is treated with clustering classification in the spectral interval of 2800 cm^{-1} to 3050 cm^{-1}. Ctrl is represented by the contralateral kidney of the mice subjected to UUO. Obst is representative of the obstructed kidney. Control mouse is harvested without the surgery, marked as normal. (A) shows the bright field image, and the corresponding image of clustering results in 4 clusters. (B) is the average spectra of each cluster in renal samples analyzed in (A).

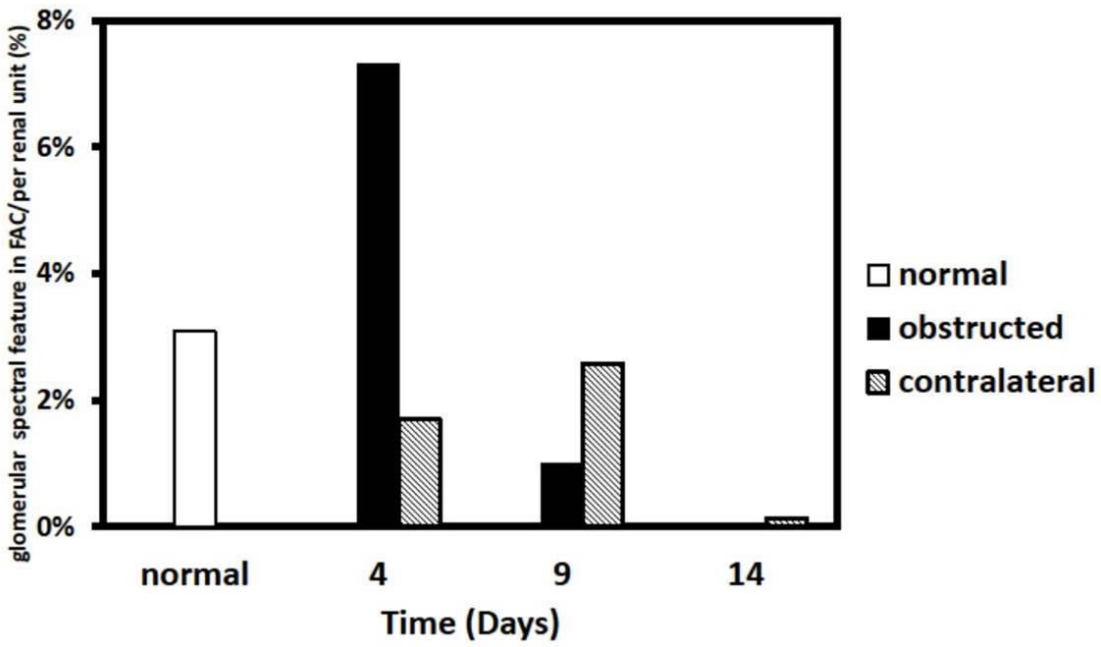

Figure 24. Stereological variation of spectral feature of glomeruli in UUO mice. The ratio is representative of the percentage of spectral feature on the F.A.C. region on glomeruli vs tissue unit. The normal kidney is labelled as a blank column. Black is for the obstructed kidney, while the sloped-dashed line is for the contralateral kidney.

3D imaging of glomeruli with multiple purposes

As discussed above, 2D FTIR imaging of glomeruli in CKD were investigated either by clustering analysis or by curve fitting, revealing the distribution and content changes of chemical components following the progression of CKD. The next aim is to acquire spatial information of glomeruli in the matter of quantity, and also the geometry on consecutive tissue specimens. Figure 25 A shows the FTIR image of glomeruli based on integrated absorbance that is mainly dominated by perfused $BaSO_4$ microparticles (1160-1220 cm^{-1}). The change in the vasculature network of glomeruli in the development of CKD is discriminated. A more compressed form of glomeruli vasculature architecture was observed in the obstructed kidney at day 4, compared to a normal kidney, which exhibited a loose wrap of capillary vessels through moving 3D imaging (Supply material). Further examination (Figure 25 B) of 3D spectral features in the C-H stretching region (2800-3050 cm^{-1}) on glomeruli was plotted, showing the

stereological distributions of identified clusters sensitive to stress induced by UUO, which is discussed in figure 23. Significantly geometric alternations in the localization of chemical groups on glomeruli is revealed by 3D FTIR imaging in our renal study. Merging the image data shows the change in stereological information on glomeruli under pathological stress (figure 25 C). Hence, the combination of more than one set of 3D image data indicates the distinct discovery of transformed patterns in morphology and physiology on glomeruli, providing a practical way towards multi-imaging approaches in handling tissue specimens.

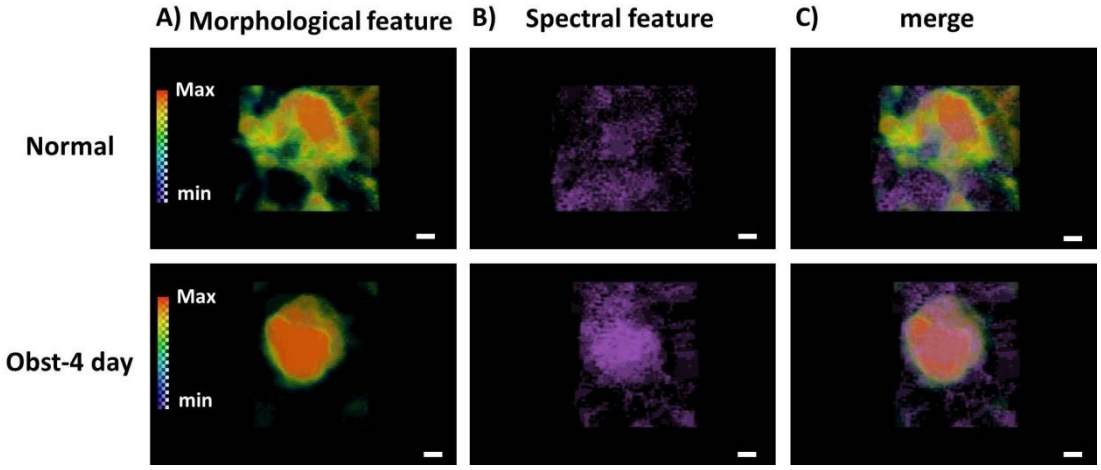

Figure 25. 3D imaging of morphological structure and spectral feature on glomeruli in mice after 4-day UUO and normal mice. The extracted 3D projection pictures illustrate the glomerular structure based on the spectral intensity of $BaSO_4$ microparticles, which are shown in (A), where high levels are shown in red, and transparent blue is for low expression. (B) indicates the spectral feature on the F.A.C. region on glomeruli by clustering analysis. Merged images in (C) display the correlation and colocalization of morphology and biochemical details on glomeruli. Scale bar is representative of 20 μm (supplementary material provided online).

Publication No. 3 (Participation):

Foreword

The Inserm U1029 LAMC Laboratory in Bordeaux and the Academia Sinica Nano-X Laboratory in Taipei have initiated a collaboration for developing 3D multimodal imaging in biomedical sciences. In Bordeaux, the chemical imaging is developed with FTIR microscopy with the aim of providing a global and quantitative 3D imaging tool to analyze biosamples. In Taipei, the aim is to develop high-resolution X-ray tomography of biosamples to analyze the structure and organization of 3D blood network in small animal models. They join their efforts in order to develop the first comprehensive technology set, able to characterize in detail the development of tumor vasculature and its impact on tumor micro-environment. Initiated in 2008, this collaboration has led to the development of imaging contrast agents usable for different imaging techniques, i.e. contrast agents that are responsive to X-Rays, infrared photons and fluorescent. It has also pushed the partners to merge their datasets to perform 3D reconstructions of blood vasculature based on different imaging techniques. Lastly, they are developing 3D data treatment methods for extracting and exploiting the biological information contained in images of different origins. The first paper presented here is the starting point of a new avenue for multimodal 3D imaging, i.e., the development of a common contrast agent that can be used for different imaging techniques.

Title: Very small photoluminescent gold nanoparticles for multimodality biomedical imaging

Motivation

As mentioned above, the requirement of obtaining image data by X-ray microscopy relies on the usage of contrast agents. It also helps the measurement of IR imaging on biosamples. In recent years, the development of contrast agents for imaging techniques has revealed significant improvement in improving many aspects of bioimaging, including that of data quality, data treatment and presenting better image visualization. With the usage of gold-NPs and barium sulfate microparticles, respectively, in X-ray based and IR-based bioimaging, we demonstrate the practical application of these two biocompatible contrast materials for the imaging of the microvasculature of glioma, or the long-term monitoring of tumor cell growth within the brain. Previous studies and unpublished data in our laboratory, as well as collaboration with Taiwan partners, showed that the morphological and/or geometric information of gold-NPs and barium sulfate in the blood vessel of brain tumor can be used to distinguish tumor growth from the non-tumor tissue, and can also be used to discriminate the tumor types by the multimodal imaging of combining X-ray and FTIR. For multimodal bioimaging, image agents have the characterization of visualization and quantization for more than one image technique. In this paper, we propose the development of a new contrast agent for functional histology, with multimodal properties by X-ray, IR and luminescent microscopies. This strategy for imaging quantitatively molecular information of examined biosamples could be used to merge multifunctional investigations for diagnosis and prognosis in clinics and laboratory research.

Result in this paper

Very small sized gold-NPs are synthesized by carefully tuning the parameters of the chemical precursors and irradiation time by X-ray light source. The dual optical properties of high x-ray attenuation and

photoluminescence excitation of these very small gold-NPs (ψ1.4 nm±0.3 nm) provides the unique capability of performing functional/morphological information in *in vivo* bioimaging. Proper surface chemistry of these very small gold-NPs allows a large amount of internalized gold-NPs in the cellular cytoplasm that did not induce in obviously either cellular proliferation, or cellular death. Furthermore, appropriate quantitative estimation is highly feasible to study NP content within the tissues. Also, the preliminary result implies that the potential of the very small gold-NPs as a drug carriers for therapeutics. This multimodal imaging agent characterized with visible light fluorescence and X-ray absorption is thus considered as a good imaging tool for histopathological imaging.

Perspective

Our studies in this paper have shown that a newly developed contrast agent has the dual optical properties of imaging capability for functional investigation of histopathology with the respect of disease. The approach of using photo-luminescent gold-NPs for functional FTIR/X-ray micro-tomography imaging allows for the evaluation of microvasculature related to pathological conditions. Based on the spectral information, it can be determined if there is abnormal morphology of blood vessels in the blood capillary within the tissue, either with leakage or fenestrae depending on the pathological mechanism of disease. Moreover, the vasculature density within investigated tissue can be determined by the stereological analysis of 3D X-ray data for studying disease-related angiogenesis. This approach of combining imaging technique and appropriate contrast agents may be used to provide a convenient tool for routine diagnosis in pathology.

Work description

The newly synthesized gold nanoparticles with irradiation exposure have multioptical characteristics, which are encouraging signs for their potential applications within biomedical research. The first

experiment for the biocompatibility estimation was to perform a cellular toxicity assay to directly count the surviving cell numbers in cultured cells exposed to our newly synthesized gold-NPs. Loading large amounts of gold-NPs into the cultured cells showed photoluminescent signals excited from the cellular cytoplasm, indicating that engulfed NPs contributed mainly to the detection of fluorescence light, not the attached clusters of NPs on the cell membrane. We also performed the imaging experiment of visualizing these very small gold-NPs accumulated in cells by using high-resolution TXM microscopy. The image results are not as significant as the ones acquired by confocal microscopy. Thus, the following animal experiment of implanting tumor cells pre-cultured with photoluminescent gold-NPs for a few days was performed to evaluate the distribution and visualization of these gold-NPs in a subcutaneous tumor development. Our results by hard X-ray microscopy showed the contrast signals attributed to the X-ray absorption of gold-NPs in inoculated tumor tissue within a small animal. By using confocal imaging, it was confirmed that the existence of gold-NPs excited the red fluorescence in the incised tumor region of the animal. We can propose that the multimodal properties of our very small gold-NPs are a good candidate to be used in biomedical research by X-ray, photoluminiscent or possible IR imaging modality.

Biotechnology Advances 31 (2013) 362–368

Contents lists available at SciVerse ScienceDirect

Biotechnology Advances

journal homepage: www.elsevier.com/locate/biotechadv

Very small photoluminescent gold nanoparticles for multimodality biomedical imaging ☆

Sheng-Feng Lai [a,b], Chia-Chi Chien [b], Wen-Chang Chen [a,**], Hsiang-Hsin Chen [b], Yi-Yun Chen [b], Cheng-Liang Wang [b], Y. Hwu [b,c,d,*], C.S. Yang [e], C.Y. Chen [f], K.S. Liang [g], Cyril Petibois [h], Hui-Ru Tan [i,j], Eng-Soon Tok [i,j], G. Margaritondo [k]

[a] Department of Chemical and Materials Engineering, National Yunlin University of Science and Technology, Yunlin 640, Taiwan
[b] Institute of Physics, Academia Sinica, Nankang, Taipei 115, Taiwan
[c] Department of Engineering and System Science, National Tsing Hua University, Hsinchu 300, Taiwan
[d] Advanced Optoelectronic Technology Center, National Cheng Kung University, Tainan 701, Taiwan
[e] Center for Nanomedicine, National Health Research Institutes, Miaoli 350, Taiwan
[f] National Synchrotron Radiation Research Center, Hsinchu 300, Taiwan
[g] Electrophysics Department, National Chiao Tung University, Hsinchu 300, Taiwan
[h] Université de Bordeaux, CNRS UMR 5248-CBMN, F33405 Talence-Cedex, France
[i] Physics Department, National University of Singapore, Singapore 117542
[j] Institute of Materials Research and Engineering, A*STAR, S117602, Singapore
[k] Ecole Polytechnique Fédérale de Lausanne (EPFL), CH-1015 Lausanne, Switzerland

ARTICLE INFO

Available online 30 May 2012

Keywords:
Photoluminescence
Au nanoparticles
X-ray imaging
Cellular uptake
Radiation synthesis
Cytotoxicity
Tumor development

ABSTRACT

An original synthesis method based on X-ray irradiation produced gold nanoparticles (AuNPs) with two important properties for biomedical research: intense visible photoluminescence and very high accumulation in cancer cells. The nanoparticles, coated with MUA (11-mercaptoundecanoid acid), are very small (1.4 nm diameter); the above two properties are not present for even slightly larger sizes. The small MUA-AuNPs are non-cytotoxic (except for very high concentrations) and do not interfere with cancer cell proliferation. Multimodality imaging using visible light fluorescence and X-ray microscopy is demonstrated by tracing the nanoparticle-loaded tumor cells.

1. Introduction

The interaction of AuNPs with cells was intensively investigated (Besner et al., 2009; Daniel and Astruc 2004; Ghosh et al., 2008; Giljohann et al., 2010; Jana et al., 2001; Sau et al., 2001; Schwartzberg et al., 2004; Sivaraman et al., 2010; Yang et al., 2008), in particular as far as physical and biological size effects are concerned (Alkilany and Murphy 2010; Connor et al., 2005; Murphy et al., 2008; Ryan et al., 2007; Shah et al., 2011; Wang SG et al., 2008). However, the properties of very small (<2 nm) nanoparticles are still only partially known. There is an apparent conflict between two basic requirements for biomedical applications: photoluminescence (e.g., for cancer cell tracing) and strong cell accumulation. Indeed, Zheng et al., and other authors (Bo et al., 2007; Duan and Nie; 2007; Lin et al., 2009 Zheng et al., 2007) reported photoluminescence from very small AuNPs or nanoclusters. In parallel, few reports (Chithrani et al., 2006; Jiang et al., 2008) argued that larger (15–50 nm) AuNPs produce the strongest cell accumulation effects.

We were able to reconcile these two properties by using MUA capping and an original synthesis method based on X-ray irradiation of the precursor solution. This approach produced very small (1.4 nm) MUA-AuNPs that are photoluminescent and strongly accumulate in cancer cells. Furthermore, gold is an X-ray absorber; therefore, our nanoparticles can be also useful for multimodality (photoluminescence and X-ray) imaging.

Both features of the fabrication method – MUA coating and X-ray irradiation – were independently tested in previous studies. X-ray irradiation of the precursor solution produced colloids of metallic

☆ A new type of Au nanoparticles showing strong photoluminescence and high cellular uptake enables in vivo multimodality (X-ray and visible light) imaging and tracing of mouse tumors.

* Correspondence to: Y. Hwu, Institute of Physics, Academia Sinica, Nankang, Taipei 115, Taiwan. Fax: +886 2 2789 6721.
** Correspondence to: W.-C. Chen, Department of Chemical and Materials Engineering, National Yunlin University of Science and Technology, Yunlin 640, Taiwan.
E-mail addresses: ChenWC@yuntech.edu.tw (W.-C. Chen), phhwu@sinica.edu.tw (Y. Hwu).

0734-9750/$ – see front matter © 2012 Elsevier Inc. All rights reserved.
doi:10.1016/j.biotechadv.2012.05.005

nanoparticles and nanorods with very high concentration and excellent long-term stability. (Cai et al., 2010; Liu et al., 2008; Wang et al., 2007a, 2007b, 2008a, 2008b, 2011; Yang et al., 2006) MUA coating was used to control the AuNP dimension down to 1–2 nm, obtain narrow size distributions, and to ensure biocompatibility (Lai et al., 2011). By combining the two features, we discovered that small nanoparticles combine the three interesting properties reported here. The small size is critical for such properties: even a slight diameter increase from 1.4 to 2.2 nm eliminates the photoluminescence and reduces the accumulation in EMT-6 cell by a factor >20.

To analyze these size effects, we irradiated with X-rays precursor solutions with different MUA/Au molar ratios, R, that produced different average diameters. Details of the size control and the radiation affect are reported elsewhere (Lai et al., 2012). The nanoparticles were then characterized with a variety of techniques including inductively coupled plasma mass spectrometry (ICP-MS), transmission electron microscopy (TEM), small-angle X-ray scattering (SAXS), Fourier transform infrared (FTIR) spectroscopy, zeta-potential analysis, photoluminescence spectroscopy, cell viability analysis, ultraviolet–visible (UV–VIS) spectroscopy and thermogravimetric

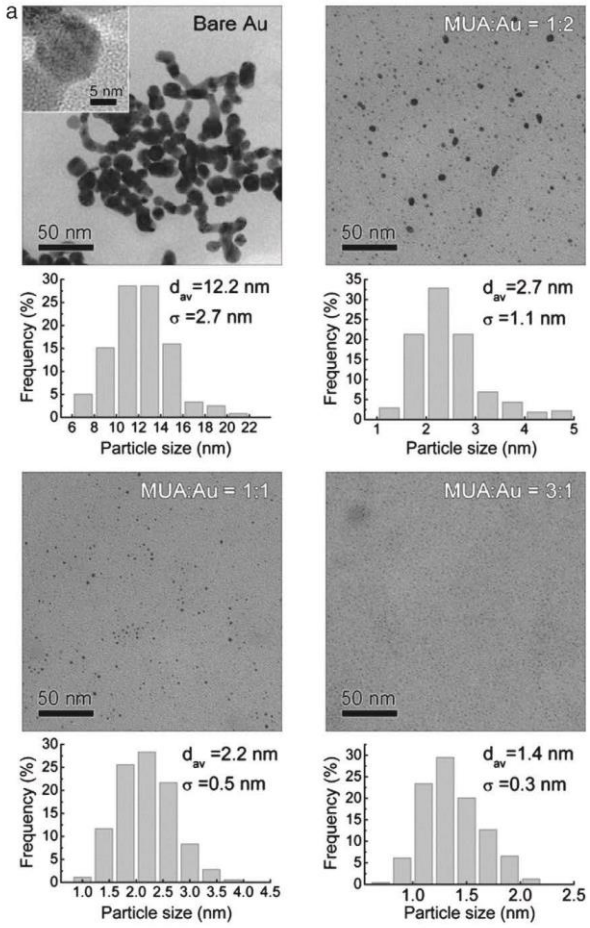

Fig. 1. (a) TEM micrographs with the corresponding size histograms (n>200) and (b) UV–visible spectra of AuNPs synthesized without MUA and with MUA/Au ratios R=0.5, 1 and 3. (c) SAXS scattering profiles of MUA-AuNP colloids with 1 and 0.1 mg ml^{-1} concentration. The 1 mg ml^{-1} profile shows the peaks of interparticle interference at scattering vector magnitudes q=0.015 and 0.034 Å^{-1}, and a hump of the form factor at q=0.3 Å^{-1}. The scattering profile of the 0.1 mg ml^{-1} nanoparticle colloid was fitted using a fuzzy sphere model; the results indicate that the diameter of the nanoparticles plus the MUA coating is ≈3.75 nm.

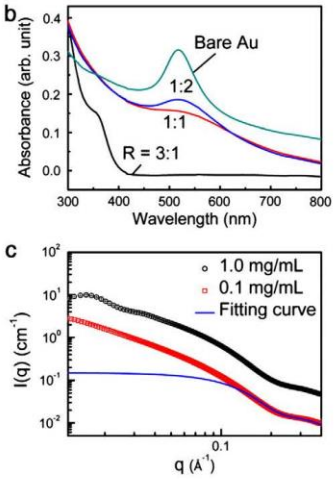

Fig. 1 (*continued*).

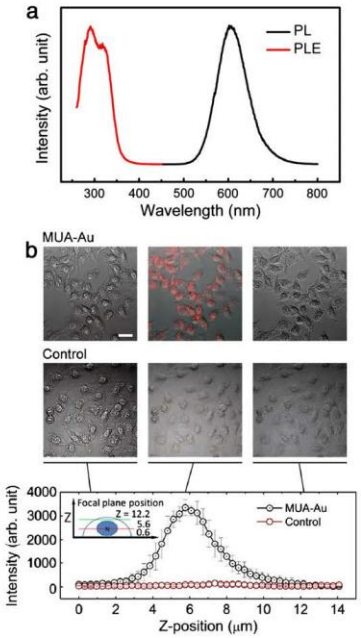

Fig. 2. (a) Photoluminescence (290 nm) and photoluminescence excitation (602 nm) spectra of our 1.4 nm MUA-AuNPs. (b) Confocal photoluminescence microscopy images of EMT-6 cells with 1.4 nm MUA-AuNPs at different Z-positions (see inset in the bottom part). The photoluminescence was excited by a 405 nm laser. The control images were obtained without MUA-AuNPs. The curves on the bottom show the integrated photoluminescence intensity (averaged over 10 cells) vs. Z.

analysis (TGA). We report here the results most directly relevant to our main findings.

2. Material and methods

2.1. Materials

$HAuCl_4 \cdot 3H_2O$, MUA, sodium hydroxide, glutaldehyde, and formaldehyde were purchased from Sigma-Aldrich. All chemicals were reagent grade.

2.2. Synthesis of MUA-AuNPs

0.5 ml of 20 mM $HAuCl_4 \cdot 3H_2O$ were adjusted to pH ~11 with 0.1 M NaOH. We then added MUA dissolved in anhydrous ethanol with different molar concentrations (relative to Au) and water to reach a 10 ml volume. The solution was placed in polypropylene conical tubes and irradiated for 3 min with hard X-rays from the BL01A beamline of the NSRRC, running at a constant electron current of 300 mA. The X-ray photon energy ranged from 8 to 15 keV and was centered at ~12 keV delivering a dose rate ~4.7×10^5 Gy s^{-1}. (Liu et al., 2009) After the irradiation, the solution was concentrated by centrifugation and the unbound MUA was removed by repeated ultrafiltration with a 10 kDa molecular cutoff.

2.3. Characteristics of the MUA-AuNPs

Samples for TEM were prepared by placing a drop of the solution on a carbon-coated copper grid and dried at 40 °C. TEM measurements were performed in a JEM-2100F system at an accelerating voltage of 200 kV. UV–visible spectra were acquired over 200–800 nm using a USB4000 Fiber Optic spectrometer from Ocean Optics (Dunedin, USA) with 1 cm path length cuvette (Evergreen Scientific, USA). Small angle X-ray scattering measurements were taken at the BL23A beamline of

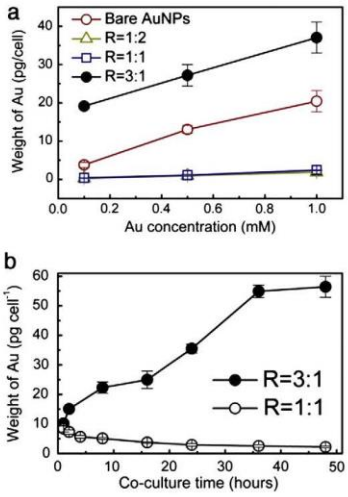

Fig. 3. (a) ICP-MS analysis of MUA-AuNP accumulation in EMT-6 cells as a function of the Au concentration in the solution; the culture time with nanoparticles was 12 hours. (b) ICP-MS analysis of the uptake by EMT-6 cells of MUA-AuNPs ($R = 3$ and 1) vs. the culture time with nanoparticles. 2×10^4 EMT-6 cells were seeded for 36 hours before adding the nanoparticles to the medium.

NSRRC with 15 keV photon energy and 1820.88 mm specimen-to-detector (MarsCCD 1024×1024 pixels) distance on 1 mg ml^{-1} and 0.1 mg ml^{-1} of the $R=3{:}1$ MUA-AuNPs. Photoluminescence spectra were measured at room temperature with a Cary Eclipse spectrophotometer (Varian, USA).

2.4. Quantitative analysis of cellular uptake of MUA-AuNPs

After preparing the EMT-6 cell as described above and waiting overnight, different concentrations of the MUA-AuNPs were added at different times. After culturing with nanoparticles, the cells were

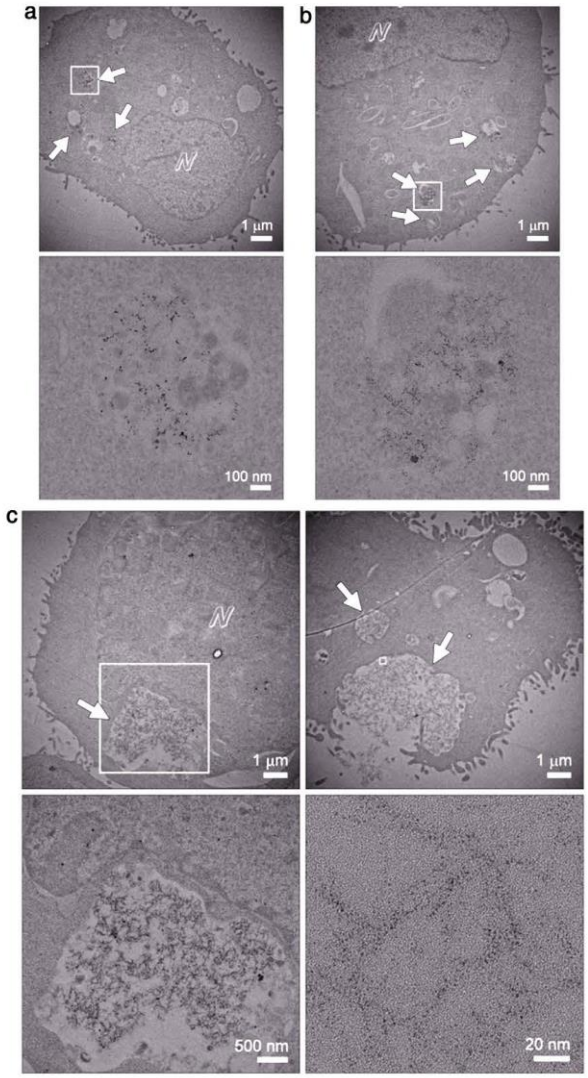

Fig. 4. TEM micrographs of EMT-6 cells cultured for 24 hours with a 0.5 mM Au concentration solution, giving MUA/Au ratio $R=0.5$ (a), 1 (b), and 3 (c). The bottom images in (a), (b) and (c) correspond to magnified view of the square areas. N is the nucleus.

trypsinized, counted and exposed to a freshly prepared aqua regia solution in an ultrasonic bath for 3 hours. The Au content of the cells was then measured by ICP-MS with an Agilent 7500cx Instrument.

2.5. Confocal microscopy

After preparing the EMT-6 cell culture and after 32 hours culturing, a 0.1 mM Au concentration equivalent of the MUA-AuNPs with a MUA/Au molar ratio of 3 was added and cultured for 24 hours. Afterwards, the cells were washed three times with 1× PBS, fixed in 4% formaldehyde solution for 10 min and placed in a PBS solution for direct observation by a confocal microscopy (Olympus IX71) with 405 nm laser excitation.

2.6. TEM observations of cell uptake

The cells were cultured on a 10 cm dish at 37 °C in a humidified 5% CO_2 atmosphere. After 24 hours, 0.5 mM of MUA-AuNP solution was added and cultured for 24 hours; the cells were then washed with 1× PBS three times, trypsin treated, fixed in 2% glutaldehyde solution for 1 hour and stained with 1% osmium tetroxide. Then, dehydration was achieved by sequential treatment with 30%, 45%, 60%, 75%, 95% and 100% ethanol, followed by 100% resin infiltration and embedding. Ultrathin sections (100 nm) prepared by an ultramicrotome were finally placed on copper grids.

BALB/c mice (20 ± 2 g, 4 weeks old) were acquired from the National Laboratory Animal Center, fed with sterile food and sterile water with pH, and kept at 7.0–7.5, while housed in isolated cages with a 12-h light/dark cycle. CT-26 cells were cultured with 500 μM MUA-AuNPs in medium RPMI-1640 with 10% FBS (fetal bovine serum) and grown in a 5% CO_2 incubator. After culturing for 24 hours, cells 1×10^6 cells per 100 μl were injected via tail vein for metastatic lung cancer development; 5×10^5 cells per 50 μl were locally injected in for metastatic liver cancer development spleen for 26 days. EMT-6 cells were cultured with 500 μM MUA-AuNPs for 24 hours, after trypsin treatment. Then, harvested cells were added to PBS. Fifty microliters of 1×10^7 cells ml^{-1} EMT-6 cell solution were inoculated in the subcutaneous tissue of the left thigh region.

3. Results and discussion

Fig. 1 illustrates the effects of MUA on the nanoparticle size. Fig. 1(a) compares TEM images (by a JEM-2100F system operating at 200 kV) of bare-AuNP and MUA-AuNP samples prepared by placing a drop of the colloid on a carbon-coated copper grid and drying at 40 °C. The size effects are evident; we derived from images of this type average diameters of 12.2, 2.7, 2.2 and 1.4 nm for bare AuNPs and for MUA-coated AuNPs corresponding to $R=0$, 0.5, 1 and 3; no further size decrease was observed for R-values above 3.

The UV–visible spectra of Fig. 1(b) confirm this progressive size decrease—see the blue shift and gradual suppression of the Au surface plasmon peak. Fig. 1(c) shows SAXS results; by fitting them with the fuzzy sphere model, we confirmed an overall size <4 nm including the MUA coating (Stieger et al., 2004). As R increases, not only the size decreases but also the size distribution width, reaching ±0.27 nm (~±20%) for $R=3$.

Fig. 2 shows that our 1.4 nm MUA-AuNPs do produce photoluminescence, perhaps due to quantum confinement effects (Huang et al., 2007; Zheng et al., 2003). No photoluminescence was observed instead for larger MUA-AuNPs or bare AuNPs. Fig. 2(a) shows the photoluminescence (PL) (black) and photoluminescence excitation (PLE) (red) spectra measured at room temperature with a Varian Cary Eclipse spectrophotometer.

Fig. 2(b) shows confocal visible micrographs under laser excitation (405 nm) of EMT-6 cells after 24 hour culture with 1.4 nm MUA-AuNPs, triple 1× PBS washing, fixing in 4% formaldehyde solution for 10 min and replacement in a 1× PBS solution. The images were taken for different focal positions along the Z-axis, perpendicular to the substrate (see the inset in the bottom part). Note the photoluminescence in the top-middle image.

The bottom part of Fig. 2(b) shows the emitted intensity vs. Z. Basically, the most intense photoluminescence originates from the middle of the cells, apparently from the area surrounding the cell nucleus. This implies of course that the photoluminescent nanoparticles are inside the cell rather than on the membrane. This demonstrates that AuNPs accumulated in cytosol without crossing the nuclear membrane, thus preventing interaction with nucleus. This cytosolic accumulation also suggests that Au-NPs were vesiculated.

Fig. 3 deals with the nanoparticle accumulation in cancer cells. Fig. 3(a) shows the total Au equivalent accumulation in EMT-6 cells for different R-values. The results were obtained with an ICP-MS instrument, after trypsinizing, counting and exposing the cells to a fresh aqua regia solution in an ultrasonic bath for 3 hours. Note the strong accumulation for the smallest nanoparticles (1.4 nm) and the aforementioned dramatic decrease for slightly larger (2.2 nm) diameters.

These results should be compared to previous reports (Chithrani & Chan, 2007; Chithrani et al., 2009; Jin et al., 2009; Malugin & Ghandehari 2010; Wang et al., 2010; Zhang et al., 2009a) that optimal cell accumulation for AuNPs occurs for 20–50 nm diameters. Our tests for bare nanoparticles are generally consistent with this conclusion. However, we found that MUA-coating drastically changes the situation: the accumulation is best for the smallest nanoparticles.

Fig. 3(b) shows that the accumulation per cell of the 1.4 nm MUA-AuNPs, already high after 12 hours of culture, further increases with the culture time for at least 36 hours. The accumulation per cell for 2.2 nm MUA-AuNPs decreases instead with time: this is due to the fast increase of the cell number by proliferation. The uptake of MUA-AuNPs did not induce detectable effect on cells proliferation, providing further evidence that the nanoparticles are highly biocompatible. Note that the accumulation of 1.4 nm MUA-AuNPs in EMT-6 cells is high not only with respect to larger nanoparticles but also in absolute terms. The level reaches indeed ~57 pg/cell, equivalent to ~2.1×10^9 nanoparticles/cell and to a total of ~1.0×10^{11} available binding sites on MUA per cell (since the average is ~49 for each MUA-AuNP). To the best of our knowledge, such accumulation levels were not reported for this or any other kind of cells which also suggests high biocompatibility.

The above main results were complemented by those of many other tests. The TEM measurements of Fig. 4 show examples of MUA-AuNPs for $R=0.5$, 1 and 3 in the cell cytoplasm. These

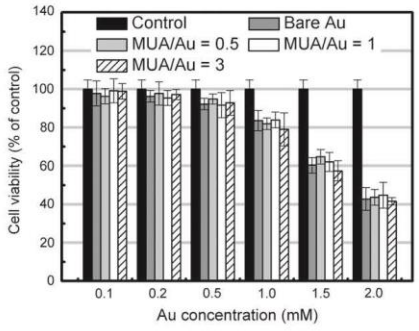

Fig. 5. Cell viability assay of EMT-6 cells co-cultured for 24 hours with different Au concentrations in culture medium and for different R-values.

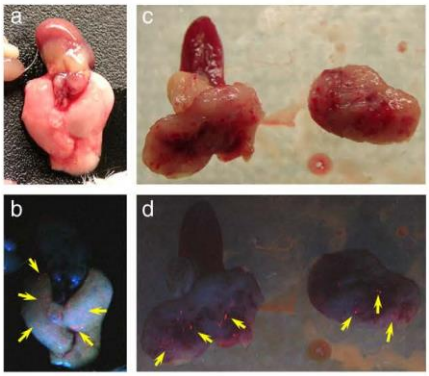

Fig. 6. Photoluminescent MUA-AuNP-loaded CT-26 cells detected in lung (a and b) and spleen tissues (c and d). (a) and (c) are optical images produced by visible light illumination. (b) and (d) are images obtained under exposure to UV light (wavelength: 260 nm): examples of photoluminescent tumor cells are marked by arrows. (c) and (d) show a mouse spleen with a developed a tumor; the organ is cut in two. The dark red portion (top) of the left part is the healthy region showing no photoluminescence. Photoluminescent spots are visible instead in the tumor-containing part of the spleen.

nanoparticles were found to be compartmentalized in cytoplasm due to endocytosis. We detected in particular 1.4 nm AuNPs in the high magnification TEM images, Fig. 4(c), indicating an endocytosis internalization route consistent with the fluorescence microscopy results, i.e., with strong accumulation only in the cytoplasm area. These TEM images did not reveal any nanoparticles in the nucleus. These findings confirmed the photoluminescence results: the nanoparticles were primarily present in the cytoplasm area and no nanoparticles were found in the nucleus.

Without involving another internalization route, the very high uptake of the 1.4 nm MUA-AuNPs can only be explained by a similarly high accumulation on the cell surface, which is likely due to a stronger surface interaction related to the special surface properties of the AuNPs. Whether such interaction is due to the higher concentration of MUA molecules or the smaller AuNP size is not clear at present.

We also performed preliminary tests on using our photoluminescent nanoparticles for drug delivery. Specifically, we analyzed MUA as a linker to conjugate doxorubucin and other cancer drugs. The first results show that the conjugation occurs without significantly affecting the MUA-AuNPs photoluminescence.

As far as accumulation in cells is concerned, we explored the possibility that the accumulated nanoparticles are subsequently excreted. However, tests performed by replacing the nanoparticle colloid with DMEM/F12 medium provided no evidence for this hypothesis.

Particularly important are the results on cytotoxicity, obtained by cell trypsination and counting with a hemocytometer. Figs. 5 shows that little or no cytotoxicity up to an equivalent Au concentration of 1.0 mM in the culture medium, whereas the cell viability did decrease beyond 1.0–1.5 mM. This is consistent with other studies (Huang et al., 2007; Li et al., 2009; Naqvi et al., 2010; Zhang et al., 2009b; Zheng et al., 2003). However, our results do not agree with the notion that <1.8 nm gold nanoparticles are highly cytotoxic (Pan et al., 2007). Since the coating molecule is different in previous studies, the observed difference suggests that the surface chemistry of the nanoparticles could play a much more important role in the cell toxicity. In fact, due to the coating our 1.4 nm MUA-AuNPs did not affect cell viability except for the above very high equivalent Au concentrations. The observed acute toxicity in <1.8 nm AuNPs observed by Pan et al. could then be consistent with our finding that is caused by a much higher rate of internalization.

We would like to conclude by mentioning two examples of the possible uses of our photoluminescent nanoparticles. First, we verified that their accumulation makes it possible to easily detect tumors in mice after injecting them from the tail vein (ICP-MS data, not shown). The photoluminescence was still present after the nanoparticles resided in tissue for more than 20 days, with no decrease in intensity.

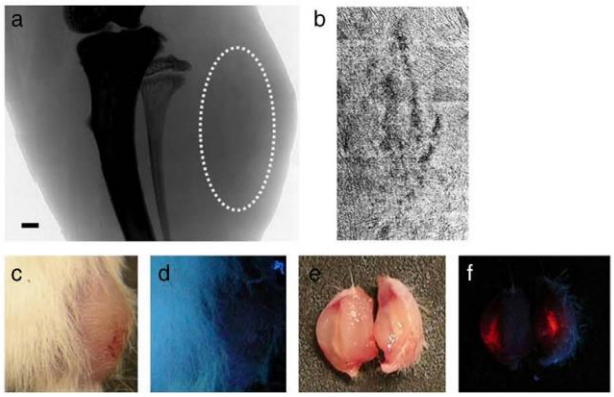

Fig. 7. (a) Projection view of a mouse leg taken in vivo with high resolution microradiography showing a tumor induced by EMT-6 cells loaded with photoluminescent MUA-AuNPs. Scale bar: 500 μm. The dashed ellipse marks the area where the EMT-6 cells were inoculated 6 days before image acquisition. The zoomed-in view (b) emphasizes the cell location by artificial enhancement of the image contrast. The photoluminescence cannot travel through thick tissue and therefore is not visible in picture (d); to detect it, the tissue must be incised as in (e) and (f). Photoluminescence visible at shallow locations underneath the surface (f) indicates that the MUA-AuNPs were transported to the tumor boundary after several generations of cell division. (c) and (e) are photographic images of the tumor at the original subcutaneous location and after incision. (d) and (f) are the corresponding images under photoluminescence-inducing UV illumination.

Second, we found that EMT-6 and CT-26 cells loaded with our photoluminescent nanoparticles kept the ability to develop tumors. As shown in Fig. 6, nanoparticle-loaded CT-26 cells were found in the lung and spleen where their red photoluminescence was clearly visible (yellow arrows in Figs. 6(b) and 4(d)) 10 days after injection from tail veins.

Likewise, MUA-AuNP loaded EMT-6 cells were used to allow tumor growth after subcutaneous inoculation. As shown in Fig. 7, in this case the tumor detection exploited in parallel the photoluminescence for optical imaging and the Au-induced absorption for X-ray imaging. In Fig. 7(a) and (b), the dark features are due indeed to X-ray absorption marking the tumor core.

We can conclude from all these tests that our MUA-AuNPs exhibit, at the same time, very small and uniform size, intense photoluminescence, strong accumulation in cells, high biocompatibility and no interference with cancer cell proliferation. Such characteristics can lead to interesting applications to cancer studies and other domains, some of which were positively tested by preliminary experiments. In particular, the very high surface area to mass ratio, the nearly complete coverage by MUA and the very high cell accumulation makes our nanoparticles good candidates as labeling agents or drug carriers. They are also more likely to be applied for multimodal imaging studies, allowing a comparison of experimental results (by X-Ray imaging, FTIR, Raman, etc.) to conventional photoluminescence and histology analysis for validation.

Acknowledgements

This work was supported by the ANR-NSC French-Taiwan bilateral program no. ANR-09-BLAN-0385, the National Science and Technology Program for Nanoscience and Nanotechnology, the Thematic Research Project of Academia Sinica, the Biomedical Nano-Imaging Core Facility at National Synchrotron Radiation Research Center (Taiwan), the Fonds National Suisse pour la Recherche Scientifique and the Center for Biomedical Imaging (CIBM, supported by the Louis-Jeantet and Leenards foundations).

References

Alkilany AM, Murphy CJ. J Nanopart Res 2010;12:2313.
Besner S, Kabashin AV, Winnik FM, Meunier M. J Phys Chem C 2009;113:9526.
Bo Y, Zhong C, Vu DM, Temirov JP, Dyer RB, Martinez JS. J Phys Chem C 2007;111:12194.
Cai XQ, Wang CL, Chen HH, Chien CC, Lai SF, Chen YY, et al. Nanotechnology 2010;21:335604.
Chithrani BD, Chan WCW. Nano Lett 2007;7:1542.
Chithrani BD, Ghazani AA, Chan WCW. Nano Lett 2006;6:662.
Chithrani BD, Stewart J, Allen C, Jaffray DA. Nanomed Nanotechnol Biol Med 2009;5:118.
Connor EE, Mwamuka J, Gole A, Murphy CJ, Wyatt MD. Small 2005;1:325.
Daniel MC, Astruc D. Chem Rev 2004;104:293.
Duan H, Nie S. J Am Chem Soc 2007;129:2412.
Ghosh P, Han G, De M, Kim CK, Rotello VM. Adv Drug Deliv Rev 2008;60:1307.
Giljohann DA, Seferos DS, Daniel WL, Massich MD, Patel PC, Mirkin CA. Angew Chem Int Ed 2010;49:3280.
Huang CC, Yang Z, Lee KH, Chang HT. Angew Chem Int Ed 2007;119:6948.
Jana NR, Gearheart L, Murphy CJ. Langmuir 2001;17:6782.
Jiang W, Kim BYS, Rutka JT, Chan WCW. Nat Nanotechnol 2008;3:145.
Jin H, Heller DA, Sharma R, Strano MS. ACS Nano 2009;3:149.
Lai SF, Chen WC, Wang CL, Chen HH, Chen ST, Chien CC, et al. Langmuir 2011;27:8424.
Lai SF, Chien CC, Chen WC, Chen YY, Wang CH, Hwu Y, Yang CS, Margaritondo G. RSC Adv 2012;2:6185.
Li JL, Wang L, Liu XY, Zhang ZP, Guo HC, Liu WM, et al. Cancer Lett 2009;274:319.
Lin CAJ, Yang TY, Lee CH, Huang SH, Sperling RA, Zanella M, et al. ACS Nano 2009;3:395.
Liu CJ, Wang CH, Chien CC, Yang TY, Chen ST, Leng WH, et al. Nanotechnology 2008;19:295104.
Liu CJ, Wang CH, Wang CL, Hwu Y, Lin CY, Margaritondo G. J Synchrotron Radiat 2009;16:395.
Malugin A, Ghandehari H. J Appl Toxicol 2010;30:212.
Murphy CJ, Gole AM, Stone JW, Sisco PN, Alkilany AM, Goldsmith EC, et al. Acc Chem Res 2008;41:1721.
Naqvi S, Samim M, Abdin MZ, Ahmed FJ, Maitra AN, Prashant CK, et al. Int J Nanomed 2010;5:983.
Pan Y, Neuss S, Leifert A, Fischler M, Wen F, Simon U, et al. Small 2007;3:1941.
Ryan JA, Overton KW, Speight ME, Oldenburg CM, Loo L, Robarge W, et al. Anal Chem 2007;79:9150.
Sau TK, Pal A, Jana NR, Wang ZL, Pal T. J Nanopart Res 2001;3:257.
Schwartzberg AM, Grant CD, Wolcott A, Talley CE, Huser TR, Bogomolni R, et al. J Phys Chem B 2004;108:19191.
Shah NB, Dong JP, Bischof JC. Mol Pharm 2011;8:176.
Sivaraman SK, Kumar S, Santhanam V. Gold Bull 2010;43:275.
Stieger M, Pedersen JS, Lindner P, Richtering W. Langmuir 2004;20:7283.
Wang CH, Chien CC, Yu YL, Liu CJ, Lee CF, Chen CH, et al. J Synchrotron Radiat 2007a;14:477.
Wang CH, Hua TE, Chien CC, Yu YL, Yang TY, Liu CJ, et al. Mater Chem Phys 2007b;106:323.
Wang CH, Liu CJ, Wang CL, Hua TE, Obliosca JM, Lee KH, et al. J Phys D Appl Phys 2008a;41:195301.
Wang SG, Lu WT, Tovmachenko O, Rai US, Yu HT, Ray PC. Chem Phys Lett 2008b;463:145.
Wang SH, Lee CW, Chiou A, Wei PK. J Nanobiotechnol 2010;8:33.
Wang CL, Hsao BJ, Lai SF, Chen WC, Chen HH, Chen YY, et al. Nanotechnology 2011;22:065605.
Yang YC, Wang CH, Hwu YK, Je JH. Mater Chem Phys 2006;100:72.
Yang Y, Yan Y, Wang W, Li JR. Nanotechnology 2008;19:175603.
Zhang SL, Li J, Lykotrafitis G, Bao G, Suresh S. Adv Mater 2009a;21:419.
Zhang XD, Guo ML, Wu HY, Sun YM, Ding YQ, Feng X, et al. Int J Nanomed 2009b;4:165.
Zheng J, Petty JT, Dickson RM. J Am Chem Soc 2003;125:7780.
Zheng J, Nicovich PR, Dickson RM. Annu Rev Phys Chem 2007;58:409.

Publication No. 4 (Participation)

Foreword

In this paper, we present a work on structural biology, using FTIR imaging to characterize collagen structure changes in glioma development. The methodology developed here also is valuable for studying CKD as fibrotic tissue, a main issue in most of renal diseases, developed along CKD physiopathology. Participating in this study with PhD students in charge of this project, it was further decided to conduct a study on CKD models to import FTIR imaging to Taiwan. Currently, Taiwan does not have a large community of spectroscopists, and FTIR imaging is poorly developed (not even present at Academia Sinica in Taipei). To strengthen the collaboration between Bordeaux and Taipei, which would take the form of an International Associated Laboratory in 2016, it was decided to have PhD level training on using FTIR imaging for analyzing glomeruli system in kidney with a 3D chemical imaging perspective.

Title: FTIR spectro-imaging of collagen scaffold formation during glioma tumor development

FTIR imaging is demonstrated to be a useful diagnostic tool for characterizing histopathological change of diseased tissue specimens in biomedical research. In the development of glioma, it is revealed that ECM abnormality is associated with the tumor growth via its physical and chemical effect on microenvironment. Collagen is one of the major components of ECM, which is rarely detected in normal brain tissue. In this study, it has been found that the differences between glioma and healthy brain specimens can be discriminated based on the spectral characteristics of collagen molecules. The spectral difference of secondary structure of protein on Amide I region (1700-1600 cm^{-1}) shows that collagen content is a unique chemical parameter for differentiating brain tumor. The scaffolding level of collagen is found to be related with the progression level of glioma. IR spectral imaging revealed the significant observation on the change of collagen amount and folding architecture. By FTIR imaging analysis on glioma specimens, chemical change (type, amount and molecular structure) of collagens can be used to classify the types of glioma and the tumor development. This finding confirms the significant application of FTIR spectral imaging in diagnosis and prognosis via the characterization of collagen in brain tissue.

In this work, it was found that the change on spectral intensity of Amide I and II region was distinguishable in tumor tissue compared to healthy tissue. On the contrary, lipid content remained stable over the period of tumor growth. Spectral curve fitting process is performed to discriminate the secondary structure change of protein contents between tumor and healthy tissue, revealing that the enlarged bands with the frequency center of 1637 cm^{-1} corresponding to the triplex structure of collagen. With the evidence of statistical result of CFA test on the secondary structure of collagen, it was found that the spectral difference between different types of pure collagens can be discriminated successfully. The same data treatment was successfully applied on the discrimination of tumor progression of solid

glioma based on the spectral information of secondary structure of collagen. Based on the findings of micro-organization of collagen contents by FTIR spectral imaging, it is concluded that collagen differentiation during tumor growth may be considered as a marker of glioma grade.

Work description

The approach of this project is to analyze glioma tumor development by IR chemical imaging, through characterizing the molecular contents related to glioma development for diagnosis. We use nanoparticles as contrast agents to reveal tumor vessels and thus locate the tumor region without histology labeling (such as fluorescent dye). Before launching IR data acquisition on tissue specimens, the sample preparation for IR imaging is to cut the frozen mouse brain perfused with contrast agents to thin sections of 20 μm deposited on the IR transparent substrate. Serial section of mouse brain is performed to obtain consecutive three tissue sections of tumor part in each mouse brain to expand the spectral data collection in tumor volume.

Learning how to collect FTIR image with low S/N ratio and reproducible data is the priority of obtaining raw spectral data for further algorithm analysis. For the data processor to examine chemical band information of IR images, we used commercial ready-to-use software, Opus 7.1, to perform the post data processing on IR data. Fixed band information of pure product collagens is obtained by curve fitting Opus software for the setup of band parameter reference to run the curve fitting on glioma tissue. The work of performing curve fitting on pure product collagens provided a good training opportunity to learn the advanced algorithm, which characterizes individual bands at a spectral interval. In my project of chronic renal disease, curve fitting processing coded by our team members provided the important information on chemical content change of F.A.C sub-molecules at glomerulus level and its

microenvironment. These results showed that fitting procedure on the analysis of FTIR image data is a key step of data processing.

Anal Bioanal Chem (2013) 405:8729–8736
DOI 10.1007/s00216-013-7337-8

RESEARCH PAPER

FTIR spectro-imaging of collagen scaffold formation during glioma tumor development

Razia Noreen · Chia-Chi Chien · Hsiang-Hsin Chen · Vladimir Bobroff · Michel Moenner · Sophie Javerzat · Yeukuang Hwu · Cyril Petibois

Received: 6 June 2013 / Revised: 29 August 2013 / Accepted: 31 August 2013 / Published online: 26 September 2013

Abstract Evidence has recently emerged that solid and diffuse tumors produce a specific extracellular matrix (ECM) for division and diffusion, also developing a specific interface with microvasculature. This ECM is mainly composed of collagens and their scaffolding appears to drive tumor growth. Although collagens are not easily analyzable by UV-fluorescence means, FTIR imaging has appeared as a valuable tool to characterize collagen contents in tissues, specially the brain, where ECM is normally devoid of collagen proteins. Here, we used FTIR imaging to characterize collagen content changes in growing glioma tumors. We could determine that C6-derived solid tumors presented high content of triple helix after 8–11 days of growth (typical of collagen fibrils formation; 8/8 tumor samples; 91 % of total variance), and further turned to larger α-helix (days 12–15; 9/10 of tumors; 94 % of variance) and β-turns (day 18–21; 7/8 tumors; 97 % of variance) contents, which suggest the incorporation of non-fibrillar collagen types in ECM, a sign of more and more organized collagen scaffold along tumor progression. The growth of tumors was also associated to the level of collagen produced ($P<0.05$). This study thus confirms that collagen scaffolding is a major event accompanying the angiogenic shift and faster tumor growth in solid glioma phenotypes.

Keywords Collagens · FTIR imaging · Glioma tumor growth · Solid tumor phenotype

Published in the topical collection *Morpho-Spectral Imaging* with guest editors Cyril Petibois and Yeukuang Hwu.

R. Noreen
Department of Chemistry, Government College University, 38000 Faisalabad, Pakistan

C.-C. Chien · Y. Hwu
Academia Sinica, NANO-X Laboratory, No 128, Sec. 1, Academia Rd. Nankang, Taipei 115-29, Taiwan, Republic of China

H.-H. Chen · V. Bobroff · S. Javerzat · C. Petibois (✉)
Inserm U1029 LAMC, Avenue des facultés, University of Bordeaux, Bat B2, 33405 Talence, France
e-mail: cyril.petibois@u-bordeaux2.fr

M. Moenner
Institut de Biochimie et Génétique Cellulaires, CNRS UMR5095, University of Bordeaux, 1, rue Camille Saint Saëns, CS 61390, 33077 Bordeaux Cedex, France

Introduction

According to the World Health Organization (WHO), glioma can be divided in to four grades (I–IV) with increasing malignancy and invasiveness [1, 2]. Although tumors of all three grades are invasive and highly proliferative but higher grade gliomas, i.e. grade III and IV or glioblastoma multiformes (GBM), are the most common and aggressive primary brain tumors which are also characterized by a high rate of local recurrence due to highly heterogeneous and intrinsically radioresistant tumor cell clones [1, 3]. However, despite advances in neurosurgery, it remains difficult to completely remove the glioma tumors due to the lack of defined tumor areas which is also a reason of poor prognosis [1].

Collagens are the basic component of tumor cell extracellular matrix (ECM) and abnormal production of various collagen types has been reported in CNS tumors like gliomas [4, 5], medulloblastomas, and fibrous tumors of the meninges [6]. In gliomas, the development of extensive microvascular network is associated with a large increase in basement membrane components such as laminin, collagen IV, and fibronectin [7]. This appears consistent with the known roles of collagens in key steps (adhesion, motility, and angiogenesis) of tumor progression. As compared to normal neural cells, glioma cells naturally have the ability to secrete a group of specific proteins in the brain that are not expressed in the ECM of the neural parenchyma, such as type-I laminin, fibronectin, and variable

amounts of collagens type I, III, IV, and VI [8–10]. These ECM collagen contents are also considered as key elements for tumor growth and invasion [11] for the solid and diffuse phenotypes involved in glioblastoma multiform in humans [12]. Collagens scaffolding is also possibly a key driver in the progression of low-grade glioma tumors towards the malignant and high-grade tumors [11].

It is therefore mandatory for anatomo-pathology to characterize the contents in collagens for determining the scaffolding level developed by tumor cells. Conventional histological and microscopic techniques (electron microscopy, fluorescence, and biphotonic microscopy) [13] have been used for the analysis of collagens but provide information only about their organization and remain unable to differentiate which types are present in a tissue sample. These techniques also depend on fluorescence probes, specific labeling, and staining procedures, and cannot determine more than one/two collagen types at a time. These limitations have pushed analytical chemists and biochemists to use vibrational spectroscopic techniques, such as FTIR and Raman spectro-imaging, as alternatives to UV-fluorescence-based histological techniques. FTIR spectro-imaging is based upon the absorption of IR radiation by vibrational transition in covalent bonds of biomolecules present [14]. The IR spectrum thus reflects the contribution of proteins, lipids, carbohydrates, and nucleic acids, plus a lot of other molecules in low concentration [15]. Several studies have reported the application of FTIR spectro-imaging for analysis of normal and pathological brain tissues based on molecular contents [3, 16, 17] and also used in other cancer tissues from liver, stomach [18], cervix [19], breast [20], colon [21, 22], prostrate [23], lungs [24], and skin [25, 26]. Furthermore, FTIR imaging is now proposed for the pathological examination of glioma tumors [27, 28] (their grades, histological classification according to WHO grading system [15, 17, 29]) and could also reveal the tumor margins after surgical resection for high-grade gliomas [27]. However, this technique is not used as a routine pathological analysis in hospitals due to the lack of molecular information provided by the multivariate classification methods [30, 31]. Thus, the application of FTIR spectro-imaging must be developed in this direction, where statistical data treatment methods must provide the molecular information of molecules. Previously, we have demonstrated that this technique allows the differentiation of collagen types [14] in the connective tissues and glioma tumors based on their secondary structure parameters by using the spectral curve-fitting methods and these contents could also be determined in the connective tissue of skeletal muscle [32], glioma tumor vasculature [3], and solid and diffuse glioma tumor tissues [33]. In this study, we demonstrate the usefulness of FTIR spectro-imaging for discriminating different steps of glioma tumor growth based on ECM production by tumor cells. Our objective was to demonstrate that FTIR imaging could also be a useful tool for determining the grades of glioma tumors and should be further developed for anatomo-pathological examination purposes.

Materials and methods

Animals

Six-week-old male Rag-gamma immuno-deficient mice ($n=26$) with an average weight of 24 g were used for this study. Animals were anesthetized using Imalgene 1000 (ketamine 10 g/100 ml) injected intraperitoneally. C6 rat glioma cells (5×10^5 cells per animal) were suspended in 3 μl of medium and implanted subcutaneously into the flanks (the outer part of the thigh) of mice. Full brain (with xenografted tumor on one lobe and healthy brain on the other lobe) were removed from mice after 8–11 ($n=8$), 12–15 ($n=10$), and 17–21 ($n=8$) days of post-implantation growth of tumors. Tumor volume was estimated for every tumor from a series of histological sections on the full course of tumor volume. All samples were washed in PBS solution and placed in tubes without fixatives before freezing in liquid N_2 and stored at −80 °C until measurements.

Tissue samples

For every sample, frozen tissue was deposited on cooled glue (polyvinyl alcohol for cryostat, −20 °C) to avoid tissue embedding. Additional glue was used to homogenize the sample in a block intended for cryosections (Cryostat 3050-TM, Leica Microsystems, France). Orientation of tissue deposited on support allowed sectioning frontally the two brain lobes for comparison between healthy (right lobe) and tumor (left lobe) tissues. Serial frozen sections of 20 μm in thickness (three sections per tumor) were transferred onto ZnSe windows for FTIR spectral imaging. All tissue sections were dried on air before further processing. Three tissue sections per sample were used for statistical data treatments.

FTIR spectral imaging acquisition

Tumor tissue sections were analyzed by FTIR imaging using Hyperion 3000 spectral imaging system equipped with a Tensor 27 spectrometer (Bruker-Optics, France) with a liquid-N_2 cooled focal plane array (64×64 elements 40×40 μm each) detector and a Globar source. A ×15 magnification level and condenser were used for obtaining a final FTIR image with pixels dimension of 2.6×2.6 μm, thus at $\sim\lambda/2$ for the mid-IR spectral interval. All infrared images were obtained in transmission mode from the tumor sections in the 4,000–900 cm^{-1} range by using 300 scans with spectral resolution of 8 cm^{-1}. Once the visible image was obtained, two tissue areas were selected—one corresponding to the

tumor volume and another one in the contralateral lobe corresponding to the healthy tissue (about 1 mm^2 for every tissue area). All data acquisition, post-processing (atmospheric CO_2 and baseline corrections), and image construction were performed using rubber band corrections with 64 points method by sub-routines of the Opus 7.1 software (Bruker-Optics, France).

Spectral curve fitting

FTIR spectra corresponding to every FTIR image of tumor and healthy tissue were averaged and saved for further data treatments. Curve-fitting of collagens FTIR spectra was performed with a sub routine of Opus 6.5 software (Bruker, France). Pure product spectra for types I, III, IV, V, and VI collagens have been used as references for comparison with tissues as previously described [14, 32–34]. The secondary structure of collagen proteins were determined by using the spectral curve fitting of amide I region (1,720–1,480 cm^{-1}). To avoid some confounding effects of self curve-fitting, where absorption band positions may vary a lot, absorption bands were fixed (their position) for all FTIR spectra according to previous studies [14, 35–37]. The percentage of Gaussian and Lorentzian functions for every absorption band was first determined from the series of pure product spectra of collagen. Eight absorption bands of amides I were selected in the 1,720–1,600 cm^{-1} spectral interval of FTIR spectra according to literature [32, 36, 38–43] (secondary structure calculations were performed using eight selected bands of amide I spectral interval as follows: α-helix (1,658 cm^{-1}), β-sheets (1,691, 1,679, and 1,626 cm^{-1}), β-turns (1,669 and 1,610 cm^{-1}), triple helix (1,637 cm^{-1}) and unordered structure (1,647 cm^{-1}) [14, 32, 44, 45]). All bands were positioned at maximal intensities and shape parameters were set at 90/10 % of Gaussian/Lorentz functions, respectively. Free parameters (free bands) in fitting procedure were also added at 1,750 and 1,480 cm^{-1} to avoid anomalous band additions at the limits of the spectral interval. All absorption bands were determined using the same fixed parameters. The results were expressed as percentages for each secondary structure parameter with respect to the total amide I spectral interval absorption (1,700–1,480 cm^{-1}).

Statistics

All results were expressed as mean±SE. Comparison between healthy and tumor tissues (8–11, 12–15, and 18–21 days) were performed with multivariate analysis of variance (MANOVA; SPSS 15.0, SPSS Inc., France) applied on the results obtained from the spectral curve fitting of every spectral interval. All data obtained from amide I absorption bands and secondary structure parameters were used for the comparison between tumors and healthy brain tissue. Multiple comparisons were performed using Dunnett's T_3 Post Hoc analysis for the determination of significant difference between these groups for each absorption band. Dunnett's test analysis is commonly used when ANOVA has rejected the hypothesis of the equality of the means distributions. It compares group means and is specially designed for the situations where all group means are to be checked against one reference group. Its purpose is to identify the groups whose means are significantly different from the means of this reference group. P values were fixed at 0.05 and 0.01 to consider the significant level of difference between series of data. Multivariate correspondence factor analysis (CFA, XL-stat, 2009) was used for the classification of all groups (collagens, healthy tissue, and tumor tissues) according to their secondary structure parameters. Here, we use collagen spectra models that we compare to brain tissue samples. This approach is considered valid since brain tissue is almost devoid of collagen contents while tumor tissue is characterized by huge production of collagen by invading and dividing cells. Thus, the brain tumor analysis magnifies the collagen content differences between healthy and tumor tissues. This is facilitating a collagen-based characterization of brain tumors, which can be more difficult for other organs. CFA is another multivariate technique which measure the correspondence between subjects (models+test samples) and variables (secondary structure parameters in our case). It is capable to give simultaneous representation of samples and variables in the same factorial analysis at the same graph and make it easy to understand the complicated information in the data tables, which is not achieved by principle component analysis (PCA) and in other classification methods [46–48].

Results

FTIR imaging of brain tissues

An example of visible and FTIR images of brain tissue sections are presented in Fig. 1.

FTIR spectra ($n=50$) were randomly extracted from selected area corresponding to each healthy and tumor tissues by excluding the blood capillaries (Fig. 2). All samples showed absorption in amide I and amide II regions which are mainly related to the stretching vibrations of C=O bonds, and combination of C–N stretching and N–H bending vibrations, respectively. Healthy tissues showed more intense lipid absorption (3,050–2,800 cm^{-1}) as compared to tumors, but these parameters remained stable over time (2,921 cm^{-1} absorption was 0.35±0.11 vs. 0.36±0.12 vs. 0.30±0.13 a.u.; 8–11 vs. 12–15 vs. 18–21 days, respectively; $P>0.05$ for all comparisons). Amide I absorption intensity (1,654 cm^{-1}) was also found stable over time in healthy samples (0.61±0.12 vs. 0.63± 0.14 vs.0.58±0.11 a.u., respectively). On the other hand, tumor samples presented higher contents in proteins ($P<0.01$) and lower lipid contents ($P<0.01$) than healthy samples for all

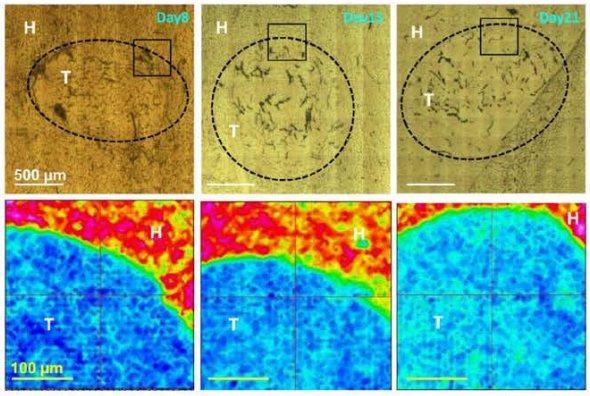

Fig. 1 Examples of visible and FTIR images of brain tissue sections (20-µm thickness). Solid glioma tumors derived from C6 cells implanted in mice brain and analyzed after 8 (*left image*), 15 (*center*) and 21 days (*right image*) of tumor growth, respectively. *H* healthy "nontumor" tissue area; *T* tumor tissue area. FTIR images show the lipid-to-protein ratio (1,700–1,600/3,000–2,800 cm^{-1} spectral intervals), which magnifies the highest protein contents and lowest lipid contents of tumor with respect to nontumor tissue. Delimitations between healthy and tumor tissue areas are given for better readability of images only

growth periods. Lipid contents remained stable in tumors (~0.2 0.25 a.u.) over time while protein contents first increased (days 8 11 vs. days 12 15) and further decreased at days 18 21 (0.68±0.09 vs. 0.78±0.12 vs. 0.63±0.11 a.u., respectively; $P<0.05$).

Spectral curve fitting of amides spectral region

To analyze secondary structure parameters of proteins, amide I band absorptions were determined by curve fitting the 1,720 1,480 cm^{-1} spectral interval (Fig. 3). All absorption bands could be determined on every spectrum ($n=50$) for each sample ($n=26$) with a maximum 2-cm^{-1} free shift at maximal intensities by using a subroutine of OPUS 7.1 software. The curve-fitting procedure was run until the root mean square error (RMSE) value gets lower than 1 %. It was observed that FTIR spectra of healthy tissues showed almost negligible intensity or very low intensity for triple helix absorption band over time (1,637 cm^{-1}; 0.05±0.03 vs. 0.0.4±0.02 vs. 0.06± 0.05 a.u.; 8 11 vs. 12 15 vs. 18 21 days, respectively; $P>0.05$ for all comparisons). On the contrary, tumor tissue showed significantly higher intensity of this absorption band (0.29±0.09 vs. 0.41±0.07 vs. 0.33±0.08 a.u.; 8 11 vs. 12 15 ($P<0.01$) vs. 18 21 days ($P<0.01$), respectively; and $P<0.01$ for all comparisons with healthy tissue conditions), and it was found increased between days 8 11 and days 12 15, while it slightly but significantly decreased thereafter.

Table 1 shows details on secondary structure parameters for healthy and tumor tissues at the three different periods of experiments. They confirm that triple helix content was higher in tumor tissues at all periods ($P<0.01$) while α-helix content was conversely higher in healthy tissues ($P<0.01$)

Characterization of collagen contents in brain tissues

The second objective of this study was to discriminate the different stages of tumor growth based on their collagen contents formation determined by their secondary structure

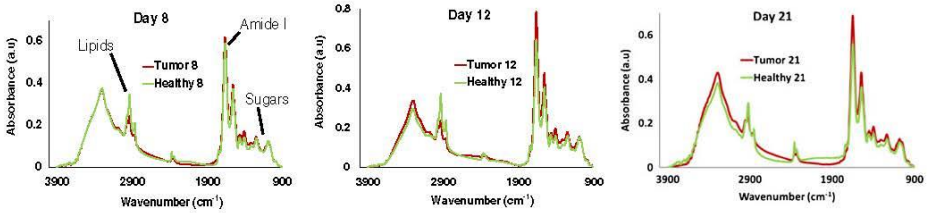

Fig. 2 Mean FTIR spectra (4,000–900 cm^{-1}) extracted from healthy and tumor images obtained after 8–11 days (*left*), 12–15 days (*center*) and 18–21 days (*right*). $n=400$ spectra per condition

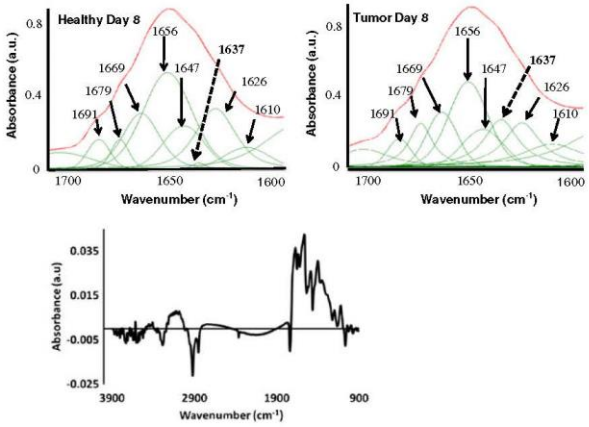

Fig. 3 Spectral curve fitting of amide I region (1,720–1,600 cm^{-1}) of healthy (*left*) and tumor (*right*) tissue at days 8–11. The 1,637 cm^{-1} absorption band is used as direct evidence of collagens presence in tissue samples. Difference FTIR spectrum (tumor-healthy conditions) corresponding to curve-fitted spectra is presented to show the changes in molecular contents. A reduced lipidic content (3,050–2,800 cm^{-1} spectral interval) is observed while proteins (1,700–1,500 cm^{-1}) and saccharides (1,150–950 cm^{-1}) are increased in the tumor condition

parameters. For this purpose, we first compared the distribution of collagens (pure product spectra) vs. their secondary structure profiles by using CFA test (Fig. 4).

CFA test provides the representation of results under graphical form with correlated samples grouped according to their "variables profiles" proximity and also showed optimizing distance between groups. It allows the construction of orthogonal system of axis called factors (F1, F2…, etc.) with statistical spaces per factor (Fig. 4, left). Here, we explained the interpretation of this test by taking an example of our reference model. There is one statistical space of correlation at the right side of the F1 axis and second space of correlation at the left side of the F1 axis with a statistical weight of 91.24 % (Fig. 4, left). These two spaces are opposite to each other. We can consider this same distribution of two spaces for the F2 axis (upper and lower side of axis) if the statistical weight is more than 10 % in our results. For the interpretation of results, one can consider that the model and test samples were found correlated (same side of the statistical space/factor) or excluded (opposite sides/factors).

This first step of spectral data treatment was performed to evaluate the efficiency of CFA test which was also explained previously. More briefly, the CFA plot with 91.24 % of statistical weight at F1 axis revealed the proximity of fibrillar collagens (types 1, 3, and 5) with α-helix, β-turns, and triple helix which were situated at the left side of F1 axis (Fig. 5, left). Whereas non-fibrillar collagens (type 4 and 6) showed their proximity with β-sheets and unordered structures presented at the right side of the F1 axis. In this model, we did not consider

Table 1 Secondary structure parameters of brain tissue protein contents

Samples	α-helix	Triple helix	β-sheets	β-turns	Unordered
Tumor-D8	24.1 ± 1.3^{bdef}	15.7 ± 1.0^{bcdef}	27.4 ± 1.4^{bcd}	22.8 ± 1.6^{bc}	9.1 ± 0.5^{bcdef}
Tumor-D12	26.1 ± 1.7^{adef}	13.3 ± 0.7^{acdef}	25.8 ± 1.4^{ade}	24.8 ± 1.9^{ade}	10.1 ± 0.4^{ace}
Tumor-D21	25.3 ± 1.9^{def}	10.9 ± 0.4^{abdef}	26.0 ± 1.9^{ade}	25.8 ± 1.4^{ade}	12.7 ± 0.7^{bde}
Healthy-D8	35.6 ± 3.5^{abc}	0.5 ± 0.1^{abc}	29.2 ± 1.4^{abc}	23.2 ± 2.3^{bc}	11.5 ± 1.2^{abc}
Healthy-D12	35.5 ± 1.9^{abc}	0.5 ± 0.1^{abcf}	28.8 ± 1.4^{bc}	22.7 ± 2.3^{bc}	12.5 ± 1.2^{abc}
Healthy-D21	35.9 ± 2.7^{abc}	0.6 ± 0.1^{abce}	30.4 ± 2.9	22.7 ± 5.2	10.4 ± 0.3^{ae}

All values are mean±SD of spectral integration results obtained from amide I spectral interval curve fitting (1,700–1,600 cm^{-1}). $n=10$ samples per condition and 50 spectra per sample randomly selected on tissue areas

D days

[a] Significantly different from Tumor-D8

[b] Significantly different from diffuse Tumor-D12

[c] Significantly different from Tumor-D21

[d] Significantly different from Healthy-D8

[e] Significantly different from Healthy-D12

[f] Significantly different from Healthy-D21 at 0.05 level of significance ($P<0.05$)

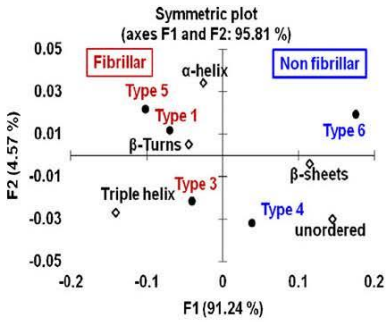

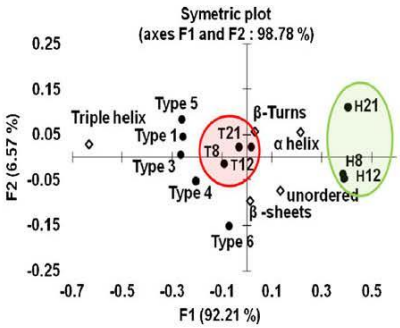

Fig. 4 Symmetric CFA score plot of collagens distribution based on their secondary structure profiles (*left*). Fibrillar collagens (*types 1, 3, and 5*) show proximity with β-turns, triple helix and α-helix contents. Non-fibrillar collagens (*types 4 and 6*) shows proximity with β-sheets and unordered structures (*left*). Symmetric score plot of CFA showing the distribution of the five collagens types which was followed by the addition of spectra from healthy and tumor tissues for their comparison with collagen contents (*right*). *Red circle* clearly showed the proximity of tumors with collagens types and triple helix; *green solid circle* shows distribution of healthy tissue far from triple and also opposite to collagens

the F2 axis because the statistical variance or statistical weight was too low (<10 %). We observed that this statistical test is able to show a difference between fibrillar and non-fibrillar collagens based on their secondary structure profiles and showed the graphical representation of all data (collagen types and secondary structure profiles) on the same symmetric plot which was not attained by other statistical tests such as PCA, factorial analysis, discriminate analysis, etc. So this model was used for further analysis and in the next step, averaged FTIR spectra from healthy and tumor tissues (days 8 11, 12 15, and 18 21) were included in the database.

The distribution of samples vs. collagen types on the CFA symmetric plot showed that the healthy tissues are plotted at the right side of the F1 axis close to the unordered structures and at largest distance from the triple helix parameter and collagens types which were at the left side of F1 axis (Fig. 4, right). Conversely, tumor tissues were situated near the collagen contents at the left side of the F1 axis. This statistical exclusion between triple helix and healthy tissue samples exhibited the low or almost no collagen contents in the healthy tissues which is in agreement with the absence of collagens in ECM of healthy brain tissues [9, 49].

Further, we removed healthy tissues from this comparison and the same CFA test was performed only for tumor tissues vs. types of collagens (Fig. 5, right). As previously described [33], it allows analyzing the tumor tissues only for distribution according to collagen types

It was found that only first-period tumors (days 8 11) were close to triple helix and fibrillar types of collagens according to F1 axis (68 % of variance), while longer period tumors (days 12 15 and 18 21) could be found on the same side of triple helix and fibrillar collagens only according to the F2

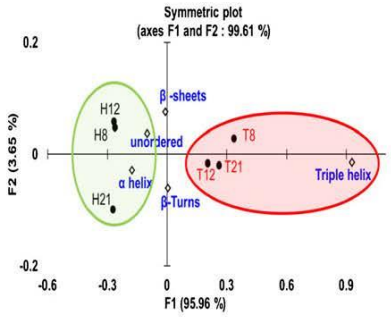

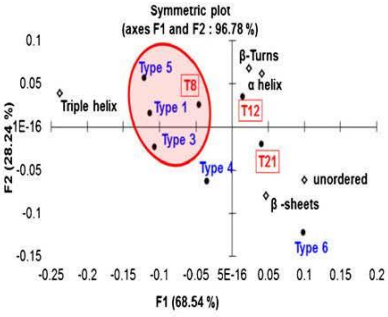

Fig. 5 Symmetric score plot of CFA test showing the distribution of healthy and tumor tissue samples according to secondary structure parameters (*left*), and distribution of only tumor samples with five collagen types (*right*). *H* healthy tissue; *T* Tumor tissue for 8–11 (*T8*), 12–15 (*T12*), and 18–21 (*T21*) days

axis, which accounted for 28 % of variance (thus considered as significantly descriptive of samples).

Discussion

Collagens are now considered as the most important self-sustaining 3D scaffold contents in glioma tumors, facilitating cell division, migration, and proliferation at early stages of tumor development [11]. However, little is known about the network organization and typology of these collagens, thus limiting our capacity to target specifically the protein types involved. Following the previous studies on collagen contents discrimination between solid and diffuse models of gliomas [33, 34], our aim was to demonstrate that FTIR imaging could also be a useful tool for determining the grade of such tumors. The statistical tests performed on curve-fitting parameters of spectra representative of healthy and tumor tissue areas showed that secondary structure parameters of protein contents in tumor tissues were significantly different from those of healthy tissues, even at early stage (days 8–11) of tumor growth. Noticeably, much higher triple helix content was found in tumors, showing that collagen is produced at all stages of tumor development as a bed for cellular organization [7, 34, 50]. Conversely, higher α-helix content characterized healthy tissues with very weak triple helix absorption, thus confirming that almost no collagen was present.

These differences between healthy and tumor tissues could also be observed in the sample distribution of CFA plot. Tumor tissues exhibited proximity with triple helix parameter where healthy tissues were found closer to unordered structure and α-helix parameters. The same plot considering only tumor tissues vs. secondary structure parameters showed that tumor tissues protein contents evolved with tumor growth. At days 8–11, tumor tissue protein contents were found very close to triple helix parameter, thus suggesting that tumor cells produced primarily collagens in the first days of tumor growth and organization. At days 12–15, tumor tissue protein contents were found closer to triple helix and α-helix parameter while at days 18–21, better proximity to β-turns was observed, thus suggesting a modification of proteins production by tumor cells along with tumor development. Taken together, these changes in protein secondary structure parameters suggest a shift from collagen production towards more glomerular proteins (presenting higher contents of β-sheets) or from highly fibrillar collagen types (with high contents of triple helix and α-helix) towards more glomerular types (presenting higher contents of α-helix and β-sheets). To test such hypothesis on collagens, we compared tumor and healthy tissue protein contents (secondary structure parameters) with collagen types I, III, IV, V, and VI. A first verification was that secondary structure parameters of fibrillar types (I, III, and V) were found close to triple helix and α-helix components. Conversely, types IV and VI were found closer to β-sheet and β-turns components. This demonstrates that the multivariate statistical approach of CFA is sensitive enough to classify correctly the collagen types with respect to their secondary structure parameters. A further analysis was the inclusion of healthy and tumor tissue parameters for the three different periods of tumor growth. It was found that healthy tissue samples were classified in CFA plot far from triple helix parameters and opposite to tumor tissues. This confirms previous studies performed while using both solid and diffuse forms of glioma tumors [33]. Here, the goal was to determine the changes in collagen contents along tumor growth. It was found that early-stage tumors exhibited higher contents in fibrillar collagens (types I and III notably at days 8–11), but this was followed by a shift towards type IV and VI collagens on days 12–15 and even more pronounced at days 18–21. The total variance of CFA plot on F1 and F2 axes was ~97 %, thus confirming that collagen contents in tumors was highly relevant for such multivariate classification. We can thus hypothesize that collagen differentiation over time from fibrillar to non-fibrillar types is a major structural feature of tumor growth in solid phenotypes of glioma.

Conclusion

We have demonstrated that collagen scaffolding and typology differentiation along glioma tumor growth is a major structural event driving their progression. Importantly, early stages of tumor growth were mainly supported by a dense fibrillar-type scaffold of collagens, which is probably the prerequisite for first cellular organization as a functional tissue with respect to host environment. The later stage of tumor growth show more differentiated typology of collagens, thus suggesting very organized scaffolding mediated by the inclusion of non-fibrillar species. This demonstrates that there is no anarchy in the ECM formation in glioma tumors. FTIR imaging also confirms this eminent role in the analysis and characterization of collagens in tissues, thus providing even more evidence that it can play a significant role as an anatomo-pathological tool in clinics and for biological research purposes [51].

Acknowledgments The authors are indebted to the "Ligue Nationale contre le cancer" and the "Agence Nationale de la Recherche" (ANR contract no bl-inter09_464249-MIAG-X) for their financial support.

References

1. Beauchesne P (2011) Cancers 3:461–477
2. Gladson CL, Prayson RA, Liu WM (2010) Annu Rev Pathol 5:33–50
3. Wehbe K, Pinneau R, Moenner M, Deleris G, Petibois C (2008) Anal Bioanal Chem 392:129–135

4. Kavsan VM, Dimitrenko VV, Shostak KO, Bukreieva TV, Vitak NY, Simirenko OE, Malisheva TA, Shamayev MI, Rozumenko VD, Zozulya YA (2007) Cyt Genet 41:30–48
5. Liang Y, Diehn M, Bollen AW, Israel MA, Gupta N (2008) J Neurooncol 86:133–141
6. Nitta H, Yamashima T, Yamashita J, Kubota T (1990) Histol Histopathol 5:267–274
7. Huijbers IJ, Iravani M, Popov S, Robertson D, Al-Sarraj S, Jones C, Isacke CM (2010) PLoS One 5:e9808
8. Gladson CL (1999) J Neuropathol Exp Neurol 58:1029–1040
9. Bellail AC, Hunter SB, Brat DJ, Tan C, Van Meir EG (2004) Int J Biochem Cell Biol 36:1046–1069
10. Tso CL, Shintaku P, Chen J, Liu Q, Liu J, Chen Z, Yoshimoto K, Mischel PS, Cloughesy TF, Liau LM, Nelson SF (2006) Mol Cancer Res 4:607–619
11. Samuel MS, Lopez JI, McGhee EJ, Croft DR, Strachan D, Timpson P, Munro J, Schroder E, Zhou J, Brunton VG, Barker N, Clevers H, Sansom OJ, Anderson KI, Weaver VM, Olson MF (2011) Cancer Cell 19:776–791
12. D'Abaco GM, Kaye AH (2007) J Clin Neurosci 14:1041–1048
13. Gutsmann T, Fantner GE, Kindt JH, Venturoni M, Danielsen S, Hansma PK (2004) Biophys J 86:3186–3193
14. Belbachir K, Noreen R, Gouspillou G, Petibois C (2009) Anal Bioanal Chem 395:829–837
15. Steiner G, Shaw A, Choo-Smith LP, Abuid MH, Schackert G, Sobottka S, Steller W, Salzer R, Mantsch HH (2003) Biopolymers 72:464–471
16. Petibois C, Drogat B, Bikfalvi A, Deleris G, Moenner M (2007) FEBS Lett 581:5469–5474
17. Krafft C, Sobottka SB, Geiger KD, Schackert G, Salzer R (2007) Anal Bioanal Chem 387:1669–1677
18. Wang TD, Triadafilopoulos G, Crawford JM, Dixon LR, Bhandari T, Sahbaie P, Friedland S, Soetikno R, Contag CH (2007) Proc Natl Acad Sci U S A 104:15864–15869
19. Cohenford MA, Rigas B (1998) Proc Natl Acad Sci U S A 95:15327–15332
20. Fabian H, Thi NA, Eiden M, Lasch P, Schmitt J, Naumann D (2006) Biochim Biophys Acta 1758:874–882
21. Lasch P, Haensch W, Naumann D, Diem M (2004) Biochim Biophys Acta 1688:176–186
22. Salman A, Sahu RK, Bernshtain E, Zelig U, Goldstein J, Walfisch S, Argov S, Mordechai S (2004) Vib Spectrosc 34:301–308
23. Li MJ, Hsu HS, Liang RC, Lin SY (2002) Ultrastruct Pathol 26:365–370
24. Yano K, Ohoshima S, Gotou Y, Kumaido K, Moriguchi T, Katayama H (2000) Anal Biochem 287:218–225
25. Crupi V, De Domenico D, Interdonato S, Majolino D, Maisano G, Migliardo P, Venuti V (2001) J Mol Struct 563–4:115–118
26. Zhang G, Moore DJ, Flash CR, Mendelsohn R (2007) Anal Bioanal Chem 387:1591–1599
27. Sobottka SB, Geiger KD, Salzer R, Schackert G, Krafft C (2009) Anal Bioanal Chem 393:187–195
28. Gaigneaux A, Decaestecker C, Camby I, Mijatovic T, Kiss R, Ruysschaert JM, Goormaghtigh E (2004) Exp Cell Res 297:294–301
29. Beljebbar A, Amharref N, Leveques A, Dukic S, Venteo L, Schneider L, Pluot M, Manfait M (2008) Anal Chem 80:8406–8415
30. Petibois C, Deleris G, Piccinini M, Cestelli Guidi M, Marcelli A (2009) Nat Photonics 3:179
31. Petibois C, Déléris G (2004) Analyst 129:912–916
32. Petibois C, Gouspillou G, Wehbe K, Delage JP, Deleris G (2006) Anal Bioanal Chem 386:1961–1966
33. Noreen R, Chien CC, Delugin M, Yao S, Pineau R, Hwu Y, Moenner M, Petibois C (2011) Anal Bioanal Chem 401:845–852
34. Noreen R, Moenner M, Hwu Y, Petibois C (2012) Biotechnol Adv 30:1432–1446
35. Fabian H, Lasch P, Naumann D (2005) J Biomed Opt 10:031103
36. Goormaghtigh E, Ruysschaert JM, Raussens V (2006) Biophys J 90: 2946–2957
37. Sun WY, Fang JL, Cheng M, Xia PY, Tang WX (1997) Biopolymers 42:297–303
38. Ami D, Neri T, Natalello A, Mereghetti P, Doglia SM, Zanoni M, Zuccotti M, Garagna S, Redi CA (2008) Biochim Biophys Acta 1783:98–106
39. Fabian H, Naumann D (2004) Methods 34:28–40
40. Petibois C, Déléris G (2006) Trends Biotechnol 24:455–462
41. Haris PI, Servecan F (1999) J Mol Catalysis B: Enzymatic 7:207–221
42. Muyonga JH, Cole CGB, Duodu KG (2004) Food Chem 86: 325–332
43. Ngarize S, Herman H, Adams A, Howell N (2004) J Agric Food Chem 52:6470–6477
44. Goormaghtigh E, Raussens V, Ruysschaert JM (1999) Biochim Biophys Acta 1422:105–185
45. Troullier A, Reinstadler D, Dupont Y, Naumann D, Forge V (2000) Nat Struct Biol 7:78–86
46. Doré J-C, Ojasoo T, Okubo Y, Durand T, Dudognon G, Miquel J-F (1996) J Am Soc Inf Sci 47:588–602
47. Kishino H, Waddell PJ (2000) Genome Inform Ser Workshop Genome Inform 11:83–95
48. Teil H (1975) Math Geol 7:3–12
49. Senner V, Ratzinger S, Mertsch S, Grassel S, Paulus W (2008) FEBS Lett 582:3293–3300
50. Aubert M, Badoual M, Christov C, Grammaticos B (2008) J R Soc Interface 5:75–83
51. Petibois C, Cazorla G, Gin H, Deleris G (2001) J Lab Clin Med 137: 184–190

Discussion

The objective of this PhD thesis is to discriminate the chemical parameters and morphological change of the renal functional unit, glomeruli, in the kidney of mice with different levels of CKD in three dimensions. The model of UUO in the rodents, which establishes the CKD condition studied in this thesis, generates a physically induced progressive inflammation in the kidney without the involvement of exogenous toxins as well as avoiding the genetic effect. FTIR imaging is considered as a useful tool to characterize the molecular histology by analyzing the spectral chemical information in many biological samples. Glomerulus has been the research subject in renal studies by many imaging techniques, but this complex microvasculature network has not been effectively studied in chronic disease statuses by FTIR imaging. The continuing decrease of GFR in CKD indicated that the function efficiency of glomeruli is evidently affected in the progression of CKD. Differentiating pathological signatures of disease biosamples by FTIR imaging provides nephrologists a tool to investigate the outcome of multiple-stress factors such as increased oxidative stress, metabolic disorder, and inflammation at the glomerulus level of CKD. Reproducible FTIR data acquisition and multivariate data treatment can provide appropriate chemical based information to distinguish the stage of disease in glomeruli between pathological and contralateral kidneys of the mice with CKD and healthy kidneys coupled with statistical analysis. The characterized absorption information of barium sulfate microparticles perfused in a glomerular vessel is used to visualize glomerular morphology and predict the glomerular damage by estimating barium sulfate content and their distribution in glomeruli. Although the standard pathological information about glomeruli of CKD is lacking in this study as there are no approaches to reach the complex biochemical conclusion of renal pathology. Our study of comparing healthy and pathological glomeruli of CKD can provide the 3D chemical/molecular conclusion of glomeruli on fundamental renal research based on spectral analysis coupled with statistical data treatment. The aim of this PhD thesis project on renal study is to access the histopathological application of 3D FTIR imaging on scientific research and further explore it to the routine use in medicine.

In this study, we research the molecular differences of the glomerulus level of the kidney with CKD based on FTIR imaging. At first, the molecular content based on the intensity of spectral absorption is investigated to evaluate the chemical parameters of lipid and protein in renal specimens. The finding has shown that the ratio of lipid to protein in pathological glomeruli is different to healthy glomeruli. Although the absolute IR absorption of lipid and protein in glomeruli does not reveal significant change between pathological and healthy specimens, the relative expression between two molecular content is sufficient to discriminate the chemical/molecular characteristics of glomeruli. The discussion of metabolic molecules in glomeruli is not studied in this project because of the large overlapping phenomenon of spectral absorption between barium sulfate and the carbohydrates within the 1300–900 cm^{-1} spectral interval. Strong absorption of barium sulfate microparticles masks the weaker spectral information of metabolic factors such as glucose, glycogen, and lactic acid within the tissue. The work on subtracting IR absorption attributable to barium sulfate microparticles in renal specimens is the future subject in researching the metabolic information of CKD in kidney.

Another subject in this project is the investigation of IR absorption change of phospholipids in renal specimens associated with oxidative stress in CKD. The increasing oxidative stress correlated with the severity of renal failure involves the level of lipid peroxidation [169]. We use curve-fitting process based on the spectral interval of 3050-2800 cm^{-1} to perform quantitative analysis of ν(=CH), $\nu_{as}(CH_3)$, and $\nu_{as}(CH_2)$ bands for their characteristic band absorption of fatty acid chains. This performance allows the oxidative damage on lipids to be quantitatively calculated on the basis of the ratio of ν(=CH) to $\nu_{as}(CH_2)$, the unsaturation level of lipids. The change of unsaturated lipids provides a direct measurement of oxidative stress in pathological kidneys with different severities of CKD, its corresponding contralateral kidneys and healthy kidneys of the control mice. Although the global detection of oxidative stress in clinical examination are not currently accessible because of the instability of some ROS of oxidative

stress and their short half-life, the oxidation target end products including peroxidized lipids formed due to the reaction of ROS with biomolecules are more stable as well as detectable in many biosamples with pathological conditions [170].

In the statistical results on the basis of 2D consecutive measurement of IR absorption and further data treatment, the findings were to demonstrate that 3D FTIR imaging is able to reach the stereological spectral discrimination of glomerular and global renal specimens. We found that the percentage of peroxidized lipids in glomerulus is increased in both pathological kidney and contralateral kidney compared to healthy kidney in the progression of CKD. Second, the distribution of perioxidized lipids is different from the pathological kidney to the contralateral kidney of mice with CKD. The distribution pattern of increased peroxidized lipids is increased from periglomerular tissue to glomerular tissue in pathological kidney in the development of CKD, while the opposite happens in a contralateral kidney. Therefore, this study has shown that 3D FTIR imaging is able to distinguish the pathological change between pathological and its contralateral kidney of the mice with CKD as well as between contralateral kidneys of the mice with CKD and healthy kidneys of control mice. We also found that the 3D characterized spectral feature of glomeruli in the 3050-2800 cm^{-1} spectral interval may be a predictable parameter of pathological stress at the early stage of CKD. Combined with the above findings about glomeruli of CKD on chemical parameters, FTIR imaging coupled with stereological analysis is a potential diagnostic tool of determining pathological status of glomeruli related with progressive renal disease.

The last step of this study is to use 3D FTIR imaging data to build the visualization of morphometric information of glomerulus level for the functional discrimination between pathological kidneys and healthy kidneys. We use integrated intensity of IR absorption of barium sulfate perfused in renal microvasculature as the functional parameter to examine glomerular morphology. The chemical

parameter based on the spectral characteristics of C-H stretching region (3050-2800 cm^{-1}) of the specimens is used to co-localize with the morphological parameter generated from barium sulfate intensity for creating the 3D multiparameter FTIR imaging of glomeruli. This 3D plotting of FTIR imaging approach shows the correlation of the internal anatomy of the glomerular vasculature and the molecular information of pathological state of glomeruli. The report on UUO models proposes that the obstruction may cause the microvascular injury based on the observation of thickening epithelial layer of glomeruli [171] as well as the reduction of renal blood flow contributing to the changes in vasculature of the obstructed kidney [172]. In the present study, 3D FTIR imaging has the potential of being a useful tool to quantitatively investigate the 3D vascular morphology and functional parameter of glomerulus level based on one spectral dataset.

The weakness in the present study is in its uncertainty of the relationship between the severity of CKD and the spectral histopathology, although it is highly possible to demonstrate the association between chemical information based on successive spectral dataset and glomerulus unit of the kidney. The small sample size of received biological specimens and minimum number of glomeruli which is completely collected for a successive dataset acquirement in each mouse kidney are the reasons with respect to the confident statistical conclusion. Though the –CH stretching region on 3050-2800 cm^{-1} is used to determine chemical change of glomeruli during the progression of CKD, other spectral interval containing more complex absorption bands such as fingerprint region for Amide absorption is not discussed in this study. On other hand, the lack of specific biomolecular evidence to support histopathological determination is another issue when considering FTIR as a histopathological tool because all spectrometric evaluation of biosamples is based on mathematical computing.

Conclusions & Perspectives

In our study, we used FTIR microscopy developed as a 3D reconstruction imaging method to investigate histopathological change of CKD on the basis of chemical parameters of glomeruli on the spectral interval of –CH stretching region (3050-2800 cm^{-1}). We demonstrated that the 3D quantitative analysis of chemical parameters can be obtained. The methodology developed can be automated so that diagnostic applications can be predicted in a clinical routine. Several key-parameters of renal diseases can be investigated, thus giving sense to the development of routine tools in the future. The spectra information of molecular content and/or the chemical change of fatty acid chains in phospholipids help to distinguish glomerular tissue from non-glomerular tissue, which may be an important capability in disease diagnosis. Using appropriate data treatment on 3D spectral data, we demonstrated that pathological and healthy glomeruli can be effectively discriminated based on the statistical difference on the unsaturated lipid level and spectral characteristics. The glomerular filtration rate can be also determined using appropriate contrast agent, in this case, $BaSO_4$ nanoparticles, which is an accepted chemical for human investigations. It remains to be demonstrated that this imaging agent can be used in pharmacological concentrations in the blood stream for local injections. A biopsy might be sufficient to characterize CKD or other renal pathologies at the glomerulus level, which is currently a missing diagnostic tool.

From this set of works done during my PhD and other initiatives between the involved Bordeaux and Taiwan laboratories, several ambitious projects have emerged to make 3D IR microscopy a major method for analyzing tissue volumes in 3D. From biomedical to pharmacological applications, the technique will provide unprecedented analytical performances for the 3D chemical analysis of tissues, extracting automatically chemical, biochemical, molecular, and sub-structures information from spectral-derived data. In this framework, the IR microscopy methodology for 3D chemical histology can be imported and developed in Taiwan for specific applications, related to CKD, liver cancer and other major

pathologies with high prevalence in Asia. The perspectives after this PhD work are thus related to new developments, summarized hereafter:

Project of International Associated Laboratory – VascView

3D multimodal imaging of vascular plasticity in human diseases

Starting Date – January 2016 (4 years duration, renewable once)

Project (abstract)

The scientific objective of the IAL VASCVIEW is to use complementary imaging resources (morphological/molecular) to study the role of the microvascular plasticity in the development of human pathologies. The ambition is to realize an analytical continuum covering the molecular - cellular – tissue scales in the characteristic organization of the pathological microvasculature, in particular for incurable cancers (glioblastoma, pancreas carcinoma, and lung cancer), and a degenerative pathology (chronic kidney disease). These pathologies have in common to be evolutionary by developing an abnormal interface between the extracellular matrix, the microvasculature and the cellular metabolism. Because of their unpredictable tissue distribution, these parameters can be analyzed only by combining 3D imaging techniques, in particular for the morphological and molecular analysis of the pathological organ. For each pathology, the analysis in native form of the growth factor - receptor interactions by coupling AFM / infrared microscopy at 10 nm of resolution will allow to study the importance of key growth factors on vascular plasticity at the single molecule level in native form. Infrared imaging coupled with X-Ray tomography will allow to estimate the impact of these growth factors on the construction of healthy and pathological capillaries. The same imaging approaches will finally allow to realize a volumetric histology at the scale of the whole organ to study the vascular network formed at different stages of the pathology progression.

Our technological objective is thus to develop new multimodal imaging (MI) solutions for 3D histology, with the aim of realizing a functional volumetric histology, in particular on biopsies, for diagnostic purposes in anatomo-pathology. The developed methodologies will also allow studying the efficiency of pro- or anti-angiogenic drugs on the vascular plasticity for the treatment of these pathologies.

The main advantage of this IAL is the use of state-of-the-art imaging techniques, in particular for X-Ray tomography (bringing unique analytical performances for *in vivo* and high-resolution imaging on single cells and small animals) and for infrared imaging (with specific and unique setups allowing the analysis of a single protein in native form or for 3D histology), taking advantage of conventional sources (Bordeaux / Taipei) and synchrotron radiation (Taiwan) for complementary studies. This situation, unique worldwide, is strengthened by the common development of microscopes, biological models, methods of image acquisitions, and solutions of data processing for the characterization of the biological samples by multimodal imaging. We thus expect from this strong collaboration that it opens new perspectives for the bioimaging and that it helps us to understand the key stages of human pathologies. Another objective

of the project is to use the scientific knowledge acquired to propose new R&D strategies, notably for the industrialization of infrared and X-Ray Benchtop instrumentations and their applications in biology.

Project accepted by Academia Sinica (TWN) on March 2015, and Inserm (FRA) and Univesity of Bordeaux (FRA) on July 2015.

ITEA3.1 European Project – 3Dpathology

Developing 3D Digital Pathology with Spectroscopy

Accepted - starting date January 2016 (for Taiwan) – Oct. 2015 (for France).

Project (abstract)

According to Frost & Sullivan[1,2], the digital pathology market is forecast to grow from $546 million in 2014 to $3.1 billion in 2020. This is based on an estimated of CAGR of 23.1%. This growth, combined with a decreasing number of qualified pathologists will lead to a tremendous increase in workload in pathology departments of clinical and pharmaceutical organizations. On top of this quantitative expansion there is urgent need for higher quality diagnostic information, which enables more effective and efficient treatments.

Clinical opinion leaders have indicated that these needs can best be answered by:

1) The digitalization of pathology labs to increase the diagnostic **capacity** of pathology departments, and
2) Improving the **quality** of diagnosis by the visualization of multi-modal pathology in 3D.

The 3D Pathology project will **address these needs by creating a** - **fast, digital, quantitative, spectroscopic, and multimodal - 3D pathology analysis system.**

We foresee that this 3D quantitative digital pathology solution, based on a combination of multiple existing pathology modalities (a multitude of molecular information is incorporated in the clinical workflow), will lead to a far more personalized treatment of cancer and cardiovascular diseases. The project will also address clinical workflow integration aspects and standardization of data storage and exchange.

The envisioned digital pathology imaging system will address the analysis and interpretation of the **inherently complex pathological images** with a size of 100+GB per sample (mono-modal). Combined with the high throughput rate and huge sample- and system data volume (data sets in the range of Terabytes to Petabytes), technological innovations are required of a completely different level of complexity compared to other state-of-the-art medical imaging solutions (e.g. spectral CT scanners).

Five major software intensive technological challenges are identified and will be cleared in this project:

---

[1] "US and European Digital Pathology Systems Market", Frost & Sullivan, June 2013

[2] "Analysis of the Digital Pathology Market in China", Frost & Sullivan, April 2014

1- Fast and automated 3D acquisition of tissue information using multiple imaging modalities;
2- Fusion of the data acquired by different modalities (different size, different resolution in all directions, different storage format, different spectral bandwidth), which includes techniques like co-registration, alignment, reconstruction.
3- Efficient analysis of the aligned 3D data from different imaging modalities. To enable a high quality diagnosis, the entire tissue sample needs to be analyzed in detail, complemented with patient data. Fast big data analysis algorithms (machine learning and data mining) will be developed to extract and combine the relevant data.
4- Design of new 3D visualization and interaction technologies (equipment and algorithms), optimized for multi-modal 3D pathology.
5- Provide an IT backbone to handle the data of tremendous size produced by the individual imaging modalities (data sets in the range of Terabytes to Petabytes).

The consortium is headed by three major European equipment suppliers (Barco, Bull and Philips), who, together with other equipment, software and service suppliers in this consortium bring complementary solutions and services to the market required to establish the complete multi-model 3D pathology pipeline envisioned (e.g. microscopes, scanners, IT infrastructures, datacenters, 3D image manipulations, research tools, diagnostics algorithms, medical training).
In addition, the three major users (dominating the market in the histology domain) are also represented in the consortium (hospitals and pathological laboratories).

ITEA3.2 European Project – DrugsInOrgans

3D Digital Imaging for Systematic Drug Testing

Submitted Oct.2015 – starting date July 2016.

Project (abstract)

The R&D costs for new therapeutic drugs have raised dramatically over the past two decades, making that major pharmaceutical and biotechnology companies now spend €10.5 billion or 22% of total annual R&D costs on preclinical research, i.e., more than the total spent on Phase I and II activity combined. The preclinical phase includes more and more analyses to check the adverse effects of drugs, and histology is required for safety, pharmacology, pharmacokinetics, and general toxicology, studies. Histological studies represent a major weakness in preclinical studies as they remain limited to the 2D visualization of a limited number of parameters. **Accessing to the 3D organization of organs in small animal models would change drastically this situation, with chemical, morphological, and functional parameters of interest.** Only chemical microscopy techniques can achieve this analytical performance, but they also generate massive datasets that are not currently managed by 3D image software products.

The aim of DrugsInOrgans is to propose an innovative ecosystem for the preclinical validation of pharmaceutical products, with the double advantage of a reduction of R&D costs for companies developing therapeutic molecules as well as an enhancement of the drug candidates' selectivity before starting clinical trials. In the first case, it is due to the systematic screening of effects of drugs on vital organs in small animal models. In the second case, the aim is to provide a new analytical standard, 3D chemical microscopy, currently unemployed in pharmacology. The main technical challenge is not analytical (3D microscopy by spectroscopy), but rather mathematical (HPC on massive image data) and related to the management and safety issues of big data.

The innovation lies in the implementation of a technological platform able to handle the acquisition, the processing and the interpretation of 3D chemical images, i.e., fresh ideas at present unavailable in pharmacology. **The major contribution will be to introduce a systematic analysis of the effects of therapeutic molecules, both on the chemical composition of tissues as on their morphology and functions (metabolic, biochemical ...).** The techniques of 3D microscopy will be complementary (mass, IR/Raman, X-ray fluorescence) and will cover the whole parameters of interest to characterize the possible toxicity of tested molecules. The platform will include a set - HPC, datacenter, software suite - that will allow to compare 3D chemical images (references vs. tests) and to reach routines for data treatments and their 3D visualization, the whole in an open source fashion to facilitate collaborations between companies, where relevant.

The envisioned digital imaging platform will address the analysis and interpretation of the inherently complex pharmaceutical= images with a size of 100+GB per sample (mono-modal). Combined with the HT rate and huge sample and system data volume (data sets in the range of Terabytes to Petabytes), technological innovations are required of a completely different level of complexity compared to other state-of-the-art bioimaging solutions (e.g. spectral and CT scanners).

Five major software intensive technological challenges are considered in this project: 1- Fast and automated 3D acquisition of small animal organs' information using chemical imaging modalities; 2- Efficient analysis of the aligned 3D data from different imaging modalities. To enable a high quality drug testing, the entire organs will be analyzed in detail, complemented with reference analyses (histology…); 3- Fast bigdata analysis algorithms (machine learning and data mining) will be developed to perform mathematical treatments and extract the relevant data; 4- Design of new 3D visualization and interaction technologies (equipment and algorithms), optimized for drug testing and validation; 5- Providing an IT backbone to handle the data of tremendous size produced by chemical imaging modalities (data sets in the range of Terabytes to Petabytes).

The consortium is headed by major **European companies** (Bull, Servier, Sanofi, Siveco, PS-Tech… and from associated countries – CAN, USA, TWN), which, together with other equipment, software and service suppliers in this consortium bring complementary solutions and services to the market required to establish the complete technology pipeline envisioned for the pharmaceutical industry (e.g. microscopes, datacenters, 3D image manipulations, IT infrastructure safety, research tools). The **securing of experimental data** will be specifically handled to ensure a complete preservation of I.P. for pharmaceutical companies. In addition, the **major end-users** (dominating the pharmaceutical market) are also represented in the consortium (biotech and big-pharma companies) and **cover the major pharmaceutical regulations found in Europe, North America and Asia**.

Reference

1. Levey, A.S. and J. Coresh, *Chronic kidney disease.* Lancet, 2012. **379**(9811): p. 165-80.
2. Zhang, Q.L. and D. Rothenbacher, *Prevalence of chronic kidney disease in population-based studies: systematic review.* BMC Public Health, 2008. **8**: p. 117.
3. Coresh, J., et al., *Prevalence of chronic kidney disease in the United States.* JAMA, 2007. **298**(17): p. 2038-47.
4. Iseki, K., *Renal outcomes in chronic kidney disease.* Nephrology (Carlton), 2010. **15 Suppl 2**: p. 27-30.
5. Hsu, C.C., et al., *High prevalence and low awareness of CKD in Taiwan: a study on the relationship between serum creatinine and awareness from a nationally representative survey.* Am J Kidney Dis, 2006. **48**(5): p. 727-38.
6. Wen, C.P., et al., *All-cause mortality attributable to chronic kidney disease: a prospective cohort study based on 462 293 adults in Taiwan.* Lancet, 2008. **371**(9631): p. 2173-82.
7. Kuo, H.W., et al., *Epidemiological features of CKD in Taiwan.* Am J Kidney Dis, 2007. **49**(1): p. 46-55.
8. Su, S.L., et al., *Risk factors and their interaction on chronic kidney disease: A multi-centre case control study in Taiwan.* BMC Nephrol, 2015. **16**: p. 83.
9. Zhang, J.L., et al., *Functional MRI of the kidneys.* J Magn Reson Imaging, 2013. **37**(2): p. 282-93.
10. Thomas, S.R., *Kidney modeling and systems physiology.* Wiley Interdiscip Rev Syst Biol Med, 2009. **1**(2): p. 172-90.
11. Eckardt, K.U., et al., *Evolving importance of kidney disease: from subspecialty to global health burden.* Lancet, 2013. **382**(9887): p. 158-69.
12. Tonelli, M., et al., *Chronic kidney disease and mortality risk: a systematic review.* J Am Soc Nephrol, 2006. **17**(7): p. 2034-47.
13. Go, A.S., et al., *Chronic kidney disease and the risks of death, cardiovascular events, and hospitalization.* N Engl J Med, 2004. **351**(13): p. 1296-305.
14. Levey, A.S., et al., *The definition, classification, and prognosis of chronic kidney disease: a KDIGO Controversies Conference report.* Kidney Int, 2011. **80**(1): p. 17-28.
15. Wouters, O.J., et al., *Early chronic kidney disease: diagnosis, management and models of care.* Nat Rev Nephrol, 2015. **11**(8): p. 491-502.
16. Vassalotti, J.A., L.A. Stevens, and A.S. Levey, *Testing for chronic kidney disease: a position statement from the National Kidney Foundation.* Am J Kidney Dis, 2007. **50**(2): p. 169-80.
17. Levey, A.S., et al., *National Kidney Foundation practice guidelines for chronic kidney disease: evaluation, classification, and stratification.* Ann Intern Med, 2003. **139**(2): p.

137-47.
18. National Kidney, F., *K/DOQI clinical practice guidelines for chronic kidney disease: evaluation, classification, and stratification.* Am J Kidney Dis, 2002. **39**(2 Suppl 1): p. S1-266.
19. Bauer, C., M.L. Melamed, and T.H. Hostetter, *Staging of chronic kidney disease: time for a course correction.* J Am Soc Nephrol, 2008. **19**(5): p. 844-6.
20. Boubred, F., et al., *Developmental origins of chronic renal disease: an integrative hypothesis.* Int J Nephrol, 2013. **2013**: p. 346067.
21. Yang, H.C., Y. Zuo, and A.B. Fogo, *Models of chronic kidney disease.* Drug Discov Today Dis Models, 2010. **7**(1-2): p. 13-19.
22. Hodgkins, K.S. and H.W. Schnaper, *Tubulointerstitial injury and the progression of chronic kidney disease.* Pediatr Nephrol, 2012. **27**(6): p. 901-9.
23. Tucker, P.S., A.T. Scanlan, and V.J. Dalbo, *Chronic kidney disease influences multiple systems: describing the relationship between oxidative stress, inflammation, kidney damage, and concomitant disease.* Oxid Med Cell Longev, 2015. **2015**: p. 806358.
24. Kaissling, B., M. Lehir, and W. Kriz, *Renal epithelial injury and fibrosis.* Biochim Biophys Acta, 2013. **1832**(7): p. 931-9.
25. Lin, S.L., et al., *Pericytes and perivascular fibroblasts are the primary source of collagen-producing cells in obstructive fibrosis of the kidney.* Am J Pathol, 2008. **173**(6): p. 1617-27.
26. Kato, N., et al., *Mapping quantitative trait loci for proteinuria-induced renal collagen deposition.* Kidney Int, 2008. **73**(9): p. 1017-23.
27. Eddy, A.A., *Overview of the cellular and molecular basis of kidney fibrosis.* Kidney Int Suppl (2011), 2014. **4**(1): p. 2-8.
28. Oberg, B.P., et al., *Increased prevalence of oxidant stress and inflammation in patients with moderate to severe chronic kidney disease.* Kidney Int, 2004. **65**(3): p. 1009-16.
29. McCullough, P.A., A.T. Whaley-Connell, and J.A. Vassalotti, *The future of CKD detection: the role for the Kidney Early Evaluation Program.* Nephrol News Issues, 2014. **28**(4): p. 41-2.
30. Kriz, W. and M. LeHir, *Pathways to nephron loss starting from glomerular diseases-insights from animal models.* Kidney Int, 2005. **67**(2): p. 404-19.
31. Carlstrom, M., C.S. Wilcox, and W.J. Arendshorst, *Renal autoregulation in health and disease.* Physiol Rev, 2015. **95**(2): p. 405-511.
32. Hoy, W.E., et al., *A stereological study of glomerular number and volume: preliminary findings in a multiracial study of kidneys at autopsy.* Kidney Int Suppl, 2003(83): p. S31-7.
33. Hughson, M., et al., *Glomerular number and size in autopsy kidneys: the relationship to birth weight.* Kidney Int, 2003. **63**(6): p. 2113-22.

34. Johnson, R.J., *The glomerular response to injury: progression or resolution?* Kidney Int, 1994. **45**(6): p. 1769-82.
35. Hallan, S.I., et al., *Combining GFR and albuminuria to classify CKD improves prediction of ESRD.* J Am Soc Nephrol, 2009. **20**(5): p. 1069-77.
36. Hemmelgarn, B.R., et al., *Relation between kidney function, proteinuria, and adverse outcomes.* JAMA, 2010. **303**(5): p. 423-9.
37. Woods, L.L., *Intrarenal mechanisms of renal reserve.* Semin Nephrol, 1995. **15**(5): p. 386-95.
38. Chaudhary, K., et al., *The emerging role of biomarkers in diabetic and hypertensive chronic kidney disease.* Curr Diab Rep, 2010. **10**(1): p. 37-42.
39. Devarajan, P., *The use of targeted biomarkers for chronic kidney disease.* Adv Chronic Kidney Dis, 2010. **17**(6): p. 469-79.
40. Fassett, R.G., et al., *Biomarkers in chronic kidney disease: a review.* Kidney Int, 2011. **80**(8): p. 806-21.
41. Weissleder, R. and M.J. Pittet, *Imaging in the era of molecular oncology.* Nature, 2008. **452**(7187): p. 580-9.
42. Wang, Y., et al., *Label-free Au cluster used for in vivo 2D and 3D computed tomography of murine kidneys.* Anal Chem, 2015. **87**(1): p. 343-5.
43. Beeman, S.C., et al., *MRI-based glomerular morphology and pathology in whole human kidneys.* Am J Physiol Renal Physiol, 2014. **306**(11): p. F1381-90.
44. Hofman, M., et al., *68Ga-EDTA PET/CT imaging and plasma clearance for glomerular filtration rate quantification: comparison to conventional 51Cr-EDTA.* J Nucl Med, 2015. **56**(3): p. 405-9.
45. Peti-Peterdi, J., et al., *Multiphoton imaging of renal regulatory mechanisms.* Physiology (Bethesda), 2009. **24**: p. 88-96.
46. Andrews, P.M., et al., *High-resolution optical coherence tomography imaging of the living kidney.* Lab Invest, 2008. **88**(4): p. 441-9.
47. Kalantarinia, K., *Novel imaging techniques in acute kidney injury.* Curr Drug Targets, 2009. **10**(12): p. 1184-9.
48. Mileto, A., et al., *Iodine quantification to distinguish clear cell from papillary renal cell carcinoma at dual-energy multidetector CT: a multireader diagnostic performance study.* Radiology, 2014. **273**(3): p. 813-20.
49. Nilsson, A., *Contrast-enhanced ultrasound of the kidneys.* Eur Radiol, 2004. **14 Suppl 8**: p. P104-9.
50. Dunn, K.W., T.A. Sutton, and R.M. Sandoval, *Live-animal imaging of renal function by multiphoton microscopy.* Curr Protoc Cytom, 2012. **Chapter 14**: p. Unit12 9.
51. Willekens, I., et al., *High-resolution 3D micro-CT imaging of breast microcalcifications: a preliminary analysis.* BMC Cancer, 2014. **14**: p. 9.

52. Ehling, J., et al., *Micro-CT imaging of tumor angiogenesis: quantitative measures describing micromorphology and vascularization.* Am J Pathol, 2014. **184**(2): p. 431-41.
53. Ceulemans, A.G., et al., *Serial semiquantitative imaging of brain damage using micro-SPECT and micro-CT after endothelin-1-induced transient focal cerebral ischemia in rats.* J Nucl Med, 2011. **52**(12): p. 1987-92.
54. Kampschulte, M., et al., *Quantitative 3D micro-CT imaging of human lung tissue.* Rofo, 2013. **185**(9): p. 869-76.
55. Tapfer, A., et al., *Three-dimensional imaging of whole mouse models: comparing nondestructive X-ray phase-contrast micro-CT with cryotome-based planar epi-illumination imaging.* J Microsc, 2014. **253**(1): p. 24-30.
56. Easterly, M.E., C.J. Foltz, and M.J. Paulus, *Body condition scoring: comparing newly trained scorers and micro-computed tomography imaging.* Lab Anim (NY), 2001. **30**(3): p. 46-9.
57. Jorgensen, S.M., O. Demirkaya, and E.L. Ritman, *Three-dimensional imaging of vasculature and parenchyma in intact rodent organs with X-ray micro-CT.* Am J Physiol, 1998. **275**(3 Pt 2): p. H1103-14.
58. Lerman, A. and E.L. Ritman, *Evaluation of microvascular anatomy by micro-CT.* Herz, 1999. **24**(7): p. 531-3.
59. Vasquez, S.X., N. Shah, and A.M. Hoberman, *Small animal imaging and examination by micro-CT.* Methods Mol Biol, 2013. **947**: p. 223-31.
60. Bennett, K.M., et al., *The emerging role of MRI in quantitative renal glomerular morphology.* Am J Physiol Renal Physiol, 2013. **304**(10): p. F1252-7.
61. Huang, A.J., V.S. Lee, and H. Rusinek, *Functional renal MR imaging.* Magn Reson Imaging Clin N Am, 2004. **12**(3): p. 469-86, vi.
62. Heilmann, M., et al., *Quantification of glomerular number and size distribution in normal rat kidneys using magnetic resonance imaging.* Nephrol Dial Transplant, 2012. **27**(1): p. 100-7.
63. Beeman, S.C., J.F. Georges, and K.M. Bennett, *Toxicity, biodistribution, and ex vivo MRI detection of intravenously injected cationized ferritin.* Magn Reson Med, 2013. **69**(3): p. 853-61.
64. Knopp, M.V., et al., *Contrast agents for MRA: future directions.* J Magn Reson Imaging, 1999. **10**(3): p. 314-6.
65. Choyke, P.L. and H. Kobayashi, *Functional magnetic resonance imaging of the kidney using macromolecular contrast agents.* Abdom Imaging, 2006. **31**(2): p. 224-31.
66. Xie, L., et al., *Magnetic resonance histology of age-related nephropathy in the Sprague Dawley rat.* Toxicol Pathol, 2012. **40**(5): p. 764-78.
67. Basgen, J.M., et al., *Estimating glomerular number in situ using magnetic resonance*

imaging and biopsy. Kidney Int, 1994. **45**(6): p. 1668-72.
68. Bertram, J.F., *Analyzing renal glomeruli with the new stereology.* Int Rev Cytol, 1995. **161**: p. 111-72.
69. Bertram, J.F., *Estimating glomerular number: why we do it and how.* Clin Exp Pharmacol Physiol, 2013. **40**(11): p. 785-8.
70. Melany, M.L. and E.G. Grant, *Clinical experience with sonographic contrast agents.* Semin Ultrasound CT MR, 1997. **18**(1): p. 3-12.
71. Bertolotto, M., et al., *Renal Masses With Equivocal Enhancement at CT: Characterization With Contrast-Enhanced Ultrasound.* AJR Am J Roentgenol, 2015. **204**(5): p. W557-65.
72. Okur, A., et al., *Relationship between kidney volume and body indexes in the Turkish population determined using ultrasonography.* Int Braz J Urol, 2014. **40**(6): p. 816-22.
73. Dowling, R.J., et al., *Contrast-enhanced Doppler ultrasound for renal artery stenosis.* Australas Radiol, 1999. **43**(2): p. 206-9.
74. Claudon, M., et al., *Renal arteries in patients at risk of renal arterial stenosis: multicenter evaluation of the echo-enhancer SH U 508A at color and spectral Doppler US. Levovist Renal Artery Stenosis Study Group.* Radiology, 2000. **214**(3): p. 739-46.
75. Wei, S., et al., *Two- and three-dimensional contrast-enhanced sonography for assessment of renal tumor vasculature: preliminary observations.* J Ultrasound Med, 2013. **32**(3): p. 429-37.
76. Garra, B.S., et al., *Quantitative ultrasonic detection of parenchymal structural change in diffuse renal disease.* Invest Radiol, 1994. **29**(2): p. 134-40.
77. Prabahar, M.R., et al., *Prediction of tubulo-interstitial injury by Doppler ultrasound in glomerular diseases: value of resistive and atrophic indices.* J Assoc Physicians India, 2008. **56**: p. 21-6.
78. Miller, D.L., C. Dou, and R.C. Wiggins, *Glomerular capillary hemorrhage induced in rats by diagnostic ultrasound with gas-body contrast agent produces intratubular obstruction.* Ultrasound Med Biol, 2009. **35**(5): p. 869-77.
79. Williams, A.R., et al., *Nephron injury induced by diagnostic ultrasound imaging at high mechanical index with gas body contrast agent.* Ultrasound Med Biol, 2007. **33**(8): p. 1336-44.
80. Al-Janabi, S., A. Huisman, and P.J. Van Diest, *Digital pathology: current status and future perspectives.* Histopathology, 2012. **61**(1): p. 1-9.
81. Kayser, G. and K. Kayser, *Quantitative pathology in virtual microscopy: history, applications, perspectives.* Acta Histochem, 2013. **115**(6): p. 527-32.
82. Haleem, N.Y., et al., *Concomitant protective and therapeutic role of verapamil in chronic mercury induced nephrotoxicity in the adult rat: histological, morphometric and ultrastructural study.* Arch Med Sci, 2015. **11**(1): p. 199-209.

83. Advani, A., et al., *Fluorescent microangiography is a novel and widely applicable technique for delineating the renal microvasculature.* PLoS One, 2011. **6**(10): p. e24695.
84. Debbaut, C., et al., *From vascular corrosion cast to electrical analog model for the study of human liver hemodynamics and perfusion.* IEEE Trans Biomed Eng, 2011. **58**(1): p. 25-35.
85. Wei, W., et al., *Evidence of angiogenesis and microvascular regression in autosomal-dominant polycystic kidney disease kidneys: a corrosion cast study.* Kidney Int, 2006. **70**(7): p. 1261-8.
86. Yu, X.J., et al., *[The SEM observation of brain tissues and vascular corrosion cast of closed diffuse brain injuries].* Fa Yi Xue Za Zhi, 1999. **15**(1): p. 3-4, 62.
87. Rummelt, V., et al., *Three-dimensional relationships between tumor cells and microcirculation with double cyanine immunolabeling, laser scanning confocal microscopy, and computer-assisted reconstruction: an alternative to cast corrosion preparations.* J Histochem Cytochem, 1994. **42**(5): p. 681-6.
88. Giacomini, A., et al., *Brain angioarchitecture and intussusceptive microvascular growth in a murine model of Krabbe disease.* Angiogenesis, 2015. **18**(4): p. 499-510.
89. Vandeghinste, B., et al., *Replacing vascular corrosion casting by in vivo micro-CT imaging for building 3D cardiovascular models in mice.* Mol Imaging Biol, 2011. **13**(1): p. 78-86.
90. Wagner, R., et al., *High-resolution imaging of kidney vascular corrosion casts with Nano-CT.* Microsc Microanal, 2011. **17**(2): p. 215-9.
91. Snyder, S. and B. Pendergraph, *Detection and evaluation of chronic kidney disease.* Am Fam Physician, 2005. **72**(9): p. 1723-32.
92. Grenier, N., M. Pedersen, and O. Hauger, *Contrast agents for functional and cellular MRI of the kidney.* Eur J Radiol, 2006. **60**(3): p. 341-52.
93. Grenier, N., et al., *Functional MRI of the kidney.* Abdom Imaging, 2003. **28**(2): p. 164-75.
94. Hynes, A., et al., *Molecular mapping of periodontal tissues using infrared microspectroscopy.* BMC Med Imaging, 2005. **5**(1): p. 2.
95. Baker, M.J., et al., *Using Fourier transform IR spectroscopy to analyze biological materials.* Nat Protoc, 2014. **9**(8): p. 1771-91.
96. Petibois, C. and G. Deleris, *Chemical mapping of tumor progression by FT-IR imaging: towards molecular histopathology.* Trends Biotechnol, 2006. **24**(10): p. 455-62.
97. Mantsch, H.H. and D. Chapman, *Infrared spectroscopy of biomolecules*. 1996, New York: Wiley-Liss. xi, 359 p.
98. Haris, P.I. and D. Chapman, *The conformational analysis of peptides using Fourier transform IR spectroscopy.* Biopolymers, 1995. **37**(4): p. 251-63.

99. Mordechai, S., et al., *Possible common biomarkers from FTIR microspectroscopy of cervical cancer and melanoma.* J Microsc, 2004. **215**(Pt 1): p. 86-91.
100. Kole, M.R., et al., *Discrete frequency infrared microspectroscopy and imaging with a tunable quantum cascade laser.* Anal Chem, 2012. **84**(23): p. 10366-72.
101. Kroger-Lui, N., et al., *Rapid identification of goblet cells in unstained colon thin sections by means of quantum cascade laser-based infrared microspectroscopy.* Analyst, 2015. **140**(7): p. 2086-92.
102. Tobin, M.J., et al., *Infrared microscopy of epithelial cancer cells in whole tissues and in tissue culture, using synchrotron radiation.* Faraday Discuss, 2004. **126**: p. 27-39; discussion 77-92.
103. Martin, M.C., et al., *3D spectral imaging with synchrotron Fourier transform infrared spectro-microtomography.* Nat Methods, 2013. **10**(9): p. 861-4.
104. Nasse, M.J., et al., *High-resolution Fourier-transform infrared chemical imaging with multiple synchrotron beams.* Nat Methods, 2011. **8**(5): p. 413-6.
105. Dorling, K.M. and M.J. Baker, *Rapid FTIR chemical imaging: highlighting FPA detectors.* Trends Biotechnol, 2013. **31**(8): p. 437-8.
106. Bhargava, R., *Infrared spectroscopic imaging: the next generation.* Appl Spectrosc, 2012. **66**(10): p. 1091-120.
107. Bellisola, G. and C. Sorio, *Infrared spectroscopy and microscopy in cancer research and diagnosis.* Am J Cancer Res, 2012. **2**(1): p. 1-21.
108. Matthaus, C., et al., *Chapter 10: Infrared and Raman microscopy in cell biology.* Methods Cell Biol, 2008. **89**: p. 275-308.
109. Petter, C.H., et al., *Development and application of Fourier-transform infrared chemical imaging of tumour in human tissue.* Curr Med Chem, 2009. **16**(3): p. 318-26.
110. Malins, D.C., et al., *The etiology and prediction of breast cancer. Fourier transform-infrared spectroscopy reveals progressive alterations in breast DNA leading to a cancer-like phenotype in a high proportion of normal women.* Cancer, 1995. **75**(2): p. 503-17.
111. Malins, D.C., N.L. Polissar, and S.J. Gunselman, *Tumor progression to the metastatic state involves structural modifications in DNA markedly different from those associated with primary tumor formation.* Proc Natl Acad Sci U S A, 1996. **93**(24): p. 14047-52.
112. Petibois, C. and B. Desbat, *Clinical application of FTIR imaging: new reasons for hope.* Trends Biotechnol, 2010. **28**(10): p. 495-500.
113. Tiwari, S. and R. Bhargava, *Extracting knowledge from chemical imaging data using computational algorithms for digital cancer diagnosis.* Yale J Biol Med, 2015. **88**(2): p. 131-43.
114. Fernandez, D.C., et al., *Infrared spectroscopic imaging for histopathologic recognition.*

Nat Biotechnol, 2005. **23**(4): p. 469-74.
115. Mitchell, A.L., et al., *Vibrational spectroscopy of biofluids for disease screening or diagnosis: translation from the laboratory to a clinical setting.* J Biophotonics, 2014. **7**(3-4): p. 153-65.
116. Gajjar, K., et al., *Fourier-transform infrared spectroscopy coupled with a classification machine for the analysis of blood plasma or serum: a novel diagnostic approach for ovarian cancer.* Analyst, 2013. **138**(14): p. 3917-26.
117. Ollesch, J., et al., *FTIR spectroscopy of biofluids revisited: an automated approach to spectral biomarker identification.* Analyst, 2013. **138**(14): p. 4092-102.
118. Bhargava, R., et al., *High throughput assessment of cells and tissues: Bayesian classification of spectral metrics from infrared vibrational spectroscopic imaging data.* Biochim Biophys Acta, 2006. **1758**(7): p. 830-45.
119. Reddy, R.K. and R. Bhargava, *Accurate histopathology from low signal-to-noise ratio spectroscopic imaging data.* Analyst, 2010. **135**(11): p. 2818-25.
120. Noreen, R., et al., *Functional histology of glioma vasculature by FTIR imaging.* Anal Bioanal Chem, 2011. **401**(3): p. 795-801.
121. Bobroff, V., et al., *FTIR spectroscopy characterization of fatty-acyl-chain conjugates.* Anal Bioanal Chem, 2015.
122. Nichols, E.F., *A study of the transmission spectra of certain substances in the infrared.* Physical Rev, 1893. **1**(1): p. 1-18.
123. Coblentz, W.W., *Investigations of Infrared Spectra*, in *Carnegie Institute of Washington*, T.P.P.N.M. USA, Editor. 1905: Washington D.C. p. 1-190.
124. Ambrose, E.J. and A. Elliott, *Infra-red spectra and structure of fibrous proteins.* Proceedings of the Royal Society of London, 1951. **260**: p. 206-219.
125. Naumann, D., D. Helm, and H. Labischinski, *Microbiological characterizations by FT-IR spectroscopy.* Nature, 1991. **351**(6321): p. 81-2.
126. Petibois, C., et al., *Determination of glucose in dried serum samples by Fourier-transform infrared spectroscopy.* Clin Chem, 1999. **45**(9): p. 1530-5.
127. Budinova, G., J. Salva, and K. Volka, *Application of molecular spectroscopy in the mid-infrared region to the determination of glucose and cholesterol in whole blood and in blood serum.* Appl Spectrosc, 1997. **51**(5): p. 631-5.
128. Ward, K.J., et al., *Quantitative infrared spectroscopy of glucose in blood using partial least-squares analyses.* SPIE: Fourier Transform Spectroscopy, 1989. **1145**: p. 607-8.
129. Petibois, C., et al., *Plasma protein contents determined by Fourier-transform infrared spectrometry.* Clin Chem, 2001. **47**(4): p. 730-8.
130. Petibois, C., et al., *Differentiation of populations with different physiologic profiles by plasma Fourier-transform infrared spectra classification.* J Lab Clin Med, 2001. **137**(3): p. 184-90.

131. Barer, R., A.R.H. Cole, and H.W. Thompson, *Infra-Red Spectroscopy with the Reflecting Microscope in Physics, Chemistry and Biology.* Nature, 1949. **163**: p. 198-201.
132. Innocenzi, P., et al., *Time-resolved infrared spectroscopy as an in situ tool to study the kinetics during self-assembly of mesostructured films.* J Phys Chem B Condens Matter Mater Surf Interfaces Biophys, 2006. **110**(22): p. 10837-41.
133. Petibois, C. and M. Cestelli Guidi, *Bioimaging of cells and tissues using accelerator-based sources.* Anal Bioanal Chem, 2008. **391**(5): p. 1599-608.
134. Petibois, C., et al., *A bright future for synchrotron imaging.* Nat Photonics, 2009. **3**(4): p. 179.
135. Petibois, C., et al., *Synchrotron radiation FTIR imaging in minutes: a first step towards real-time cell imaging.* Anal Bioanal Chem, 2010. **397**(6): p. 2123-9.
136. Petibois, C., et al., *Facing the challenge of biosamples FTIR imaging using the synchrotron radiation source.* J Synhrotron Rad, 2010. **17**(1): p. 1-11.
137. Drogat, B., et al., *Acute L-Glutamine Deprivation Compromises VEGF-A Up-regulation in A549/8 Human Carcinoma Cells.* J Cell Physiol, 2007. **212**(8): p. 463-72.
138. Petibois, C., *Imaging methods for elemental, chemical, molecular, and morphological analyses of single cells.* Anal Bioanal Chem, 2010. **397**(6): p. 2051-2065.
139. Cestelli Guidi, M., et al., *Experimental ATR device for real-time SR-FTIR imaging of living cells.* Biotechnol Adv, 2013. **31**: p. 402-7.
140. Petibois, C., et al., *Analytical performances of FT-IR spectrometry and imaging for concentration measurements within biological fluids, cells, and tissues.* Analyst, 2006. **131**(5): p. 640-7.
141. Levenson, E., P. Lerch, and M.C. Martin, *Spatial resolution limits for synchrotron-based infrared microspectroscopy.* Infrared Phys Technol, 2008. **51**(5): p. 413-16.
142. Fabian, H., P. Lasch, and D. Naumann, *Analysis of biofluids in aqueous environment based on mid-infrared spectroscopy.* J Biomed Opt, 2005. **10**(3): p. 031103.
143. Cestelli-Guidi, M., et al., *Optical performances of SINBAD, the Synchrotron INfrared Beamline At DAPHNE.* J Opt Soc Am A, 2005. **22**(12): p. 2810-7.
144. Petibois, C., et al., *Method for determining absorption bands*, Inserm, Editor. 2014: France.
145. Petibois, C., *Imaging techniques with synchrotron radiation.* Anal Bioanal Chem, 2010. **397**(6): p. 2031-2032.
146. Mayet, C., et al., *Analysis of bacterial polyhydroxybutyrate production by multimodal nanoimaging.* Biotechnol Adv, 2013. **31**(3): p. 369-74.
147. Ghosh, S., et al., *Conducting polymer nanostructures for photocatalysis under visible light.* Nat Mater, 2015. **14**(5): p. 505-11.
148. Houel, J., et al., *Midinfrared absorption measured at a lambda/400 resolution with an atomic force microscope.* Opt Express, 2009. **17**(13): p. 10887-94.

149. Petibois, C., *The emergence of multimodal imaging methods for real-time nanoscopy.* Anal Bioanal Chem, 2011. **399**.
150. Coresh, J., et al., *Prevalence of chronic kidney disease and decreased kidney function in the adult US population: Third National Health and Nutrition Examination Survey.* Am J Kidney Dis, 2003. **41**(1): p. 1-12.
151. Keith, D.S., et al., *Longitudinal follow-up and outcomes among a population with chronic kidney disease in a large managed care organization.* Arch Intern Med, 2004. **164**(6): p. 659-63.
152. Puelles, V.G., et al., *Glomerular hypertrophy in subjects with low nephron number: contributions of sex, body size and race.* Nephrol Dial Transplant, 2014. **29**(9): p. 1686-95.
153. Amharref, N., et al., *Brain tissue characterisation by infrared imaging in a rat glioma model.* Biochim Biophys Acta, 2006. **1758**(7): p. 892-9.
154. Wood, B.R., et al., *Fourier transform infrared (FTIR) spectral mapping of the cervical transformation zone, and dysplastic squamous epithelium.* Gynecol Oncol, 2004. **93**(1): p. 59-68.
155. Lasch, P. and D. Naumann, *FT-IR microspectroscopic imaging of human carcinoma thin sections based on pattern recognition techniques.* Cell Mol Biol (Noisy-le-grand), 1998. **44**(1): p. 189-202.
156. Dreissig, I., et al., *Quantification of brain lipids by FTIR spectroscopy and partial least squares regression.* Spectrochim Acta A Mol Biomol Spectrosc, 2009. **71**(5): p. 2069-75.
157. Paschalis, E.P., et al., *FTIR microspectroscopic analysis of normal human cortical and trabecular bone.* Calcif Tissue Int, 1997. **61**(6): p. 480-6.
158. Noreen, R., et al., *FTIR spectro-imaging of collagen scaffold formation during glioma tumor development.* Anal Bioanal Chem, 2013. **405**(27): p. 8729-36.
159. Spalazzi, J.P., et al., *Quantitative mapping of matrix content and distribution across the ligament-to-bone insertion.* PLoS One, 2013. **8**(9): p. e74349.
160. Noreen, R., et al., *Detection of collagens in brain tumors based on FTIR imaging and chemometrics.* Anal Bioanal Chem, 2011. **401**(3): p. 845-52.
161. Majzner, K., et al., *Secondary structure of proteins analyzed ex vivo in vascular wall in diabetic animals using FT-IR spectroscopy.* Analyst, 2013. **138**(24): p. 7400-10.
162. Saeed, A., et al., *Effects of Very Low Dose Fast Neutrons on Cell Membrane And Secondary Protein Structure in Rat Erythrocytes.* PLoS One, 2015. **10**(10): p. e0139854.
163. Leskovjan, A.C., A. Kretlow, and L.M. Miller, *Fourier transform infrared imaging showing reduced unsaturated lipid content in the hippocampus of a mouse model of Alzheimer's disease.* Anal Chem, 2010. **82**(7): p. 2711-6.

164. Wood, B.R., et al., *A three-dimensional multivariate image processing technique for the analysis of FTIR spectroscopic images of multiple tissue sections.* BMC Med Imaging, 2006. **6**: p. 12.
165. Nagle, R.B., et al., *Unilateral obstructive nephropathy in the rabbit. I. Early morphologic, physiologic, and histochemical changes.* Lab Invest, 1973. **28**(4): p. 456-67.
166. Chevalier, R.L., M.S. Forbes, and B.A. Thornhill, *Ureteral obstruction as a model of renal interstitial fibrosis and obstructive nephropathy.* Kidney Int, 2009. **75**(11): p. 1145-52.
167. Wilson, D.R., *Renal function during and following obstruction.* Annu Rev Med, 1977. **28**: p. 329-39.
168. Kawada, N., et al., *Increased oxidative stress in mouse kidneys with unilateral ureteral obstruction.* Kidney Int, 1999. **56**(3): p. 1004-13.
169. Massy, Z.A. and T. Nguyen-Khoa, *Oxidative stress and chronic renal failure: markers and management.* J Nephrol, 2002. **15**(4): p. 336-41.
170. Cracowski, J.L., T. Durand, and G. Bessard, *Isoprostanes as a biomarker of lipid peroxidation in humans: physiology, pharmacology and clinical implications.* Trends Pharmacol Sci, 2002. **23**(8): p. 360-6.
171. Buhrle, C.P., et al., *The hydronephrotic kidney of the mouse as a tool for intravital microscopy and in vitro electrophysiological studies of renin-containing cells.* Lab Invest, 1986. **54**(4): p. 462-72.
172. Tanner, G.A. and L.C. Knopp, *Glomerular blood flow after single nephron obstruction in the rat kidney.* Am J Physiol, 1986. **250**(1 Pt 2): p. F77-85.